Title
The Physics of Fullerene-related Materials

Author
Benedict, Lorin X.

Publication Date
1996-12-01

LBNL-39885
UC-404

ERNEST ORLANDO LAWRENCE
BERKELEY NATIONAL LABORATORY

The Physics of Fullerene-Related Materials

Lorin X. Benedict

Materials Sciences Division

December 1996
Ph.D. Thesis

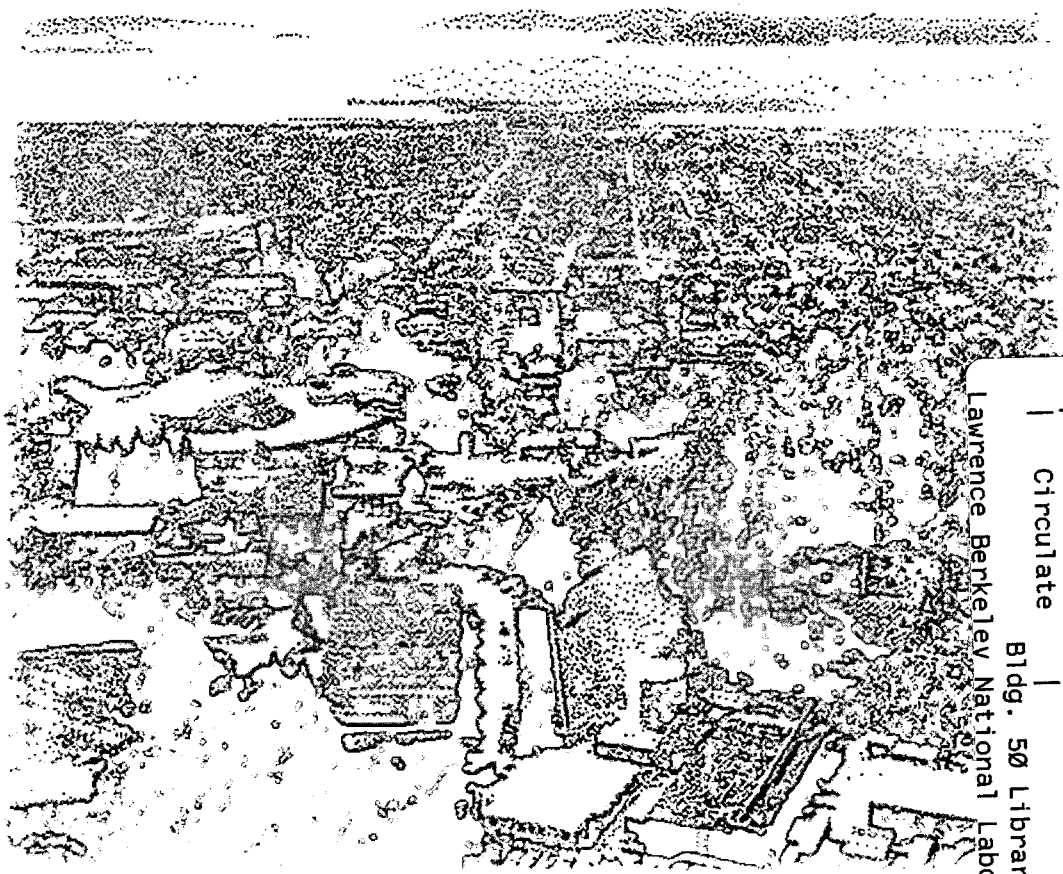

LBNL-39885

DISCLAIMER

LBNL-39885
UC-404

THE PHYSICS OF FULLERENE-RELATED MATERIALS

by

Lorin X. Benedict

B.A. (University of Chicago) 1992

M.A. (University of California at Berkeley) 1995

A dissertation submitted in partial satisfaction of the

requirements for the degree of

Doctor of Philosophy

in

Physics

in the

GRADUATE DIVISION

of the

UNIVERSITY of CALIFORNIA at BERKELEY

Committee in charge:

Professor Steven G. Louie, Chair

Professor Raymond Jeanloz

Professor Alex Zettl

1996

This work was supported in part by the National Science Foundation Grant No. DMR-9520554 and by the Director, Office of Energy Research, Office of Basic Energy Sciences, Materials Sciences Division of the U. S. Department of Energy under Contract No. DE-AC03-76SF00098.

The Physics of Fullerene-Related Materials

by

Lorin X. Benedict

0.1 Acknowledgements

First and foremost I would like to thank my advisor, Steven G. Louie, for providing excellent guidance, and for letting me do pretty much what I wanted. Secondly, I thank my parents (all four of them) for the same reasons.

I have benifited from collaborations with many people over the last four years. In fact, I would say that this thesis is as much theirs as it is mine. I collaborated with Dr. Vincent H. Crespi on the work appearing in chapters 6, 9, 11, and 12, and he gave much-needed advice in many other areas as well. I have been very affected by his approach to scientific problems, and I hope to continue to hone the skills I have learned from him. Chapters 3 and 5 would not have been possible without the efforts of Dr. Eric L. Shirley, and I will continue to work with him in the future. The work of Dr. Leonor Chico was insrumental in bringing about chapters 6 and 10. Her enthusiasm for physics (and music) was a joy to me.

Others who I have collaborated with are: Dr. Xavier Blase, the group of Prof. Gerard Martinez, Nasreen G. Chopra, Prof. Alex Zettl, and Mimo. Most notably, I thank my most frequent collaborator, Prof. Marvin L. Cohen, whose piercing insight and intellectual inventiveness provided a beacon in a sometimes foggy morass of findings and interpretations.

In addition, I have benifitted from fruitful disscussions with: A. Rappe, Y. Miyamoto, A. Rubio, F. Mauri, S. Saito, J. Cerda, K. Shirai, W. Beyermann, M. Côté, A. Mizel, R. Luyken, K. Erikson, J. Hone, M. Fuhrer, L. Bernardo, and C. Regan. Thanks also to O. Zakharov, B. Kralik, and B. Pfrommer for helping so much on computer matters.

There are four non-academic areas which have greatly enhanced my life and have served to define it over the last four years: music, film, table tennis, and food. In the food department, I thank the Mandarin Garden Restauraunt, 2025 Shattuck Ave. Without their almond chicken and hunan prawns, this work would definately not have been pos-

sible. Along these lines, I thank my long-time friend Everett Lipman for accompanying me there on many occasions.

In film, I have recently been inspired by the works of Andrzej Wajda, Roman Polanski, Andrei Tarkovsky, Ang Lee, Wayne Wang, Henri-Georges Clouzot, Derek Jarman, Satyajit Ray, Todd Haynes and the incomparable John Cassavetes. I have continued to enjoy my old favorites: Alfred Hitchcock, Orson Welles, Preston Sturges, Billy Wilder, Leni Riefenstahl, Luis Bunuel, Stanley Kubrick, Robert Siodmak, Pedro Almodovar, William Dieterle, Ken Russell, David Lean, Martin Scorsese, Werner Hertzog, Spike Lee, Akira Kurosawa, Elia Kazan, Robert Altman, Wim Wenders, Carol Reed, Yasujiro Ozu, and Jacky Chan. Much thanks to Jennifer Huang and Karen Kwong for accompanying me on many cinematic adventures. I also thank UC Theater and Movie Image for fighting the good fight of serious cinefiles.

I have been deeply moved by musicians too numerous to mention. A few notables are: Sergei Prokofiev, Igor Stravinski, Mozart, Beethoven, Tchaikovsky, Wagner, Richard Strauss, Claude Debussy, Maurice Ravel, Gabriel Faure, Sergei Rachmaninoff, Samuel Barber, Carl Neilsen, Brahms, Bela Bartok, Dimitri Shostokovich, Witold Lutoslawski, Jacob Druckman, Camille Saint-Sains, Bach, John Mack, Richard Woodams, Richard Solis, Frank Cohen, Jimmy Hamilton, Larry Combs, Bernie Adlestein, Freddy Hubbard, Clifford Brown, David McGill, Ron Phillips, Murray Panitz, Cho-Lian Lin, Pinky Zucherman, the great Mistislav Rostoprovich, Glenn Gould, Horowitz, Art Tatum, Oscar Peterson, Hank Jones, the Cleveland Quartet, the Cleveland Orchestra, the Philidelphia Orchestra, Duke Ellington, Herbie Hancock, Charles Mingus, Sun Ra, John Gilmore, Yusef Lateef, Stan Getz, Sam Rivers, Joe Henderson, Billy Harper, Lew Tebackin, Gene Ammonds, Jimmy Smith, Richard "Groove" Holmes, Wes and Buddy Montgomery, Julian Adderly, Bunky Green, Eric Dolphy, Sonny Fortune, Sonny Stitt, Jacky MaClean, Rasaan Roland Kirk, Steve Coleman and 5 Elements, Steve Coleman and Metrics, Steve Coleman period, Vijay Iyer, Walter Savage, Eliot Kavee, Zakhir Husain, Vicu, Gene

Lake, the young Tony Williams, Art Blakey, Ralph Peterson, Al Foster, Harvey Mason, Anthony Braxton, Roscoe Mitchell, the Mills Brothers, Rosemary Clooney, Carol Sloan, Shirley Horn, Johnny Hartmann, Austin Cromer, Mel Torme, and Nat Cole. I am indebted to Vijay Iyer and χ Epps for sharing many musical insights and experiences with me.

In the table tennis arena, I thank my many practice partners, teachers, and fellow enthusiasts: Hugh Fountain, Mark Ritter, Wang Shanxing, Phillip and Lum Ding Lim, Shashin Shodhan, the myriad Lees and Dos, Freddy Gabriel, Jiyoung Choi, Chen Ling, Sam Roberson, all the players at Chinese Playground–SF (but most particularly the Bus Driver!), Masaaki Tajima, the fantastic James Therriault, Dennis Davis, and most of all the great Shonie Aki, whose backhand stance and side-spin pushes will mystify me to my dying day. Among the luminaries that I draw on for inspiration: Cheng Yinghua, J.-O. Waldner (of course), Vladimir Samsonov, Kong Linghui, Wang Tao, Ding Song, Li Gun Sang, Feng Zhe, Liu Guoliang, Jorge Rosskopf, Philipe Saive, Petr Korbel, Johnny Huang, Ni Xia Lian, Qiao Yunping, Chen Zhibin, Oh Sang Eun, Toshio Tasaki, Liu Song, Yoo Nam Kyu, Andrzej Grubba, and the unbelievable Kim Taek Soo, who for me represents the pinnacle of athletic expression.

Finally, I thank my uncle Gershon Berman PhD for his South-Bay wisdom, and my sister Cheryl Benedict for just being herself.

0.2 Dedication

This work is dedicated to my father, Victor Benedict, who instilled in me an appreciation for science, music, and laughter.

Contents

Abstract

THE PHYSICS OF FULLERENE-RELATED MATERIALS

by

Lorin X. Benedict

Doctor of Philosophy in Physics

University of California at Berkeley

Professor Steven G. Louie, Chair

Graphite, or sp^2-bonded carbon, is a semimetallic planar material consisting of sheets of interlinked six-fold carbon rings. Materials exist which are made of graphitic sheets that have been deformed in various ways. One example is the fullerenes, quasispherical cages of carbon made of interlinked five-fold and six-fold rings. Molecular solids of fullerenes have been formed; they are semiconductors with band-gaps of several eV. Another example is carbon nanotubes. These are cylinders of rolled-up sheets that are many microns long, but only nanometers wide. They can be semiconductors or metals depending on how the sheet is rolled into a cylinder. We study many physical properties of fullerene-related materials in this work. Throughout, the main theme is that interesting phenomena emerge when different electronic structures (metal $\longrightarrow$ semiconductor) couple to reduced dimensionality.

First we examine optical absorption in solid C_{60}, and study the physics of excitons hopping from molecule to molecule. We find that the lowest-lying excitons have predominantly Frenkel character, with the electron and hole located on the same molecule. Next we study carbon nanotubes. The electronic structure of very small-radius tubes is

calculated, and large sheet curvature is shown to give rise to metallic behavior. Junctions of dissimilar nanotubes are described which act as metal/semiconductor and semiconductor/semiconductor heterostructures with potential device applications. The low-temperature heat capacity of nanotubes is shown to differ substantially from that of graphite, owing to the reduced dimensionality. The static polarizability tensor of single-walled tubes is found to be highly anisotropic, and its magnitude is a simple function of both the tube radius and the band-gap. Electron transport through nanotubes and nanotube heterojunctions is investigated, and metal/metal heterojunctions are shown to have a conductance which depends sensitively on the symmetry of the interface. A collapsed, or flattened state of nanotubes is presented, and analysis of TEM images of these structures affords an estimate of the graphite intersheet attractive energy. We close with a study of planar carbon pentaheptite, a possible metallic alternative to graphite consisting of interlinked five-fold and seven-fold carbon rings.

Chapter 1

Introduction

This work is devoted to the study of a class of materials made solely of carbon. It therefore seems appropriate that we begin with a brief discussion of the atom itself. Carbon is one of the more abundant elements in the universe, the fifth most abundant in the solar system [1]. All life on Earth is carbon-based, a fact which illustrates its versatility in forming different kinds of chemical bonds. Carbon has six protons in its nucleus (as well as 6 neutrons), so the neutral atom has six electrons. Using the hydrogenic, central-field approximation, we can think of the six electrons as being in the configuration $[1s^2]2s^2 2p^2$. The brackets surround what we tend to think of as the core of the atom. These two electrons are spatially located quite close to the nucleus, and the energy to remove one from the atom is very large compared to the energy to remove one of the outer shell electrons[2]. Thus, they can be considered as somewhat inert, even when perturbed by the fields of other nearby atoms. The ground state configuration is one with total orbital angular momentum $L = 1$, total spin $S = 1$, and total angular momentum, $J = L + S = 0$, commonly notated ${}^3P_0$.

When many carbon atoms are brought together to form a liquid or solid, it becomes energetically favorable for one of the $2s$ electrons to be promoted to the $2p$ position, so the configuration becomes more like $[1s^2]2s^1 2p^3$. This is known as hybridization. It will be convenient to represent the three p-states using a cartesian basis, with each p-orbital pointing along a cartesian axis. The valence states are then denoted $|s>, |p_x>, |p_y>, |p_z>$. There are two common kinds of hybridization that condensed forms of carbon naturally favor. The first is sp^3 hybridization, in which each carbon atom has four *identical* bonds eminating from it. We can represent these four bond orbitals as

linear combinations of the valence states: $\frac{1}{2}[|s> +|p_x> +|p_y> +|p_z>]$, $\frac{1}{2}[|s> +|p_x> -|p_y> -|p_z>]$, $\frac{1}{2}[|s> -|p_x> +|p_y> -|p_z>]$, $\frac{1}{2}[|s> -|p_x> -|p_y> +|p_z>]$. The bonds point tetrahedrally outward in space, and each has $\frac{1}{4}s$-character, and $\frac{3}{4}p$-character. The second common kind of hybridization is sp^2, in which each carbon atom shares three identical bonds in a plane, and one inequivalent bond pointing perpendicular to that plane. The three identical bonds each have $\frac{1}{3}s$-character, and $\frac{2}{3}p$-character, while the perpendicular bond has only p-character. The planar bonds are known as σ-bonds. Their cartesian representation is: $\frac{1}{\sqrt{2}}[|s> +|p_x>]$, $\frac{1}{\sqrt{2}}[|s> -\frac{1}{2}|p_x> +\frac{\sqrt{3}}{2}|p_y>]$, $\frac{1}{\sqrt{2}}[|s> -\frac{1}{2}|p_x> -\frac{\sqrt{3}}{2}|p_y>]$. They are unchanged upon reflection about the plane ($z \longrightarrow -z$). The perpendicular bond is called a π-bond, with cartesian representation: $|p_z>$. It acquires a minus sign when reflected about the plane.

It should be noted that carbon is the only element that favors two radically different kinds of covalent bonding (at zero pressure). Even other elements with the same valence electron configuration, like silicon and germainium, participate almost exclusively in sp^3 bonding. This is thought to be due to the lack of a large core in carbon. Smaller bondlengths are needed for sp^2 bonding, and this is not allowed for atoms with large core regions.

From a materials point of view, the two types of bonding give rise to condensed states with very distinct structural signatures. Matter composed chiefly of sp^3-bonded carbon tends to extend isotropically in all directions, while sp^2-bonded carbon tends to be layered, in accordance with the intrinsically planar geometry of sp^2 bonding. For this reason, it is natural to think of the two situations as opposite extremes. Nevertheless, the two forms are *equally stable*. This freak occurance of nature defies any simple explanation, although we will see that it can be *post*dicted by first-principles calculations.

It is instructive to consider carbon solids which consist entirely of one or the other type of bonding, and in fact, both solids are familiar from everyday experience. The perfect sp^3 solid is diamond, in which each carbon atom is surrounded by four carbon

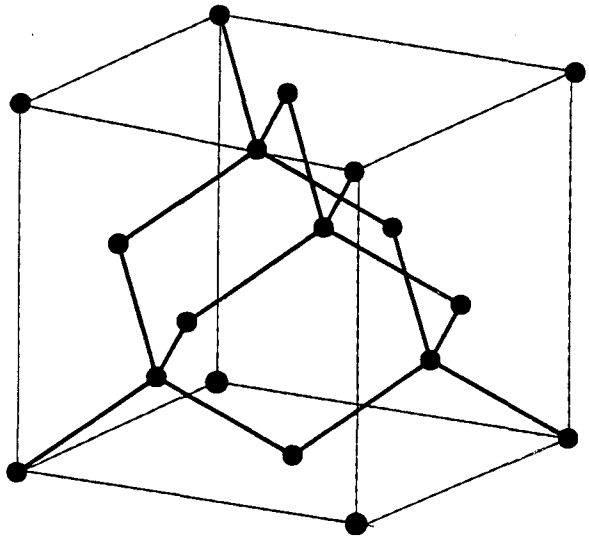

Figure 1.1: Illustration of the atomic structure of cubic diamond. The black circles represent carbon atoms. The carbon-carbon nearest neighbor distance is 1.54 Å.

nearest neighbors 1.54 Å away in a tetrahedral arrangement. There are two forms of diamond, the most common of which is illustrated in Fig. 1.1. All forms are insulators with band-gaps of $\sim$ 5.5 eV. The perfect sp^2 solid is graphite. Again, there are a couple different forms of this, with the most common shown in Fig. 1.2. The geometry is layered, with each atom surrounded by three nearest neighbors in the plane. As per the above discussion, the nearest neighbor distance is 1.42 Å, smaller than the nearest neighbor distance in diamond. Graphite is a semimetal, so it has zero band-gap. We will consider the specifics of its electronic structure below. Other forms of carbon, such as amorphous or liquid carbon, have bonding which is somewhere between these two extremes. It is the pure sp^3 and sp^2 forms which have the lowest energy. State-of-the-art first-principles electronic structure calculations yield a cohesive energy of 7.45 eV/atom for diamond and 7.40 eV/atom for graphite [3]. This suggests the schematic picture of Fig. 1.3, in which perfect sp^3 and sp^2 solids are roughly degenerate, and

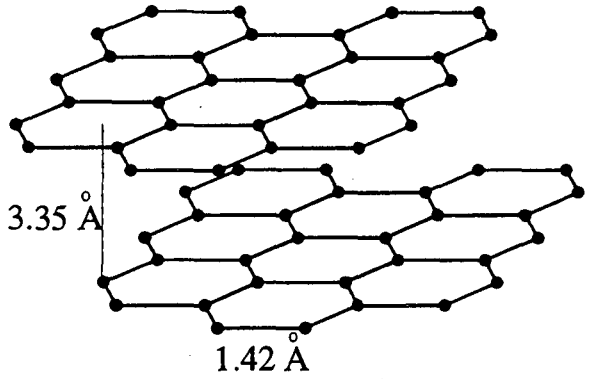

Figure 1.2: Atomic structure of hexagonal graphite. The nearest neighbor distance in the plane is 1.42 Å, while the inter-planar distance is 3.35 Å.

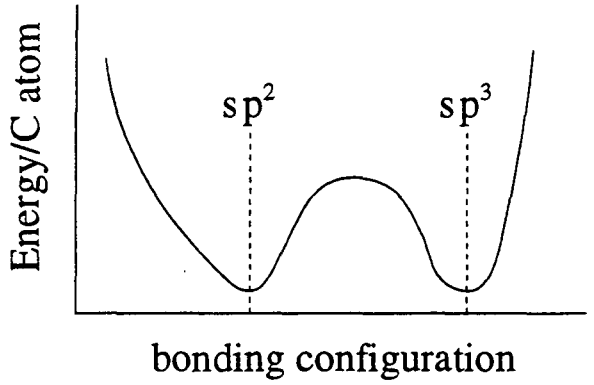

Figure 1.3: Schematic picture of dependence of the cohesive energy of carbon materials on bonding configuration.

everything else is higher in energy.

The focus of this work is on the properties of carbon materials whose bonding configurations are close to sp^2. Since most physical properties are a direct consequence of electronic structure, we now describe the electronic structure of the perfect sp^2 solid, graphite, in some detail. We consider only a single sheet of graphite, for the interaction between layers is relatively weak, as is evidenced by the large inter-layer distance of 3.35 Å. A graphite sheet consists of interlinked hexagons with a carbon atom at each vertex (see a sheet in Fig. 1.2). Although all C atoms are in identical chemical environments,

there are two atoms per unit cell. Each atom is endowed with one s electron and three p electrons, so each cell contains eight electrons (we neglect the core electrons from this point onward). If we use a tight-binding (TB) basis set with $|s>$, $|p_x>$, $|p_y>$, and $|p_z>$ orbitals on each atom, the Hamiltonian is diagonalized by Bloch sums of the sp^2 bond orbitals given above (with the z-direction perpendicular to the sheet plane). Fig. 1.4 shows the resulting TB band structure for graphite. The dashed line marks the Fermi energy, E_F. First and second neighbor TB parameters were used[4] which are fit to reproduce the first-principles pseudopotential local density functional graphite band structure. The two bands nearest E_F are π-bands, while the other six far from E_F are σ-bands. Since the π-bands touch E_F, the π-states are responsible for electrical conduction. The electronic density of states, $N(E)$, is shown in Fig. 1.5. Note that although $N(E_F) = 0$, $N(E)$ is nonzero for all other energies in the vicinity of E_F. Thus, graphite is a semimetal.

Looking back to the band structure, we see that the π-bands meet at the points denoted by K. These are the corners of the hexagonal first Brillouin Zone (BZ) (see Fig. 1.6). In fact, these are the only points where they meet. The Fermi surface is therefore a zero-dimensional set in the two-dimensional BZ. This is why $N(E_F) = 0$. If the sheet is doped slightly with either electrons or holes, the Fermi surface will be as shown by the dashed curves in Fig. 1.6, circles enclosing the K-points. This leads us to two important points regarding the graphite sheet Fermi surface: 1) The size of the Fermi surface is much smaller than the BZ, and 2) The Fermi surface is *not* a closed curve which surrounds the Γ-point ($k = 0$). These two facts will turn out to be very important for understanding the electronic structures of the systems we now discuss.

Prior to 1985, diamond and graphite were the only known stable forms of pure crystalline carbon to exist in bulk at standard temperature and pressure. There were, of course, graphite-like stable materials such as carbon fibers [5] and conventional soot, but these are only minor deviations from graphite. All this changed when the group

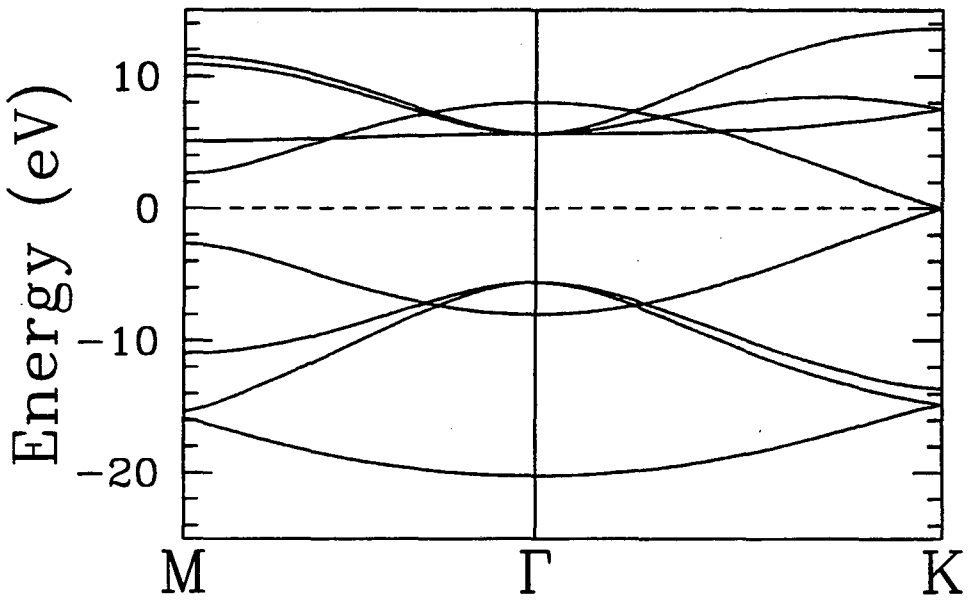

Figure 1.4: TB band structure of a graphite sheet calculated with the TB parameters of Ref. [4]. The k-space points Γ, M, and K are shown in Fig. 1.6. The Fermi energy is at zero and is marked by the dashed line.

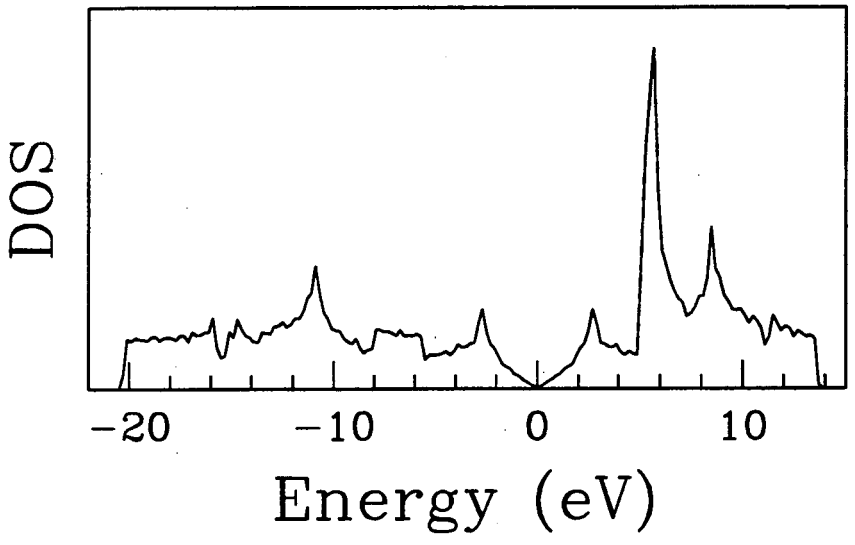

Figure 1.5: Electronic DOS of a graphite sheet calculated from the TB bands of Fig. 1.4. The Fermi level is at zero.

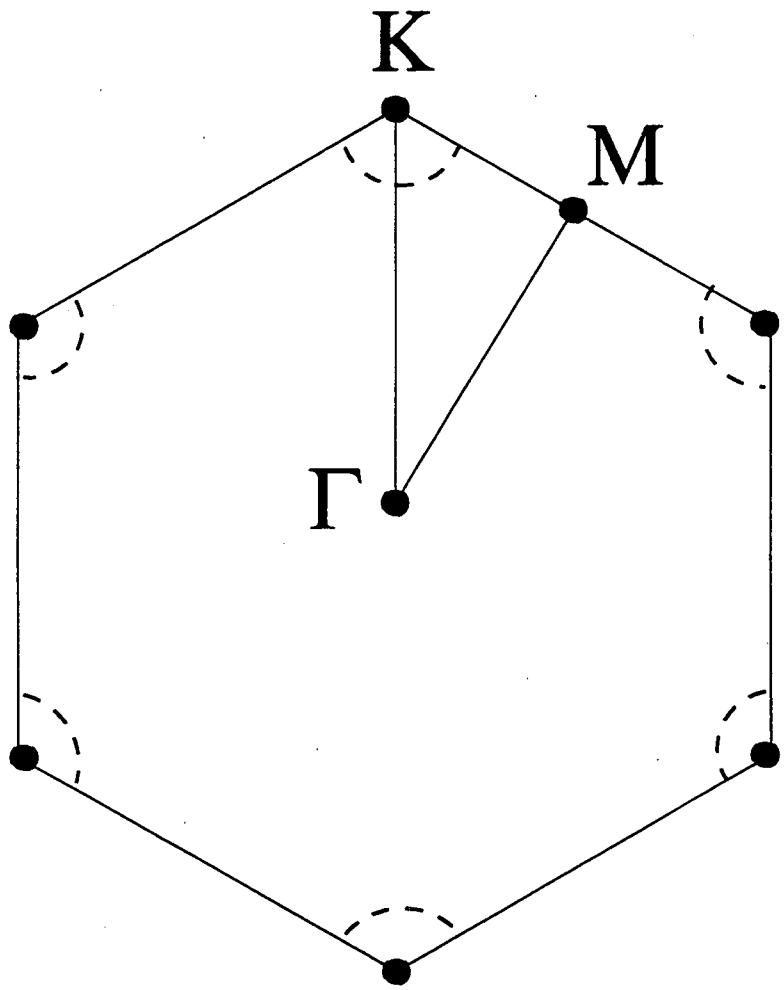

Figure 1.6: Graphite sheet BZ. Special points $\Gamma(k = 0), K$, and M are marked. For an undoped sheet, the Fermi surface is the collection of vertex points. Dashed curves indicate the Fermi surface for low-doping.

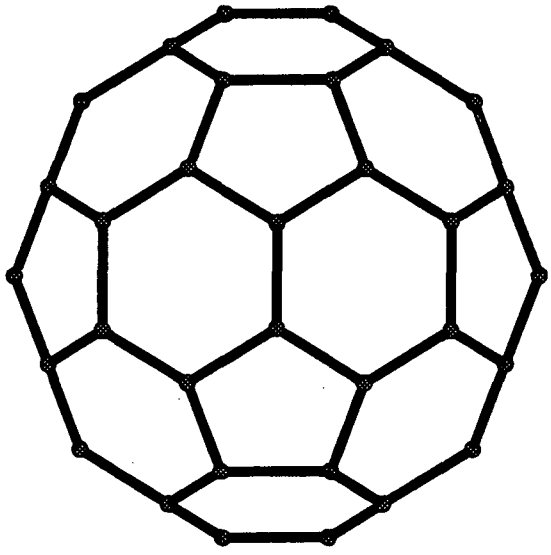

Figure 1.7: Atomic structure of C_{60}. All atoms lie on a sphere of radius 3.57 Å.

of H. Kroto, R. Curl, and R. Smalley [6] discovered a remarkably stable carbon cluster containing sixty carbon atoms. It was suggested, and subsequently verified, that its structure is that of a soccer ball as shown in Fig. 1.7. At first sight, this looks like a spherical version of single-sheet graphite. Each atom is surrounded by three nearest neighbors, and many of the atomic rings are hexagons. On closer inspection, it is seen that there are twelve pentagons as well. The closed surface topology demands this, so the bond network is somewhat different from that of graphite. An equivalent point is that the bonding is no longer perfectly planar as it is for a graphite sheet. Thus, C_{60} is a system best described as "mostly sp^2, with a small admixture of sp^3". The density of electronic states for the cluster is broadly similar to $N(E)$ for graphite. In particular, the states nearest E_F are mostly π-like, consisting of p-orbitals pointing radially outward. The curved geometry, together with the quantum confinement of electrons to a small

sphere, results in an electronic energy gap of $\sim 2-3.$ eV.

There are other stable cage-like carbon clusters which have been found as well, such as C_{70}, C_{84}, C_{94} [7], etc. All are closed graphitic surfaces with exacly twelve pentagons. As the number of atoms increases, the curvature decreases, as does the ratio of pentagons to hexagons. The graphite sheet properties are then recovered. Carbon clusters of the C_{60} variety have been termed fullerenes, for their resemblence to the geodescic dome promoted by the architect Buckminsterfuller.

One of the most important developments in fullerene research was the formation of a molecular solid of C_{60}. This was first done in 1990 by Kratschmer et al. [8], who used an arc-discharge method to make large quantities of C_{60} from graphite rods. It was subsequently shown that alkalai-doped solid C_{60} can superconduct at temperatures in excess of 30 K [9]. We will discuss many of the interesting physical properties of undoped solid C_{60} in the next chapter.

The use of the arc-discharge method to make large quantities of fullerenes gave way to another breakthrough in the field of carbon materials: the discovery of carbon nanotubes. In 1991, S. Iijima [10] found long thin whiskers of carbon growing from the cathode of his arc. They were many microns long, but only a few nanometers wide. Careful analysis with a transmission electron microscope (TEM) revealed that these so-called nanotubes are concentric circular cylinders made of rolled-up graphite sheets (see Fig. 1.8). Unlike spherical fullerene clusters, the cylindrical nanotubes are curved only along one direction, so the bond network need not contain pentagons. Two years later, the groups of Iijima and Ichihashi, and Bethune et al. [11] used transition metal catalytic particles to grow single-walled carbon nanotubes. These are individual sheets of graphite rolled into cylinders with diameters as small as 7 Å.

Besides having extremely high tensile strength, [12] carbon nanotubes are predicted to have very interesting electronic properties. Tubes with slightly different radii and helicities (the spiraling of hexagons up the tube) should have very different band gaps

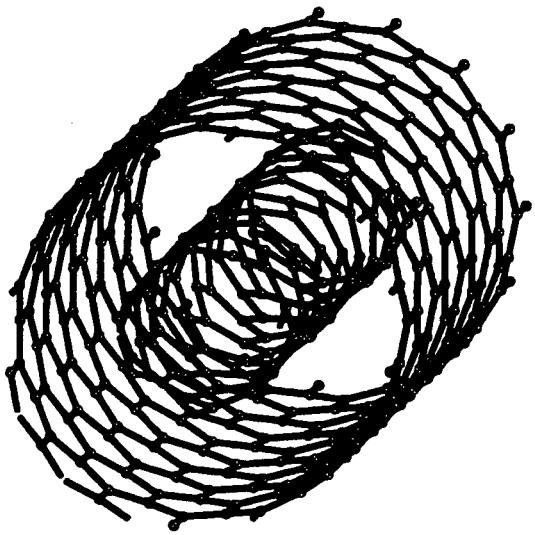

Figure 1.8: Atomic structure of a two-walled carbon nanotube. All carbon rings are hexagons.

[13, 14, 15]. This is a consequence of the two facts about the graphite sheet Fermi surface mentioned above. In particular, the electronic structure of a sheet with small disconnected regions of Fermi surface is strongly affected by the imposition of periodic boundary conditions. When the sheet is rolled into a cylinder, these boundary conditions are naturally imposed. The exotic geometric and electronic structures of carbon nanotubes should give rise to a host of interesting physical phenomena, many of which we will discuss in this work.

The remainder of this dissertation is divided into three major parts. The first concerns solid C_{60}. We begin by introducing the main facts about the system, including electronic and phonon spectra, and the orientational order/disorder transition. Then we move on to a comprehensive study of the optical absorption edge of solid C_{60}, focusing primarily on the role played by excitions. The second part is devoted to carbon nanotubes. The topic is introduced, with special attention paid to the theoretical prediction of tube band-gaps using prior knowledge about the graphite band structure. We then show how these previously derived results are invalidated when considering nanotubes with radii < 3 Å. Nanotube heterojunctions are proposed in which a tube's local electronic structure varies dramatically along its length. The low-temperature heat capacity of different nanotube samples is considered, and the static dielectric response of single-walled tubes is calculated as a function of radius and band-gap. Nanotube transport properties are then studied. The room-temperature static resistance of single-walled metallic tubes is estimated, followed by a detailed study of quantum conductance through nanotubes with vacancies, and nanotube heterojunctions. Finally, we describe a collapsed state of carbon nanotubes, and extract information regarding the graphite intersheet attractive energy. The last chapter of this work introduces pentaheptite, a pure-carbon planar covalent material consisting entirely of 5-fold and 7-fold atomic rings. We predict it to be metallic, and metastable at standard temperature and pressure.

Chapter 2

Solid C_{60}

Solid C_{60}, or fullerite, is a molecular solid of C_{60} in which the C_{60} molecules are centered on the sites of an fcc lattice. They are weakly bonded to each other with Van der Waals forces. At low temperature ($T < 260$ K), the balls are orientationally ordered in such a way that there are four C_{60} /cell [8]. This is known as the Pa3 structure. Above 260 K, the balls are orienationally disordered, but their centers remain fixed on the fcc lattice sites. The reason for this particular orientational ordering at low temperature is that the C_{60} balls have regions of high and low electronegativity. The center of each inter-pentagonal bond has the highest electron density, while the center of each pentagon-hexagon bond has the lowest. The Pa3 structure allows for electronegative sites on one ball to be close to electroposotive sites on neighboring balls, thereby minimizing the electrostatic energy. The orientational order/disorder transition temperature, 260 K, is a measure of this attraction. At room temperature, the balls are freely rotating about their centers of mass.

Before discussing the electronic structure of solid C_{60}, we mention a few facts about the electronic structure of an isolated C_{60} molecule. The single-particle C_{60} energy level spectrum is shown in Fig. 2.1 [16]. If the spectrum is examined over a large energy range, it is seen that the density of levels is broadly similar to $N(E)$ for graphite. States with energies between -5 eV and 5 eV are primarily π-states, made up of atomic p-orbitals pointing along the local normal to the sphere. Since the Fermi energy lies between two levels, C_{60} is a closed-shell molecule. All levels are 1, 3, 4, or 5-fold degenerate. This is a consequence of the icosahedral symmetry of the molecule. Each state can be classified according to irreducible representations of the icosahedral point group [17]. The HOMO

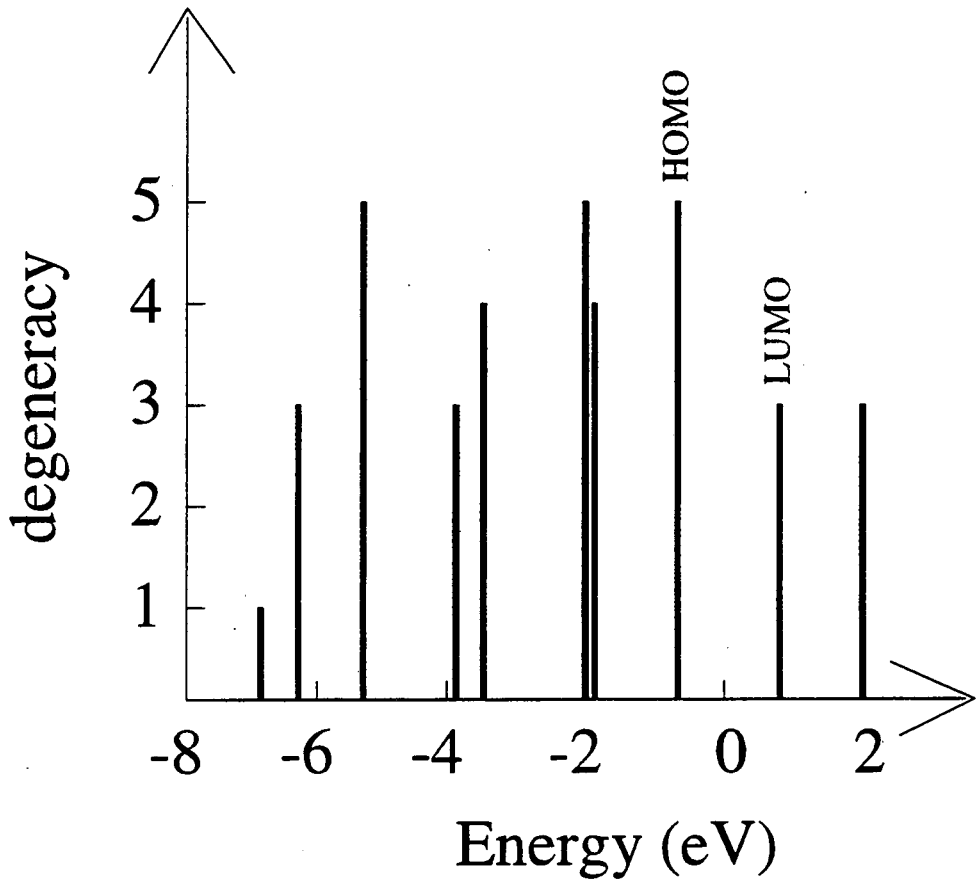

Figure 2.1: C_{60} single-particle energy level spectrum near the Fermi energy, $E = 0$. The HOMO is 5-fold degenerate, and the LUMO is 3-fold degenerate.

is 5-fold degenerate, and transforms according to the H_u representation. The LUMO is 3-fold degenerate, and is a T_{1u} state. The subscript u denotes *ungerade*, or odd under inversion about the ball center. Note that the first excited state consisting of an electron in the T_{1u} complex, and a hole in the H_u complex is odd$\otimes$odd = even. Thus, the transition from the even ground state to this excited state is dipole forbidden.

Solid C_{60} is a material of extremes; the interaction between neighboring C atoms in a C_{60} molecule is very stong, while the interaction between adjacent molecules is very weak. It is the strength of the on-ball interaction that gives rise to the large energy spread of the π-states ($\sim$ 10 eV). When many C_{60} molecules are brought together to form a solid, the isolated molecular energy levels spread out into bands. The weakness of the interball intraction is manifested in the small dispersion ($\sim$ 1 eV) of these bands. The resulting band gap is $\sim$ 2.15 eV [18, 19, 20], smaller than the HOMO-LUMO gap in the isolated molecule. It is interesting to compare this to the electronic structure of the hypothetical Fm3 phase, in which all balls have the same angular orientation, so the structure is fcc with *one* ball per cell. The Fm3 band widths are a bit larger than those of the Pa3 case [21]. This is to be expected, for the increased orientational order makes it easier for electrons to hop from ball to ball.

Just as for the electronic states, the phonons of solid C_{60} are governed by two widely different energy scales. The first is the large intra-ball stretch energy, and the second is the small inter-ball stretch energy. Calculations of Vashishta *et al.* [22] show that the modes below 15 meV are interball phonon modes, where the individual balls are undistorted, and they are moving against each other. The modes above 25 meV are primarily on-ball in character. They have extremely small dispersion, analogous to the small dispersion for electronic energy bands. Above the orientational order/disorder transition, much of the weight below 15 meV is shifted to even lower energy [22]. This is because some of these modes are librons, where the balls are rotating about their fixed centers of mass. In the orientationally disordered phase, there is little or no restoring

force for librations, so their energies approach $\hbar^2/2I \sim 10^{-4} - 10^{-3}$ meV, where I is the moment of inertia of C_{60} about its center.

In the following chapter, we will be concerned with the optical absorption edge of solid C_{60} as a function of pressure both below and above the orientational ordering temperature. We will show that the main features below the single-particle continuum are due to excitons strongly coupled to phonons. We consider excitons consisting of an electron in the T_{1u} band and a hole in the H_u band. The experimentally measured temperature dependence of the exciton lines sheds light on the strength of the electron-phonon interaction in orientationally ordered and disordered phases.

Chapter 3

Excitons and optical absorption edge

The electronic structure of solid C_{60} has attracted much interest from both theoretical and experimental points of view. Thoeretically, different approaches have been taken to study this material, including the local density approximation (LDA) [23] and the *ab initio* quasiparticle method [24]. These methods predict the same band ordering for C_{60} in the hypothetical Fm3 structure, but the band gap changes from 1.04 eV (in the LDA calculation) to 2.15 eV (in the *GW* quasiparticle picture). Experimentally, direct and inverse photoemission [18, 19, 20] give values for the gap closer to the *GW* prediction than to the LDA one. This can be compared to results of microwave conductivity experiments [25] providing excitation energies of about 1.85 eV, whereas luminescence experiments [26] report an emission band at around 1.7 eV. The discrepancy with the optical gap could be due to excitons, but this remains to be determined.

In order to investigate the properties of the absorption edge of this semiconductor, the group of G. Martinez has performed transmission measurements on fullerite single crystals grown by the group of A. Zettl. The absorption coefficient was determined as a function of pressure, temperature, and applied magnetic field strength. Fig. 3.1 displays the absorption coefficient measured at different temperatures. While the absorption edge remains structured below 260 K, it gets smeared above the orientational order/disorder transition. The magnitude of the absorption is quite weak compared to standard values for direct-gap and electric-dipole-allowed transitions in semiconductors. This is not surprising since the HOMO-LUMO gap is electric-dipole-forbidden in the isolated molecule. All transitions above 1.75 eV have a reproducible oscillator strength. However, the band around 1.7 eV is probably of extrinsic origin because its shape is

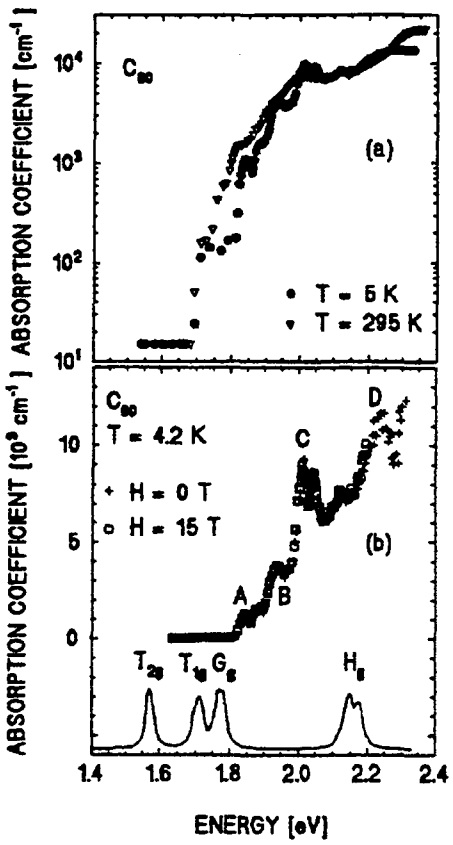

Figure 3.1: (a) Absorption coefficients of the fundemental absorption edge of fullerite at 5 and 295 K and (b) comparison between absorption curves without magnetic field and with a magnetic field of 15 T. The calculated density of states (see discussion below) for excitonic transitions is displayed in the lower part of the figure.

not conventional and its strength is significantly decreased following a heating process under vacuum.

The intrinsic transitions can be grouped in three bands around 1.86 eV (A), 1.94 eV (B), 2.03 eV (C), and a broad structure at 2.3 eV (D). In order to obtain more insight into the nature of the intrinsic transitions, a magnetic field investigation was performed. The results are shown in Fig. 3.1, where spectra at 0 and 15 T are compared. Within the experimental uncertainty ($\sim$ 0.5 meV), both spectra are identical. This result agrees with the picture of very localized excitations: if the transition takes place on a single molecule with an exciton Bohr radius of about 0.5 nm, the expected diamagnetic shift at 15 T would be less than 10^{-3} meV, which is not measurable. High-pressure experiments at low temperatures (30 K) have also been performed. Results are presented in Fig 3.2. It is found that the three excitonic peaks shift with pressure: -45 $\pm$ 5 meV/GPa (peak A), -60 $\pm$ 8 meV/GPa (peak B), and -80 $\pm$ 10 meV/GPa (peak C).These values were deduced from a linear interpolation of four measurements made between 0 and 1.5 GPa.

We present calculations modeling low-lying exciton levels in fullerite. Our approach makes no assumptions regarding the symmetries or character (Frenkel, charge-transfer, or Wannier) of excitons. Instead, we seek to determine these properties from the calculation. We consider excitons formed from a hole in the H_u-band and an electron in the T_{1u}-band. The electron-hole interaction is appropriately screened, as we will discuss. We find the energy needed to form the lowest, optically accessible (i.e., singlet) exciton is 1.58 eV, in reasonable agreement with the measured 1.83 eV [27]. The lowest several exciton levels have strong Frenkel character. The main effects influencing these levels' energies are the average H_u- T_{1u} splitting, which equals the minimum quasiparticle gap plus the mean band widths for the H_u- and T_{1u}-derived bands, and the intramolecular electron-hole attraction, which is dominated by a large monopolar part. Multipolar components of this attraction induce splittings by several tenths of an electron volt between exciton states having predominantly $T_{1u} \otimes H_u = T_{2g}$, T_{1g}, G_g and H_g total symmetries.

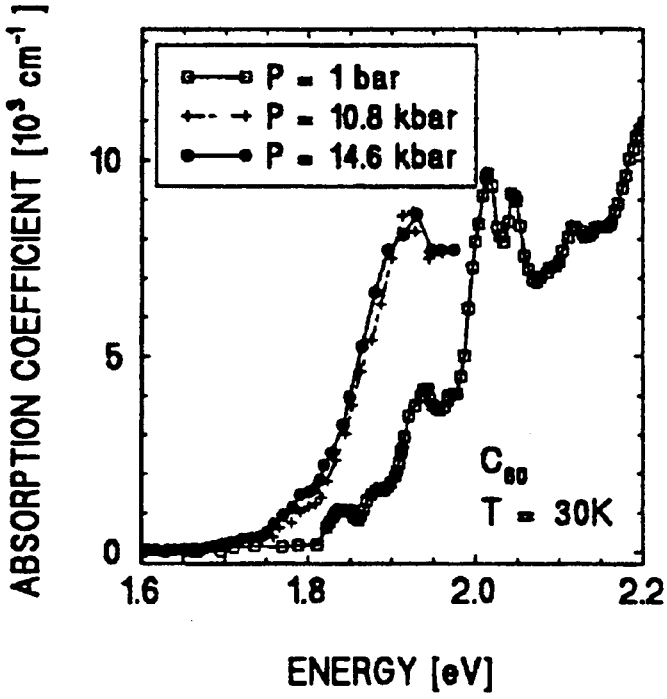

Figure 3.2: Low-temperature absorption spectra of C_{60} crystals for different values of the hydrostatic pressure.

(In the solid, unlike the molecule, such symmetries are not completely realized. However, for the Frenkel excitons, these symmetries are almost realized, so that the symmetry labels are still descriptive.) Within each group of excitons, e.g. T_{2g} excitons, we find exciton band widths ranging from 20 meV to 40 meV for the low-temperature Pa3 structure. The level schemes for triplet and singlet excitons are qualitatively similar. The interval between the lowest triplet and singlet exciton levels is found to be 0.28 eV, in agreement with the 0.28 eV found experimentally [28]. At energies immediately above the Frenkel exciton levels, we find some well defined charge-transfer exciton states which are energetically close to the quasiparticle, electron-hole continuum.

In the remainder of this chapter, we describe our approach used to model excitons, and present results for singlet and triplet excitons in the Fm3 and Pa3 crystals. We illustrate the two kinds of excitons found in this work (Frenkel and charge-transfer), and we present an estimate of pressure derivatives for excitons in Pa3 C_{60}. Several pertinent implications and aspects of the results are discussed.

3.1 Methodology

The exciton states are solutions of a Hamiltonian, H_{ex}. This Hamiltonian consists of three terms, which respectively account for the dynamics of an electron (H_{el}), of a hole (H_{hole}), and of the electron-hole interaction (H_{e-h}):

$$H_{ex} = H_{el} + H_{hole} + H_{e-h}. \tag{3.1}$$

Individually, H_{el} and H_{hole} would govern the dynamics of independent quasiparticles: a single conduction-band electron or valence-band hole in a fullerite crystal. These dynamics are described using a Slater-Koster parameterization of ab initio quasiparticle results, presented earlier [24]. Specifically, we have

$$H_{el} = \sum_{\mathbf{R}i} \left(\epsilon_e a^+_{\mathbf{R}i} a_{\mathbf{R}i} + \sum_{\mathbf{R}'i'} (t_e^{\mathbf{R}-\mathbf{R}'})_{i,i'} a^+_{\mathbf{R}i} a_{\mathbf{R}'i'} \right), \tag{3.2}$$

where $\mathbf{R}$ and $\mathbf{R}'$ indicate unit cells of the crystal, and i and i' indicate T_{1u} orbitals of the various molecules in each unit cell. Indices i and i' also include spin degrees of freedom. Here ϵ_e is the T_{1u} term energy. The t's are transfer (or hopping) integrals between molecular orbitals (MO's) on neighboring molecules, so these are non-zero only when $\mathbf{R}$ and $\mathbf{R}'$ are close. We neglect nonorthogonality of MO's on different molecules. Operators a^+ and a are electron creation and annihilation operators for the various MO's. Analogously, for holes we have

$$H_{hole} = \sum_{\mathbf{R}i} \left(\epsilon_h b^+_{\mathbf{R}i} b_{\mathbf{R}i} + \sum_{\mathbf{R}'i'} (t_h^{\mathbf{R}-\mathbf{R}'})_{i,i'} b^+_{\mathbf{R}i} b_{\mathbf{R}'i'} \right). \tag{3.3}$$

Based on quasiparticle calculations, the average H_u-T_{1u} splitting, $\epsilon_e - \epsilon_h$, is about 3.03 eV in fullerite, whereas the measured value of this quantity ranges from 3.5 eV [20] to 3.7 eV [29]. We use the theoretical value of 3.03 eV in the present analysis.

Because of the complexity of the electron-hole interaction, we describe it in four stages. First, we describe ways of subdividing the electron-hole interaction in order to facilitate its calculation. Next, we discuss interactions between the electron and hole when they are on different molecules. Then we consider the case of the electron and hole on the same molecule. Finally we discuss how solid-state screening effects renormalize the electron- hole interaction. After discussing the form of the electron-hole interaction, we briefly mention how the exciton Hamiltonian is solved.

Our notation is defined as follows. Electron and hole motion are coupled by H_{e-h}, which we write as:

$$H_{e-h} = H^{(1)}_{e-h} + H^{(2)}_{e-h}, \tag{3.4}$$

where

$$H^{(1)}_{e-h} = \sum_{\mathbf{R}i} \sum_{\mathbf{S}j} \left[(1 - \delta_{\tau_{\mathbf{R}_i}, \tau_{\mathbf{S}_j}}) W(\tau_{\mathbf{R}_i} - \tau_{\mathbf{S}_j}) a^+_{\mathbf{R}_i} b^+_{\mathbf{S}_j} b_{\mathbf{S}_j} a_{\mathbf{R}_i} \right], \tag{3.5}$$

and

$$H^{(2)}_{e-h} = \sum_{\mathbf{R}i} \sum_{\mathbf{S}j} \left[\delta_{\tau_{\mathbf{R}_i}, \tau_{\mathbf{S}_j}} \sum_{i',j'} \xi_{ii',jj'} a^+_{\mathbf{R}_i} b^+_{\mathbf{S}_j} b_{\mathbf{S}_{j'}} a_{\mathbf{R}_{i'}} \right]. \tag{3.6}$$

Here, $\tau_{\mathbf{R}i}$ denotes the location of the molecule associated with the i-th T_{1u} MO in the $\mathbf{R}$-th unit cell; there is a corresponding definition for $\tau_{\mathbf{S}j}$ which involves the H_u MO's. This division of H_{e-h} into $H_{e-h}^{(1)}$ and $H_{e-h}^{(2)}$ is a division into effects occurring when the electron and hole are on the same and different molecules, respectively.

A different conceptual subdivision of the electron-hole interaction is also worth noting. The interaction may be divided into *direct* and *exchange* parts [30]. This distinction is important, since one must carefully consider how each part is to be screened. In this work, H_{ex} is really an effective Hamiltonain describing the low-lying excitons formed from $H_u \longrightarrow T_{1u}$ electron promotions. All virtual promotions besides $H_u \longrightarrow T_{1u}$ serve to renormalize the properties of the H_u hole and T_{1u} electron, and lead to a new effective electron-hole interaction which is reflected in H_{ex}. In the C_{60} molecule, whether in the vapor phase or solid state, care must be taken to include the effects of these many other, possible promotions: only these promotions are treated collectively in screening the exchange effective electron-hole interactions, whereas *all* promotions are treated collectively in screening of the effective direct interactions.

This particular screening of the exchange parts would not be appropriate in treatments of excited states of molecules and solids involving the full Hamiltonians with bare electrons and holes [30, 31]. Yet, as described above, we use an effective Hamiltonian which treats only the dynamics of the T_{1u} electron and H_u hole with an effective fundamental interaction that is screened by the remainder of the system. Our screening of the exchange parts is not novel. It is highly analogous to a similar screening of the effective fundamental interaction between valence electrons within the core-polarization-potential fashion of core- valence partitioning (as well as analogous to the screening of the fundamental interaction between π-electrons when σ and π electrons have been similarly partitioned). As was explicitly derived within the core-polarization- potential framework, evaluation of the dielectric response of a semiconductor using the random-phase approximation resulted in a screening, because of core-polarization effects, of the

exchange part of the (valence) electron-(valence) hole interaction [32]. [To clarify this (standard) terminology, we note that only the exchange part of the electron-hole interaction is included within the random-phase approximation.]

Consider the case when $\tau_{\mathbf{R}i}$ and $\tau_{\mathbf{S}j}$ correspond to different molecules. Then for the screened interaction, W, we include interactions between the monopole moments of the T_{1u} or H_u charge distributions on each molecule. This screened interaction includes a term equal to $-e^2/[4\pi\epsilon_0|\tau_{\mathbf{R}_i} - \tau_{\mathbf{S}_j}|]$, plus a term accounting for solid-state screening effects, which will be described below. Our $H^{(1)}_{e-h}$ affects the direct part of the electron hole interaction, because of the minimal spatial overlaps between orbitals on different molecules.

One might also consider multipolar contributions to intermolecular Coulomb integrals. Such contributions could influence exciton band widths. However, we presume that they are quite small, and do not consider them further. In our model, therefore, exciton band widths are determined by single-particle hopping through H_{el} and H_{hole}. A Frenkel exciton can move from one molecule to its neighbor via successive hops of the electron and hole.

If $\tau_{\mathbf{R}_i}$ and $\tau_{\mathbf{S}_j}$ correspond to the same molecule, the electron- hole interaction is of the form:

$$\xi_{ii',jj'} = \delta_{ii'}\delta_{jj'}\left[\Phi_0 - A \times \left(\frac{e^2}{4\pi\epsilon_0 R_0}\right)\right] + A\zeta^D_{ii',jj'} + A'\zeta^X_{ii',jj'}. \qquad (3.7)$$

The term Φ_0 accounts for the solid-state screening effects which occur when the electron and hole are on the same molecule. The parts scaled by the factor A represent monopole (first term) and multipole (second term) contributions to the intramolecular, direct electron-hole interaction. The parts scaled by the factor A' represent multipole parts of the intramolecular, exchange electron-hole interaction. Modulo scalings by A or A', intramolecular interactions are computed within the Parr-Pariser-Pople approach [33], which involves a parametrization of multi-center Coulomb integrals for π-electron

systems. Ref. [33] presents several sets of parameters appropriate for use in calculations with neglect of differential overlap, an assumption made in this work. We use parameters given by Löwdin, whereas a different set of semi-empirical parameters gives somewhat different results. To illustrate this, approximate level schemes for triplet and singlet excitons in the Pa3 structure are shown in Fig. 3.3 as we continuously interpolate between Löwdin's and the semi-empirical parameters [33]. Notably, the nearly degenerate T_{1g} and T_{2g} singlet levels can change order.

One may be justifiably concerned with the use of intramolecular electrons, based on studies of benzene, in the study of C_{60}. However, the parameters are fairly independent of the π-electron system studied, in part since the associated Coulomb integrals approach a form of e^2/d, where $d > 0.3$ nm is the distance between two carbon atoms. Therefore, the systematic uncertainty of our extrapolation of parameters from benzene to C_{60} is indicated by the effects in the above comparison of Löwdin's parameters and the semi-empirical parameters. To improve precision would require detailed, quantum-chemical treatment of intramolecular correlation that is well beyond the scope of this work.

In Fig. 3.3 and throughout this work, intramolecular direct integrals are scaled by the factor A, to achieve the correct interaction as determined from measurements of the lowest triplet state in vapor-phase C_{60}. Haufler et al. [34] found that the lowest triplet state lies 1.7 eV above the molecular ground state in the vapor phase. With an ionization potential, 7.6 eV [35], and electron affinity, 2.7 eV [36], this implies an electron-hole attraction energy of 7.6 eV - 2.6 eV - 1.7 eV = 3.3 eV. Without any scaling, the Löwdin parameters would give an attraction energy of 3.98 eV. Therefore, we use $A = 0.83$ for those parameters. This scaling compensates for the lack of a more complete treatment of intramolecular correlation effects.

The scaling of the exchange parts of the electron-hole interactions by the factor A' requires further motivation. We cannot have $A' = A$ exactly, because A reflects screening effects via all virtual $H_u \longrightarrow T_{1u}$ promotions, whereas A' should not. Rather,

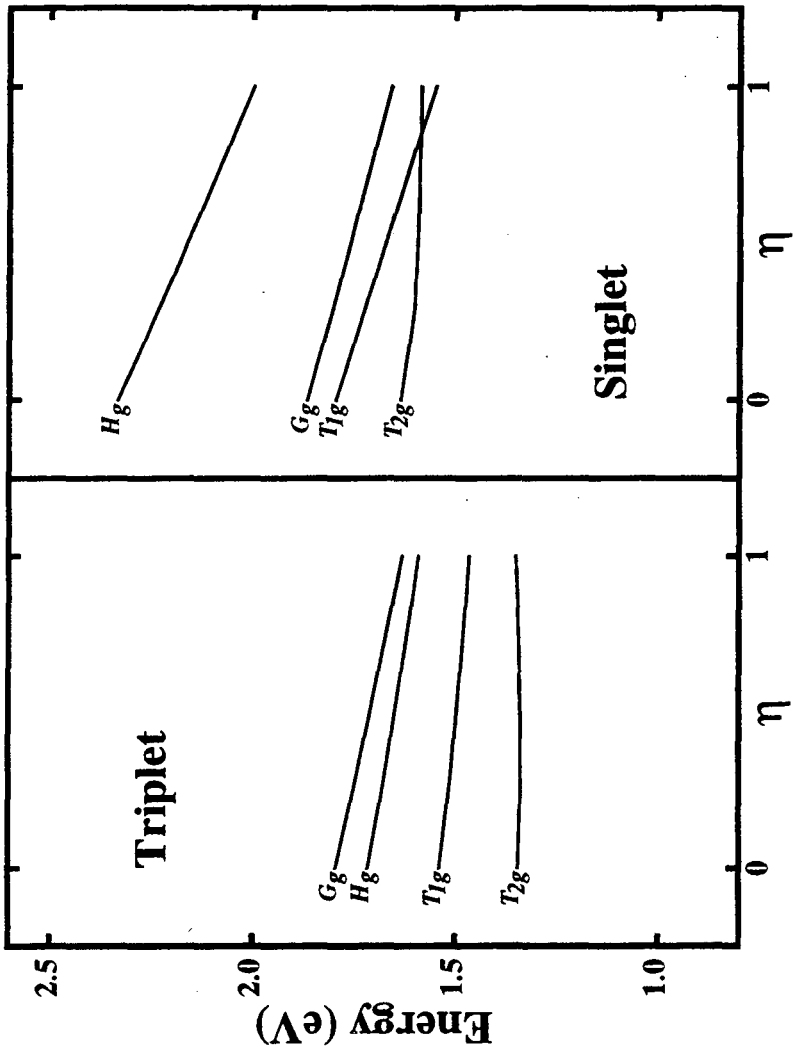

Figure 3.3: Approximate dependence of approximate singlet and triplet level schemes (for crystal momentum, $\mathbf{q} = 0$, in the Pa3 structure) on the Parr-Pariser- Pople parameters used for π-electron multi-center intergrals. The parameter η defines the admixture of Löwdin and semi-empirical (cf. Ref. [33]) parameters used in weighted average of these two sets, where Löwdin's parameters are given weight $(1-\eta)$, and the latter, weight η. Exciton symmetries are indicated, and splittings within each complex (e.g. T_{2g}) are suppressed in the presentation, to clarify the dependence of results on the parameters.

we would expect $A < A' < 1$. However, because A is close to 1 and because of the great number of promotions other than those $H_u \longrightarrow T_{1u}$ promotions which form excitons, many of which are only a few electron volts above the band gap, we expect $A' \sim A$. The validity of such an approximation is supported a posteriori by the accuracy of our predicted $^3T_{2g} \longrightarrow ^1T_{2g}$ interval. Although it is conceptually important that A and A' differ, better knowledge of the latter is not helpful in this system: because variation of A throughout its possible range would affect the exciton-level energies by percents of an electron volt, any uncertainty in A' will contribute minimally to our other systematic uncertainties.

We now discuss solid-state screening effects on W in $H^{(1)}_{e-h}$ and $H^{(2)}_{e-h}$, and the evaluation of Φ_0. Consider H_{e-h} acting on a given configuration in which the electron and hole are respectively in some pair of T_{1u} and H_u MO's. There may be multipolar contributions to intramolecular electron-hole interactions. Beyond that, the form of H_{e-h} implies that its action is simply multiplicative; it will not produce a different configuration. This multiplicative action of H_{e-h} is modified by solid-state screening effects, which are effective screening of the electron-hole interaction via induced molecular dipoles. Each molecule develops a dipole because of the fluctuating electric fields of the electron, the hole, and other molecular dipoles. However, solid-state screening effects are presumably negligible for intramolecular multipolar interactions between the electron and hole.

For computing solid-state screening effects, electric fields of the electron and hole may be approximated by the associated MO's having spherical probability distributions on each molecule. This leads to polarization of molecules in the vicinity of the electron or hole, whereas there is no contribution by a particle to the electric field at the center of a MO's probability distribution. Also, interactions between molecular dipoles are assumed to be adequately treated in a point-dipole picture [37]. Suppose the electron and hole are located on molecules at positions τ_e and τ_h, while the molecular dipole of

a molecule at position τ is indicated by $\mathbf{p}(\tau)$. Then we have,

$$\mathbf{p}(\tau) = \frac{\alpha}{4\pi\epsilon_0}\left[\frac{e(\tau_e-\tau)}{|\tau_e-\tau|^3} - \frac{e(\tau_h-\tau)}{|\tau_h-\tau|^3} - \sum_{\tau'}\nabla_\tau(\mathbf{p}(\tau')\cdot\nabla_{\tau'})\frac{1}{|\tau-\tau'|}\right]. \qquad (3.8)$$

Given electron and hole coordinates, all molecular dipoles are determined simultaneously and self-consistently using the above relation. We use the theoretical, static molecular polarizability, α, and restrict ourselves to linear response theory. The value of α used, given by Pederson and Quong [38], includes all intramolecular electron-electron interactions within the random phase approximation. Computation of solid-state screening effects follows straightforwardly for a finite solid. Application of appropriate boundary conditions permit us to extrapolate these effects to what they would be in an infinite solid, or as is appropriate at a surface, a semi-infinite solid.

The induced dipoles' potential is the sum of a potential induced by the electron and a potential induced by the hole. To obtain solid-state screening effects on the electron-hole interaction, we include half of the dipoles' potential as felt by the electron, which would arise because of the hole alone, and half of the dipoles' potential felt by the hole, which would arise because of the electron alone. (These two terms are equal within the model. The electron and hole self-energy effects, i.e. effects of each particle feeling the dipole potentials caused by itself, are already incorporated in the model through H_{el} and H_{hole}.)

The solid-state screening effects involve a dynamical screening of the electron-hole interaction: these effects depend on the fluctuating electron and hole coordinates, as opposed to the expectation value of the total, exciton charge distribution. This fact notwithstanding, we only need to use the static molecular polarizability in the present model, since electron and hole dynamics are slow compared to the dynamics of the relevant collective electronic molecular excitations. At large $|\tau_e - \tau_h|$, the solid-state screening effects converge to the correct, asymptotic limit, in which the electron-hole interaction is $-e^2/[(4\pi\epsilon)|\tau_e - \tau_h|]$, where ϵ, the dielectric constant, is related to the

molecular polarizability, α, through the Clausius-Mossotti relation.

We solve H_{ex} with the following, general form of exciton wave function:

$$|\Psi_{n\mathbf{q}}>=\sum_{\mathbf{R}} e^{i\mathbf{q}\cdot\mathbf{R}} \sum_{\mathbf{S}} \sum_{i,j} C^{n\mathbf{q}}_{\mathbf{S};i,j} a^{+}_{\mathbf{R}i} b^{+}_{(\mathbf{R}+\mathbf{S})j} |0> . \qquad (3.9)$$

The exciton has total crystal wave vector, $\mathbf{q}$, which is a good quantum number in a periodic system; n distinguishes the various exciton states having a given $\mathbf{q}$. Summation of $\mathbf{R}$ over unit cells establishes the crystal wave vector of the exciton, and summation over values of $\mathbf{S}$ permits the hole and electron to be in different unit cells. In practical calculations, we truncate the range of $\mathbf{S}$, and this truncation is progressively relaxed to insure that each exciton wave function achieves the desired degree of relative electron-hole separation. By summing over i and j, we consider every possible pair of H_u and T_{1u} MO's lying within each pair of unit cells, $\mathbf{R}$ and $\mathbf{R}+\mathbf{S}$. Operators a^+ and b^+ act on the crystal ground-state wave function to create all desired electron-hole pairs states. The C-coefficients weigh these pair states according to their amplitudes in the stationary solutions of H_{ex}. Solution for singlet or triplet exciton levels may be carried out using pre-selected combinations of the C-coefficients which project onto a given $S-S_z$ subspace. Solving H_{ex}, which in this work involves evaluating up to about 10,000 degrees of freedom, is accomplished by iterative diagonalization techniques. Exploiting the sparseness of H_{ex} significantly reduces the required computational resources.

In the set-up of H_{ex}, one must be careful to include time-reversal effects when describing the hole dynamics, if these dynamics are derived from an electron band structure. Also, one needs to be mindful of possible phase shifts related to $\mathbf{q}$ when the electron or hole move between adjacent unit cells. Finally, care must be taken to account for the Fermi statistics in the signs of H_{e-h} matrix elements for singlet- and triplet-exciton cases. Due attention to all of these issues is tedious but straightforward.

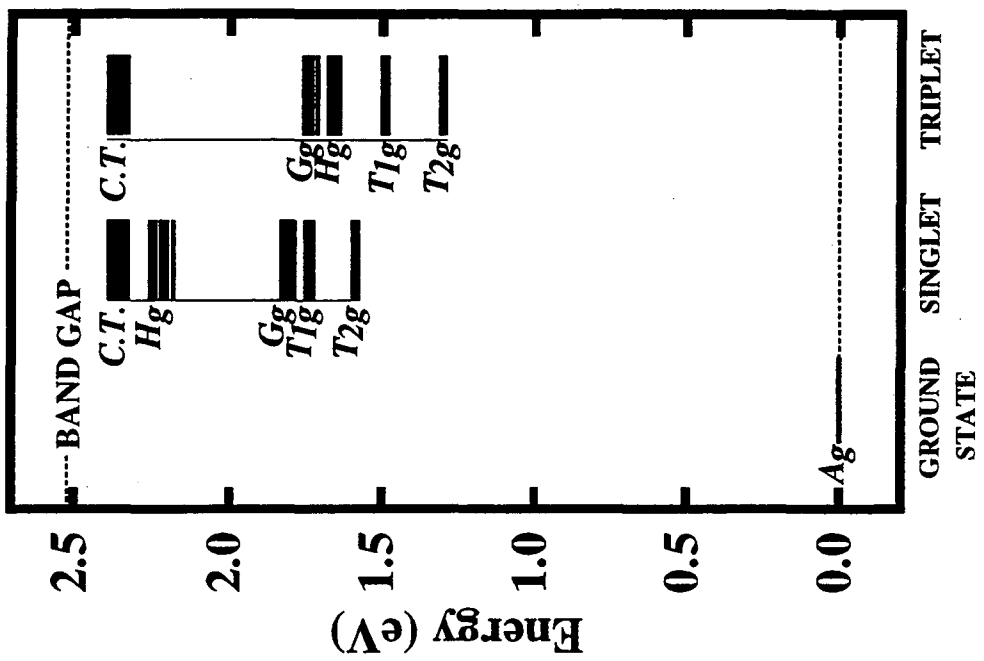

Figure 3.4: Level scheme (for crystal momentum, $\mathbf{q} = 0$) singlet and triplet excitons in Pa3 structure of C_{60}. Symmetries of Frenkel exciton levels are indicated. Higher-lying, charge-transfer excitons, whose formation requires about 2.33 eV excitation, possess more similar level schemes for singlet and triplet states. The quasiparticle band gap is indicated (at 2.52 eV), although this gap is not neccessarily direct in the Pa3 structure.

3.2 Results

Except for the results in Fig. 3.3, all results are based on Löwdin's parameters [33]. In Fig. 3.4, we present computed level schemes for singlet and triplet excitons in Pa3 C_{60} [39]. In the Fm3 structure, the lowest exciton levels are typically 0.05 eV lower than those given in Fig. 3.4. Experimentally, the lowest triplet and singlet excitons for Pa3 C_{60} have energies of 1.55 eV and 1.83 eV, respectively. Here, they are predicted to be 1.30 eV and 1.58 eV, respectively. The singlet-triplet splitting is

therefore accurately predicted. While we find the lowest singlet exciton levels have T_{2g} symmetry, the T_{1g} excitons are quite close energetically, and the relative ordering of excitons with these two symmetries depends sensitively on the detailed treatment of the interactions, as discussed previously and illustrated in Fig 3.3. In these regards, one might also compare the various results cited in Ref. [39]. Therefore, our results do not establish which symmetry corresponds to that of the lowest-lying, singlet exciton.

In Fig. 3.5, we illustrate the dependence of exciton-level energies on the maximum allowed electron-hole separation. Compared to when the electron and hole are constrained to be on the same molecule, the energies of the actual Frenkel excitons are lowered by 0.1 eV to 0.2 eV. This lowering may be estimated by using second-order perturbation theory. We consider as an unperturbed Hamiltonian one which is equal to H_{ex}, but with all transfer integrals reset to zero, and we include effects of the transfer integrals perturbatively. In order of increasing energy, stationary solutions of such a zero-transfer-integral Hamiltonian are excitons with purely Frenkel character, then excitons with purely charge-transfer character, and so forth. Once one includes the true transfer integrals as a perturbation, the energies of Frenkel excitons will be affected by approximately $Z|t|^2/(U-V)$. Here, Z is the molecular coordination number, and t is a typical transfer-integral magnitude. U and V are the electron-hole interaction when the electron and hole are on the same molecule and on adjacent molecules, respectively. Both U and V are negative, and U is larger in magnitude than V.

Correspondingly, one would expect exciton band widths to be larger in the Fm3 crystal than in the Pa3 crystal, because transfer integrals (and electron and hole band widths) are larger in the former structure. We find this to be the case. For example, the T_{2g} exciton band width is roughly 60 meV in the Fm3 structure, vs. roughly 20 meV in the Pa3 structure. We present the exciton bands for the Pa3 structure in Fig. 3.6. (The energies of Frenkel excitons should likewise be lower in the Fm3 structure than in the Pa3 structure, as has already been noted.)

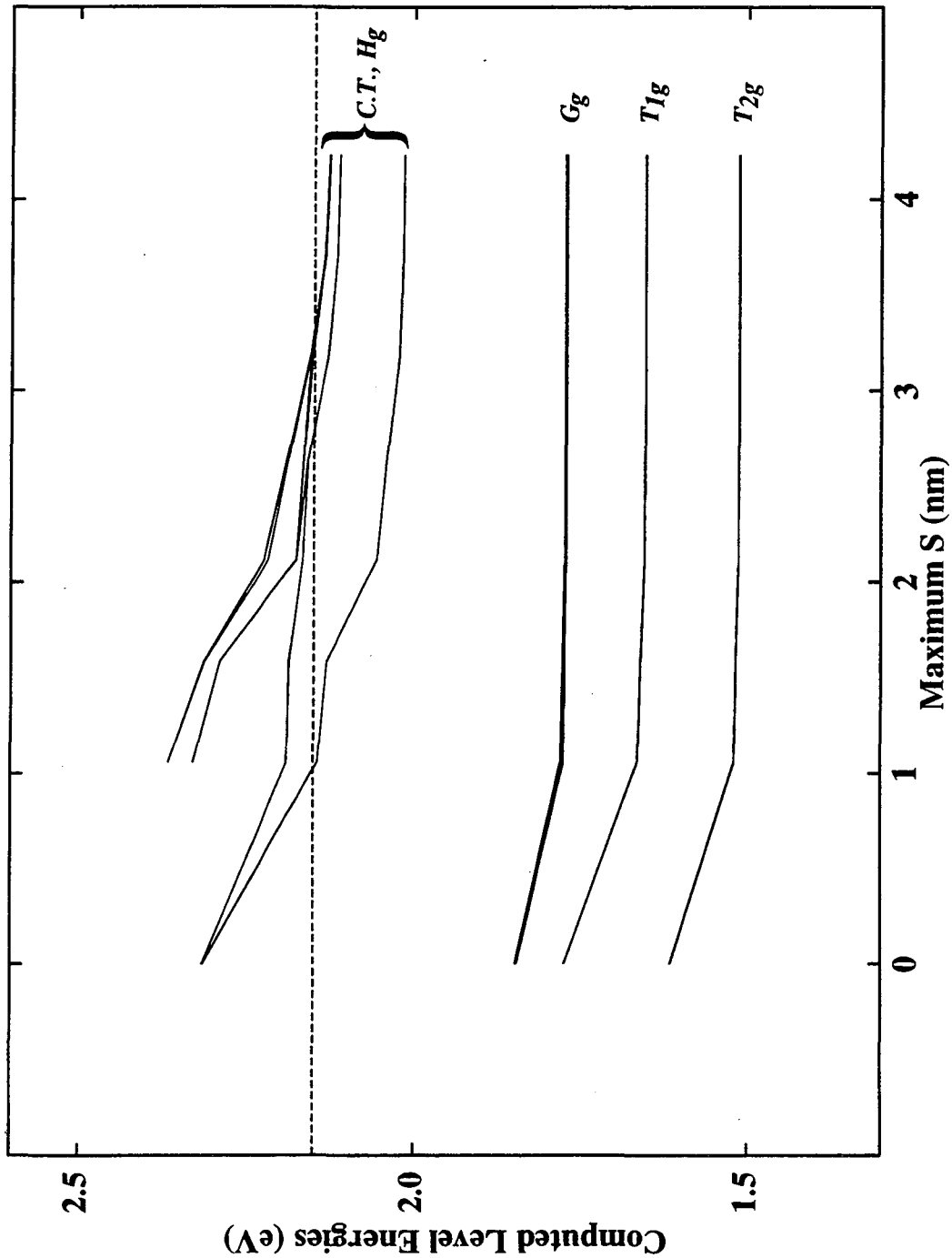

Figure 3.5: Dependence of ($\mathbf{q} = 0$) exciton energies, in Fm3 structure, on the maximal range of wave-function cut-off, **S**. As suggested by this plot, only the T_{2g}, T_{1g} and G_g, singlet excitons have nearly complete Frenkel character in the Fm3 structure, whereas the H_g excitons acquire considerable charge-transfer character. The horizontal, dashed line indicates the theoretical, Fm3 quasiparticle band gap.

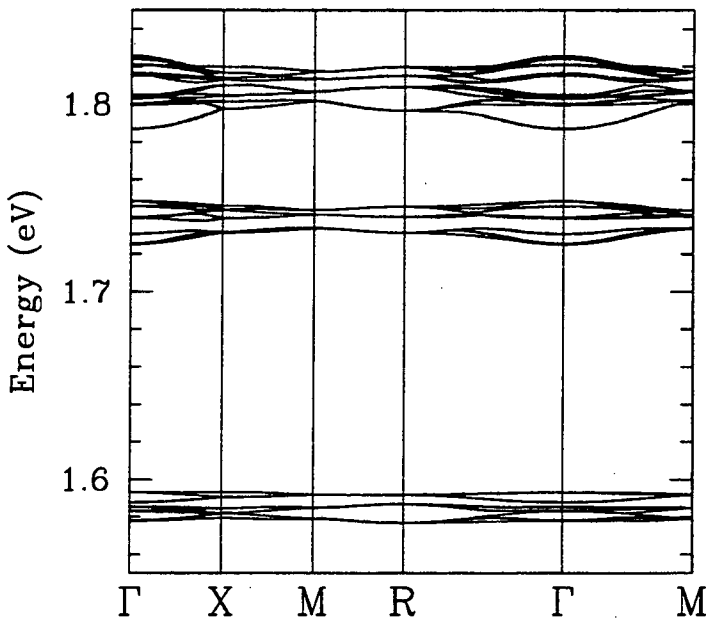

Figure 3.6: Exciton energy bands in Pa3 structure of C_{60}. In order of increasing energy, the bands depicted are for singlet excitons with T_{2g}, T_{1g} and G_g symmetry. In units of $2\pi/a$, where a is the lattice constant,Γ, X, M and R correspond to crystal momenta (0,0,0), (1/2,0,0), (1/2,1/2,0), and (1/2,1/2,1/2).

Using the present model, we can estimate the pressure derivatives of exciton energies. Pressure derivatives arise from the dependence of transfer integrals on the separation between adjacent molecules. Within local-density-functional theory [40], which reliably estimates the effects of compression on band energies [41], H_u and T_{1u} band widths vary (approximately) inversely with the third power of the molecular volume [42]. Therefore, the effects of intermolecular hopping on exciton energies should vary inversely as the sixth power of the molecular volume, since they vary as the squares of the transfer integrals. If we take the bulk-modulus of solid C_{60} to be 10.3 GPa [43], the model predicts that the pressure derivatives for T_{2g}, T_{1g} and G_g exciton energies for Pa3 C_{60} are -44 meV/GPa, -44 meV/GPa, and -54 meV/GPa, respectively. This is in reasonable agreement with the observed pressure derivatives, -45 meV/GPa $\pm$ 5 meV/GPa, -60 meV/GPa $\pm$ 8 meV/GPa, and -80 meV/GPa $\pm$ 10 meV/GPa, of the three spectral features near the absorption edge of the Pa3 structure [27].

3.3 Discussion

A strong Frenkel character of low-lying excitons in the fullerites is suggested by experiments measuring the Zeeman effect [27], and by the remarkable similarity of optical absorption spectra for C_{60} in the solid state and dissolved in n-hexane as well as other solutions [44]. Whereas optical spectra primarily probe singlet excitons, we note that the 1.55 eV required to form a triplet exciton in the solid in electron energy-loss experiments is close to the 1.7 eV required in the vapor phase. These C_{60} Frenkel excitons are aptly described in the fashion used by Knox [45] regarding Frenkel excitons in other molecular solids. That is, the formation of an exciton does not necessarily imply a substantial alteration in the charge distribution in the solid, but perhaps only a more subtle rearrangement of internal molecular degrees of freedom. On the simplest level, energies required for formation of both triplet and singlet excitons exhibit a 0.1 eV to

0.15 eV downward shift in the solid, if one considers results for isolated C_{60} molecules and C_{60} molecules in the solid state. This red-shift is commonly attributed to the Frenkel excitons having some charge-transfer character in the solid.

An unresolved issue in this work which we have yet to mention is the role of quantized vibrations in measured excitation spectra. Phonons are believed to account for the observed cross-sections for creating the lowest-lying, parity-forbidden excitons by optical means, whereas electric-quadrupole effects would produce much smaller cross-sections. Vibrations also cause absorption spectra to exhibit many more lines than the discrete lines predicted theoretically, which is direct evidence for Herzberg-Teller mechanisms. The variation of the absorption coefficient for the exciton bands reflects the relative electron-phonon coupling strength, since simple consideration of excitonic density of states (Fig. 3.1) do not explain the differences.

The electron-phonon interaction is also evident in the temperature variation of the optical transitions. We can write, for any transition energy E_0 (Ω is the system volume):

$$\left(\frac{\partial E_0}{\partial T}\right)_P = \frac{1}{\Omega}\left(\frac{\partial \Omega}{\partial T}\right)_P \Omega \left(\frac{\partial E_0}{\partial \Omega}\right)_T + \left(\frac{\partial E_0}{\partial T}\right)_\Omega, \tag{3.10}$$

where the temperature coefficient is decomposed into an extrinsic part (first term above) due to thermal expansion of the lattice at constant pressure, and an intrinsic part due to the electron-phonon interaction at constant volume. The extrinsic part can be evaluated with the temperature-dependent thermal expansion coefficient [46], the bulk modulus for the different phases [43], and the pressure coefficient of the transition energy. These quantities are not determined with good accuracy and are temperature dependent (especially across the phase transition). We assume constant values for them, and have checked that our conclusions do not depend on this crude choice. The integral,

$$I_{el-ph} = \int_0^T \left(\frac{\partial E_0}{\partial T}\right)_\Omega dT \tag{3.11}$$

can then be evaluated for different values of the absorption coefficient specific to the structures A, B, and C. The results are displayed in Fig. 3.7. It is clear that the intrinsic

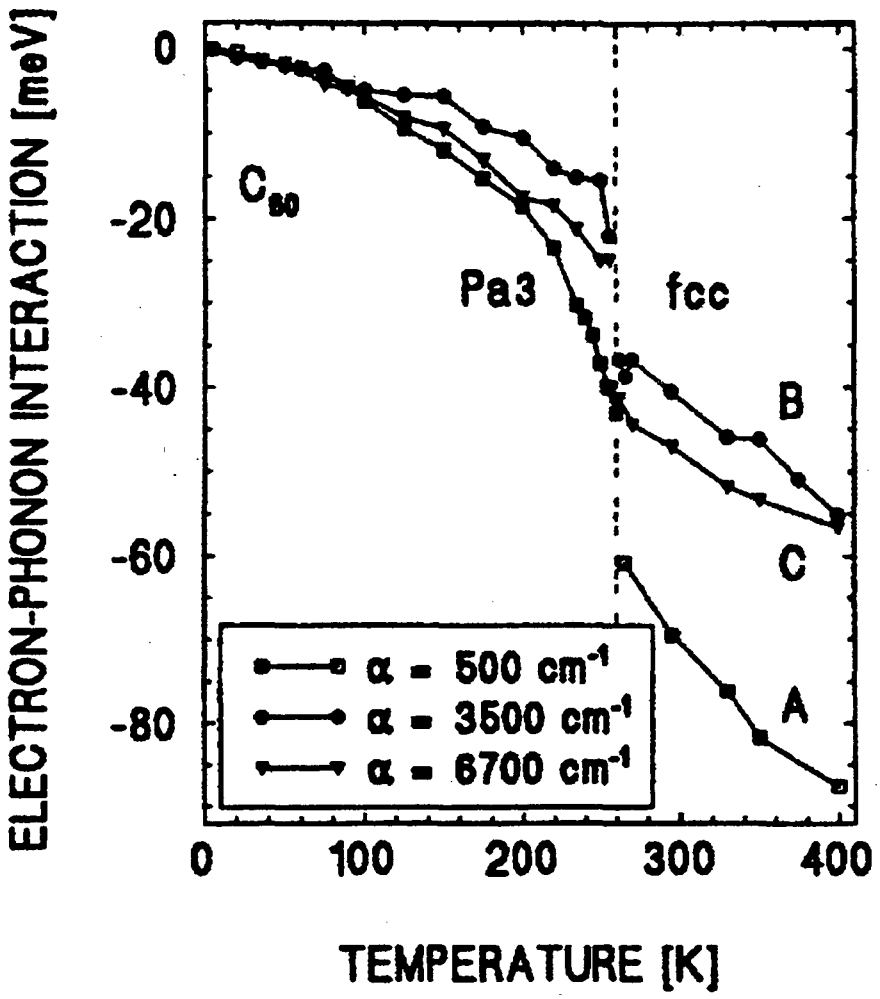

Figure 3.7: Intrinsic contribution of the electron-phonon interaction to the transition energy vs. temperature for constant values of the absorption coefficient α.

part of I_{el-ph} is a monotonically increasing function of temperature that undergoes an abrupt increase at the orientational order/disorder phase transition. This interaction is also specific to the symmetry of the excitonic state and appears to be significantly more important for the exciton A.

The increase of I_{el-ph} with temperature can be understood from the theories of Fan, and Brooks and Yu [47], as applied to excitonic states. In this description, electronic states, renormalized by phonons, are shifted to lower energy. As temperature increases, the phonon occupation numbers increase, leading to a larger shift in the exciton energies. The discontinuity in the energy shifts at the structural phase transition is most likely a result of the discontinuous change in the low-energy phonon spectrum, as calculated in Ref. [22].

3.4 Conclusions

In summary, we have calculated the properties of excitons in undoped solid C60. Our model involves a conduction-band T_{1u} electron and a valence-band H_u hole, whose motions are coupled by their mutual attraction. The isolated dynamics of the particles were described previously within a quasiparticle approach. The electron-hole attraction is modeled using a screened Coulomb interaction. Intramolecular electron-hole interactions are described using a semi-empirical Parr-Pariser-Pople scheme. These and intermolecular electron-hole interactions are screened by the lattice of polarizable molecules.

We predict that the lowest-lying excitons exhibit a strong Frenkel character, whereas some higher-lying excitons exhibit a distinct charge-transfer character. The results for Frenkel excitons are consistent with previous studies dealing with isolated C_{60} molecules [39]. The lowest triplet and singlet excitons are found to have T_{2g} symmetry, and can be formed with an excitation energy of 1.30 eV and 1.58 eV, respectively. These energies differ from the experimentally measured values by 0.25 eV, and the singlet-triplet

splitting is accurately predicted. In our results, the T_{2g} and T_{1g} singlet excitons lie close in energy, and their ordering is sentitive to the precise Parr-Pople-Pariser parameters used, so this work does not establish which is actually the lowest. Within the singlet and triplet cases, the exciton states characterized by different symmetries (T_{2g}, T_{1g}, G_g and H_g) span an energy range of several tenths of an electron volt. As a function of crystal momentum, exciton energy levels disperse by about 20 meV in the Pa3 structure.

Since the average HOMO-LUMO separation in solid C_{60} is around 3 eV, the intramolecular electron-hole interaction (or electron-hole, "Hubbard U" parameter) is about -1.5 eV. Just as for the electron quasiparticle states in this molecular solid, the properties of excitons exhibit a coexistence of features which are characteristic of single molecules and of extended systems.

Chapter 4

Carbon nanotubes

Carbon nanotubes are circular cylinders formed from graphite sheets. At the time of this writing, there are three major types of carbon nanotube samples which have been produced in the laboratory. The first is multi-walled tubes [10]. These are concentric cylindrical tubes with at least two walls, inner radii $\sim 10 - 100$ nm, and can be up to hundreds of microns in length. A TEM image of such a tube is shown in Fig. 4.1. The distance between adjacent concentric walls is always nearly 3.35 Å, as for graphite. They are grown in a carbon-arc chamber, similar to the one used for making large quantities of C_{60}. The second type is single-walled tubes [11]. Each tube has only a single wall, and a radius $\sim 3 - 10$ Å. They are grown with transition metal catalytic particles. A TEM picture is shown in Fig. 4.2. The third sample type will be called *ropes* [48]. A rope consists of a triangular array of single-walled tubes with radii ~ 7.8 Å, presumably held together by Van der Waals forces. They are very long, and bend continuously along their length. A TEM image is shown in Fig. 4.3. These tubes are made with a laser vaporization technique using catalysts.

In order to simplify the theoretical analysis of nanotube properties, we begin by describing a classification scheme for tube geometries [13]. We focus on single-walled tubes, for multi-walled tubes and ropes are just collections of single-walled tubes. A single-walled carbon nanotube is uniquely defined by its circumference vector, $\vec{\mathbf{c}} = n\vec{\mathbf{a_1}} + m\vec{\mathbf{a_2}}$, where $\vec{\mathbf{a_1}}$ and $\vec{\mathbf{a_2}}$ are lattice translation vectors of a graphite sheet, chosen to be 60^o apart. The atom at position (0,0) is made equivalent to the atom at position (n, m) by rolling. The length of $\vec{\mathbf{c}}$, $|\vec{\mathbf{c}}| = a\sqrt{n^2 + m^2 + nm}$, becomes the circumference of the resulting cylinder. An example is shown in Figs. 4.4, and 4.5. Note that if $n \neq m$,

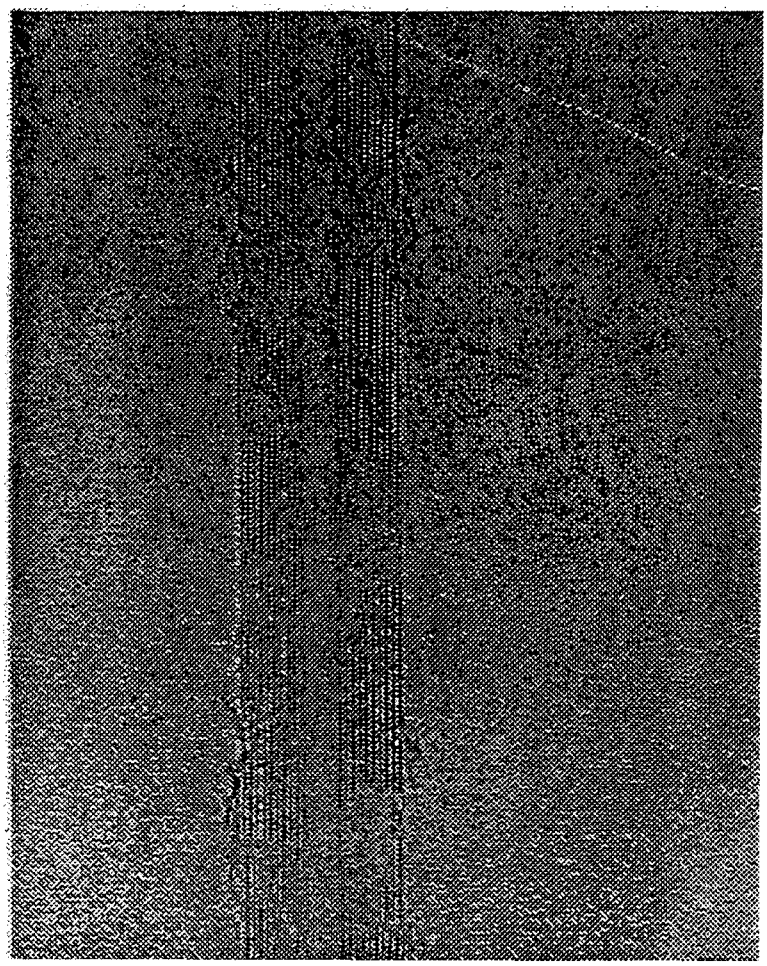

Figure 4.1: TEM image of a 10-walled carbon nanotube taken by N.G. Chopra. The distance between adjacent walls is nearly 3.35 Å.

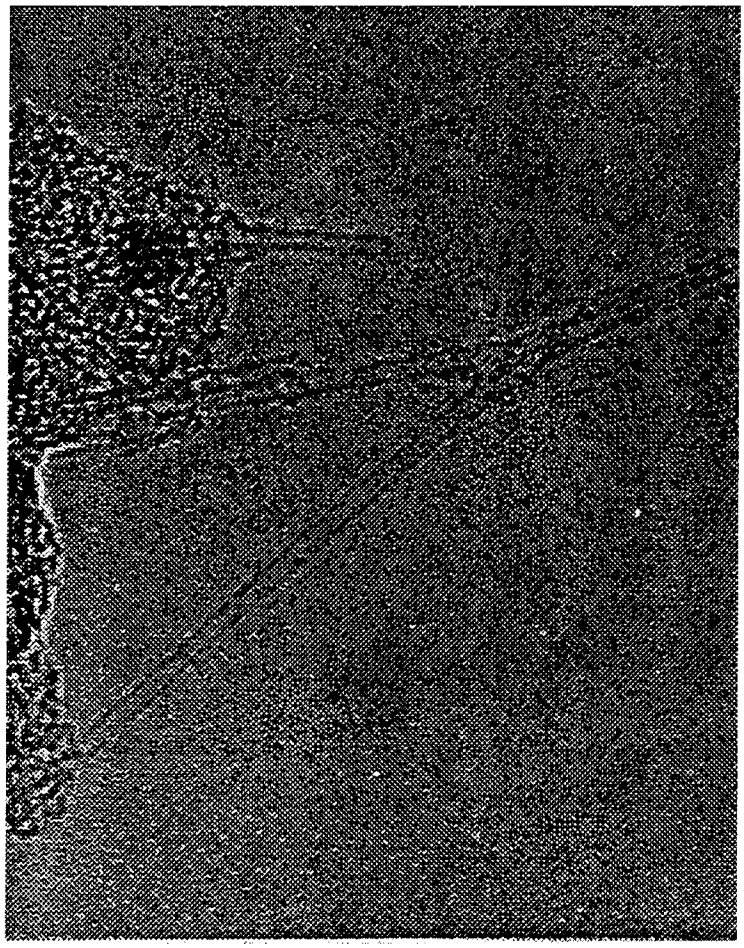

Figure 4.2: TEM image of single-walled carbon nanotubes taken by N.G. Chopra. Unlike the single-walled tubes of Ref. [11], these tubes were extracted from ropes of single-walled tubes discussed below.

Figure 4.3: TEM image of ropes, or arrays of single-walled tubes taken by N.G. Chopra. The costituent single-walled tubes have radii ~ 7.8 Å.

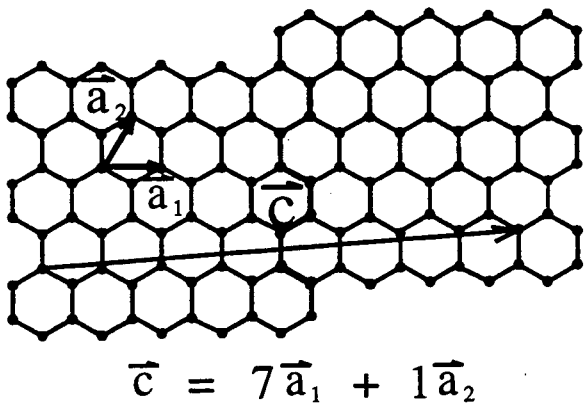

Figure 4.4: Circumference vector of the (7,1) tube mapped onto a graphite sheet.

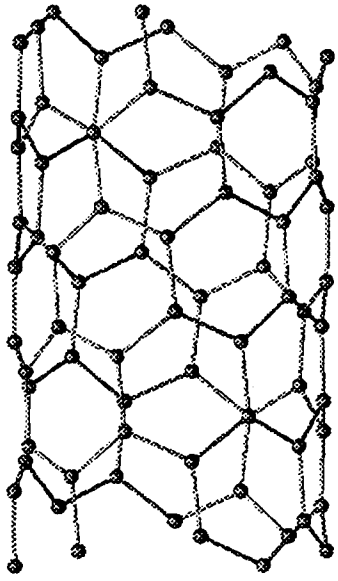

Figure 4.5: Atomic structure of the (7,1) tube.

and n and m are both different from zero, then the hexagonal carbon rings spiral up the tube in a helical fashion. This is refered to as chirality, or helicity. If one of n or m = 0, or $n = m$, then the tube is said to be non-chiral.

Since carbon nanotubes consist of rolled-up graphite sheets, it is natural to derive the electronic structure of single-walled nanotubes from the band structure of single-sheet graphite [13, 14, 15]. In chapter 1, we mentioned that the Fermi level states of an undoped graphite sheet have k-vectors that lie on the corners of the hexagonal BZ (the points labeled by K in Fig. 1.6). To determine if the tube with circumference vector $\vec{c} = (n, m)$ (hereafter called the "(n, m) tube") is a metal, we must see if the circumferential periodic boundary conditions *include* these k-points. The sheet wavevector $\vec{k}$ will be included if it satisfies the condition of single-valuedness of the tube wavefunction:

$$\vec{c} \cdot \vec{k} = 2\pi J, J = 0, \pm 1, \pm 2, ... \tag{4.1}$$

Plugging in the K-point:

$$\vec{c} \cdot (\frac{1}{3}\vec{b_1} - \frac{1}{3}\vec{b_2}) = (n\vec{a_1} + m\vec{a_2}) \cdot (\frac{1}{3}\vec{b_1} - \frac{1}{3}\vec{b_2}) = \frac{2\pi}{3}n - \frac{2\pi}{3}m = 2\pi J, \tag{4.2}$$

or,

$$n - m = 3J, J = 0, \pm 1, \pm 2, ... \tag{4.3}$$

The (n, m) carbon nanotube is metallic if $n - m$ is a multiple of 3, and is semiconducting otherwise. An example of this is shown in Fig. 4.6, where the allowed k-vectors for (7,1), and (8,0) tubes are overlayed on the graphite sheet BZ. Each line represents a different value of J in the equations above. Lines intersect the corners for the (7,1) tube, but do not for (8,0). The gap of the (8,0) tube can be estimated by looking at the allowed k-points which are closest to the corners. The gap is approximately equal to the energy difference between graphite sheet π and π^* (antibonding π) states at these k-points. The closer the allowed lines come to the corners, the smaller the gap.

Of course, these arguments only hold for the large radius case. If the tube radius is small, then the underlying graphitic surface is highly curved, and it is no longer correct

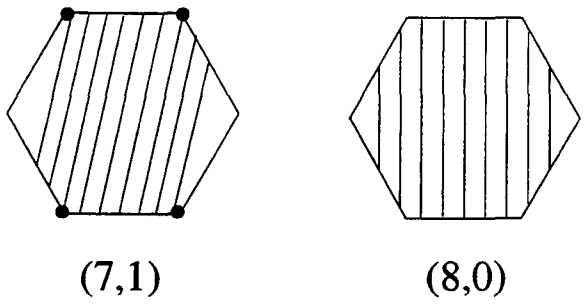

Figure 4.6: Allowed k-vectors of the (7,1) and (8,0) tubes mapped onto the graphite sheet BZ. Some lines intersect the corners for the (7,1) tube, while they do not for (8,0).

to think of a tube as a sheet with periodic boundary conditions. We will explore some of the consequenses of this for tubes with radii < 3 Å in the next chapter. For now, we note that curvature induces $\sigma - \pi$ hybridization, or admixture of sp^3 into what is predominantly sp^2. The lowest order effect of $\sigma - \pi$ hybridization on the above rules for metallicity is as follows [14]: (n, m) tubes with $n - m = 3J, J = \pm 1, \pm 2, ...$ are *very small − gap semicondutors*; only tubes with $n = m$ are metallic. All others are semiconductors, as stated above. For example, the (7,1) tube is predicted to have a band-gap of ~ 0.08 eV when $\sigma - \pi$ hybridization is taken into account [49].

The result of all this is that (n, m) carbon nanotubes with radii > 3 Å come in three varieties: large-gap, small-gap, and no gap. The large-gap tubes are those with $n - m \neq$ a multiple of 3. The small-gap tubes have $n - m =$ a nonzero multiple of three. Metallic tubes are of the (n, n) variety, also known as arm-chair tubes. As the tube radius, R, increases, large-gap and small-gap varieties both tend towards the zero-gap graphite sheet. We can see this explicitly by looking at the periodic boundary condition argument. As R increases, $|\vec{c}|$ increases, so the number of allowed J-values increases (see Eq. 4.1). Thus, the density of allowed lines increases and the smallest distance between a line and the K-point decreases. Since the π-bands disperse linearly away from K

(see Fig. 1.4), the tube band gap should be inversely proportional to R. Tight-binding calculations of Mintmire et al. [50] predict band-gaps that scale roughly as A/R, where $A = 4$ eVÅ for the large-gap tubes, and 0.1 eVÅ for the small-gap tubes. Similar reasoning shows that for metallic tubes, $N(E_F) \propto 1/R$. It should be noted that the same circumferential periodic boundary condition arguments can be applied to other elementary excitations. In particular, phonon modes of a graphite sheet may be used to predict the phonon band structure of carbon nanotubes [51].

The following seven chapters deal with physical properties which are a direct consequence of the novel geometric and electronic structures of carbon nanotubes. First, we consider the effects of $\sigma - \pi$ hybridization on the band structure of very small radius tubes. Then we propose heterostructures made from nanotubes which could be used as electrical devices. The radius dependence of the low temperature behavior of the heat capacity of carbon nanotubes is studied, and we calculate the radius and band-gap dependence of the static polarizability tensor for single-walled tubes. This is followed by two chapters on carbon nanotube transport properties. The last chapter concerns the energetics of a flattened, or collapsed state of nanotubes.

Chapter 5

Electronic structure of small-radius nanotubes

In the last chapter, we focused on classifying carbon nanotubes as metals or semiconductors. Although early work [13, 14, 15] has noted that hybridization of the graphitic σ,π,$\pi^\star$ and $\sigma^\star$ states should occur because of the curvature of the tubes, the importance of these effects was not fully appreciated. The tube states near the Fermi level were described as chiefly π and $\pi^\star$ states. Recently [11], nanotubes with very small radii were experimentally produced, with diameters as small as 7 $\AA$. In this chapter, we show that sufficiently strong hybridization occurs in such tubes which dramatically changes the band structure proposed in previous works.

We have carried out both *ab initio* pseudopotential local density functional (LDA) calculations and Slater-Koster [52] tight-binding (TB) calculations. We study the tubes $(n,0)$, with n ranging from 6 to 9. As illustrated in Fig. 5.1a, tube $(n,0)$ corresponds to wrapping a section of a graphitic sheet in the indicated orientation with n hexagons around the tube circumference. The diameter of these tubes ranges from 4.78 $\AA$ for (6,0) to 7.20 $\AA$ for (9,0). The LDA electronic structure calculations were performed using a planewave basis set. We generated first a semilocal pseudopotential following the scheme of Troullier and Martins [53] and made it fully nonlocal according to the Kleinman and Bylander procedure [54]. The energy cut-off for the electronic wave-functions was set at E_{cut}= 49 Ry leading to an 0.05 eV convergence of the band energies. The very large number of planewaves needed for this type of calculation (ranging from 13,500 for (6,0) to 19,000 for (9,0)) required the use of an efficient iterative diagonalization scheme [21]. The LDA calculations were carried out in a supercell geometry with a hexagonal array of tubes, with the closest distance between atoms on different tubes being 5.5 $\AA$. This

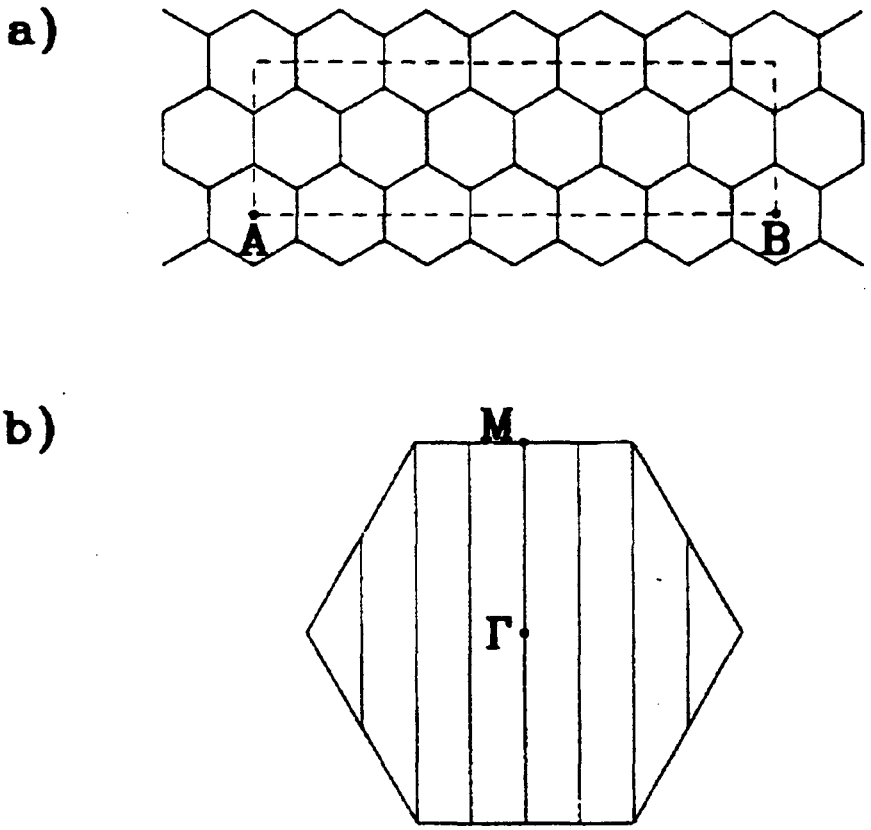

Figure 5.1: (a) Unit cell of the (6,0) tube mapped onto the graphite sheet. For the tube, point A is rolled onto point B. (b) Brillouin zone of the graphite sheet. The vertical lines mark the set of allowed k vectors for the tube

permitted the neglect of tube-tube interactions. For the TB calculations, we used the first and second nearest neighbor parameters proposed in Ref. [4] for graphite.

Along the axes of the tubes, the length of the unit cell was set by assuming that the tube was generated simply by rolling a graphite sheet segment. Using the Hellmann-Feynman theorem, we found that the stresses imposed on each supercell were negligible in the axis direction. The most important structural change was the tendency of the tube to reduce its radius from that given by the above rolling. This effect was nonetheless small, ranging from 1.6 % reduction for (6,0) to nearly zero for (9,0). We found similar results within a tight-binding total energy minimization scheme [55]. The effect of this relaxation on the electronic band structure was negligible. We also relaxed the internal coordinates of the atoms using Hellmann-Feynman forces. The forces were very small, and all the atoms remained equivalent within the unit cell.

Our results for the band gaps are given in Table 5.1, compared with those from previous TB work [14]. We find major differences between the results from LDA and the TB calculations. The most significant difference occurs for the tube (6,0) which has been previously predicted to be a small gap semiconductor [14]. We find in this work that, within LDA, tube (6,0) is a metal. In addition, we find that tubes (7,0) and (8,0) are semiconductors, consistent with previous calculations, but with a much smaller gap than those from TB works. This discrepancy is due to a singly degenerate state which is much lower in our LDA calculations than in the TB work. LDA is known to underestimate the value of the band gap of many materials, but the narrowing of the gap here is due primarily to curvature effects, as evidenced by the dependence on tube size.

In Fig. 5.2 we show the band structure and density of states (DOS) for the tube (6,0). The singly degenerate state mentioned above is labeled by (a). At Γ, this state is 0.83 eV below the doubly degenerate state that forms the top of the valence band in TB calculations. This band overlap makes the tube (6,0) a metal within LDA with a density

Table 5.1: Band gap (in eV) of selected tubes. All gaps given are direct and at the Γ-point. For the metallic case, the overlap of the bands is given as a negative gap.

tube	Tight Binding	Present calculations	
	Ref. [14]	TB	LDA
(6,0)	~ 0.2	0.05	metal (- 0.83)
(7,0)	~ 1	1.04	0.09
(8,0)	1.22	1.19	0.62
(9,0)	0.04	0.07	0.17

of states at the Fermi level equal to $D(E_F) = 0.07$ states/eV-atom. For this tube, we also performed an independent LDA calculation using a semilocal pseudopotential and another diagonalization scheme as described in Ref. [24]. The two LDA band structures were in excellent agreement. We also checked that this state is insensitive to the small structural relaxation effects described above.

As we shall show, state (a) occurs in all $(n, 0)$ tubes for symmetry reasons, but its energy at Γ varies with n. For the tubes (7,0) and (8,0), state (a) does not close the gap, but reduces significantly its value as compared to TB calculations. For these two tubes, the state (a) at Γ lies between the two doubly degenerate states that form the HOMO and LUMO states in TB calculations. This state reduces the TB gap by 1 eV for (7,0) and by 0.6 eV for (8,0). For the tube (9,0), the state (a) lies just above the TB LUMO state and therefore does not fall within the gap.

The discrepancy between TB and LDA calculations decreases as the radius of the tube increases. This is consistent with the notion that in large tubes with small curvatures, one obtains a good description of the nanotube band structure by "folding" the graphite sheet band structure. However, this idea implicitly relies on the assumption that states around the gap or Fermi level are essentially π or π^* derived. This is not true

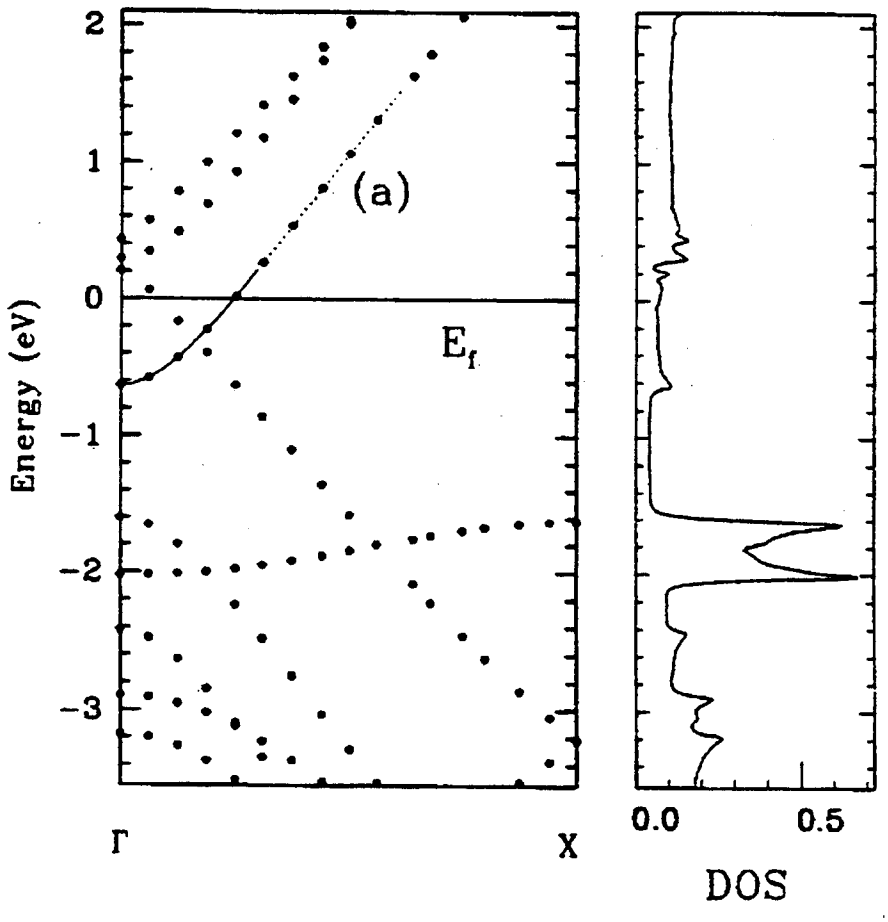

Figure 5.2: Band structure and density of states (states/eV-atom) for the tube (6,0). The energies are in eV and the zero is at the Fermi level. We trace the new band (a) around the center of the Brillouin zone as a guide to the eye.

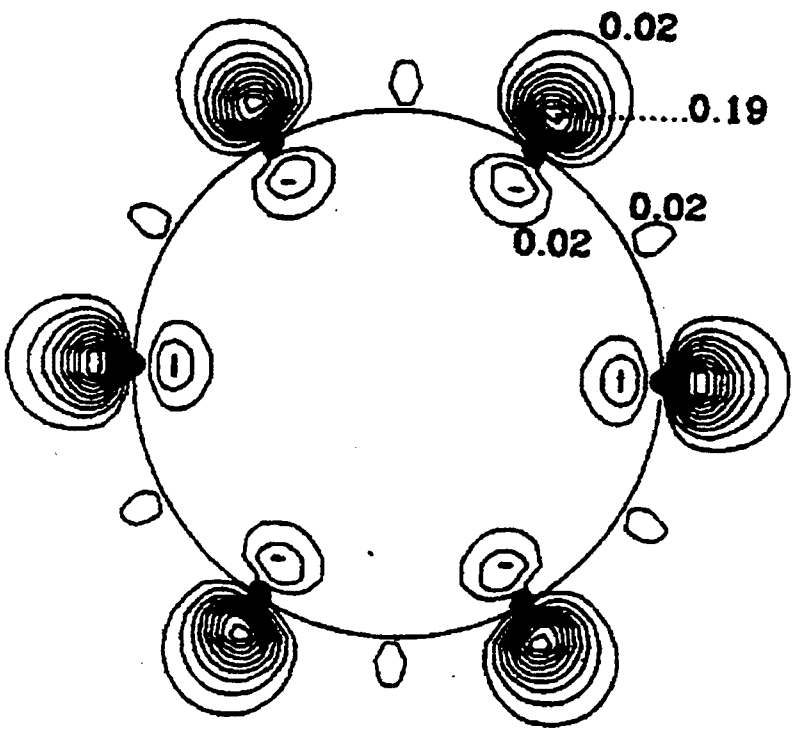

Figure 5.3: Contour plot of the charge density for state (a) at Γ for tube (6,0). The contours are in a plane perpendicular to the axis of the tube which contains six carbon atoms. The numbers quoted are in units of e/[a.u.]^3. The circle represents a cross section of the cylinder on which the atoms lie.

for small tubes where the curvature is so strong that large hybridization effects occur. We show in Fig. 5.3 the charge density distribution for the state (a) at Γ for the tube (6,0). One can see that most of the wave-function is localized outside the tube. If this state is mostly π or π^* derived, it should have equal weight inside and outside the tube. Detailed analysis of the σ^*-π^* hybridization in $(n,0)$ tubes also indicates that this state should be mostly outside of the tubes for k-vectors near the tube's zone center. We show below that it is crucial to accurately describe the σ^* states and their interaction with the π^* complex before one is able to reproduce within TB the behavior of the state (a)

in our LDA calculation.

To study the effects of hybridization on the state (a) of tube (6,0), we begin with a planar sheet of graphite with the unit cell described in Fig. 5.1a. Because state (a) is singly degenerate, in the "band folding" language, it must be derived from the Γ-M line of the graphite sheet Brillouin zone (BZ), and must occur in all $(n, 0)$ tubes. As a result of the boundary conditions of the tube, M is folded onto Γ. We plot in Fig. 5.4a the corresponding TB bands along the Γ-X direction of the tube (see Ref. [14]). From the symmetry of the tube, singly degenerate states only mix with each other and not with states of higher degeneracy, so only these need be considered in the analysis of the behavior of state (a). The dashed lines are the singly degenerate bands coming from the folding of the $\pi^\star$ and $\sigma^\star$ graphite bands along the Γ-M line of the hexagonal graphite BZ (Fig. 5.1b) onto the Γ-X line of the tube BZ. Next we bend this graphite sheet along the AB direction while imposing the proper periodic boundary conditions in order to mimic a continuous transformation of the graphite sheet onto the (6,0) tube. This procedure distinguishes the zone folding from the curvature.

Fig. 5.4 illustrates the evolution of our TB band structure under this transformation for two of these "intermediate" structures. Their radii of curvature are between $R = \infty$ of planar graphite (Fig. 5.4a) and R =2.39 $\AA$ of tube (6,0) (Fig. 5.4d). For a curved sheet of graphite, the $\pi^\star$ and $\sigma^\star$ states mix and repel each other, resulting in a lowering in energy of the (originally) pure $\pi^\star$ states. It is the lower hybridized $\pi^\star$ band which gives rise to the singly degenerate state (a) near E_F in the LDA calculation. Therefore, within the TB Hamiltonian of Ref. [4], this state does exist, but it is not low enough in energy to make the tube metallic as found in the LDA calculation. We note also that, with a localized basis set limited to $2s$ and $2p$ orbitals, TB calculations are unable to describe large charge transfer asymmetrically away from the atoms. However, in our LDA calculations, we find the total potential to be locally symmetric inside and outside the tube so that the localization of the state (a) outside the tube must be mainly due

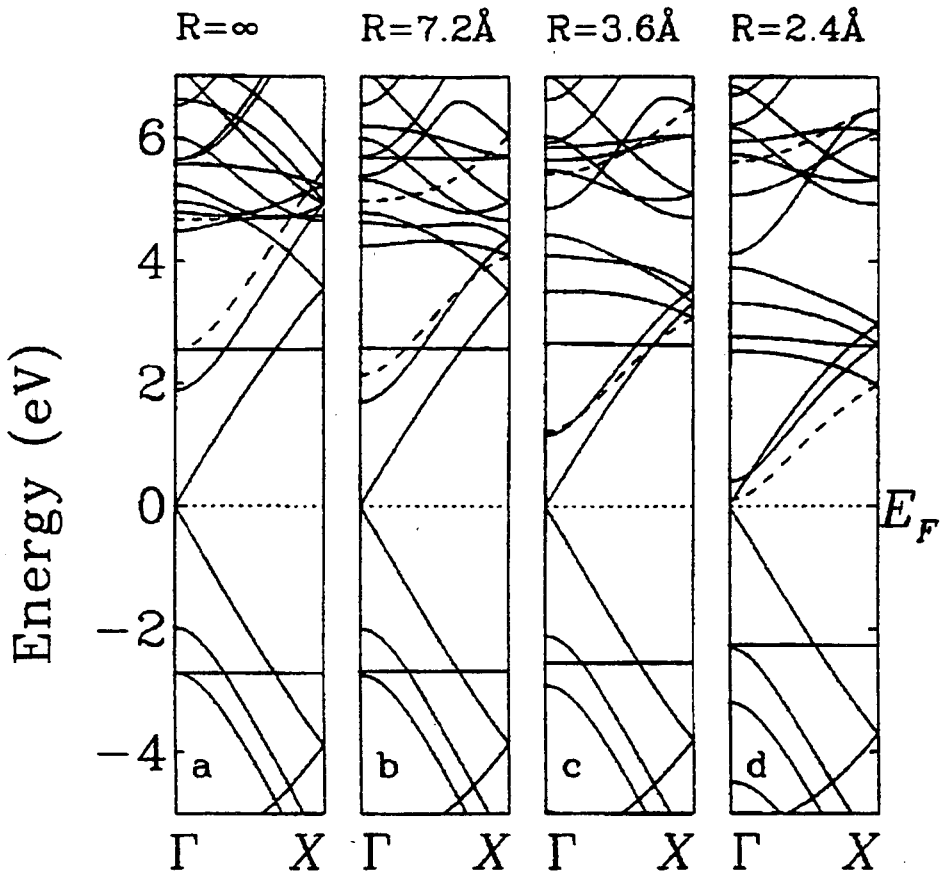

Figure 5.4: Evolution of the graphite TB bands near the Fermi level for the (6,0) geometry under increasing curvature. Energies are in eV and the zero is set at the Fermi level. The dashed curves mix strongly with each other due to curvature. In an LDA calculation, the lower one would span the gap. The radii of curvature are indicated.

to hybridization and not electrostatic effects. Similar studies have been made for tubes (7,0), (8,0), and (9,0), yielding similar results.

Some workers [56, 57] have recently suggested that very small radius tubes may not be energetically stable. It is argued that at some critical radius the elastic strain energy per atom stored in the rolled sheet would be larger than the dangling bond energy per atom for the flat graphitic strip obtained by "cutting" the tube along its cylindrical axis. In order to address this question for the tubes of our study, we carried out LDA total energy calculations for our smallest tube (6,0) with radius 2.39 $\AA$, and its corresponding strip and found that the tube is energetically more stable than the strip. This implies that the critical radius below which tube energy exceeds strip energy for $(n, 0)$ tubes is less than the (6,0) radius. The result is in agreement with the conclusion of a previous classical force-field calculation [56] which predicts the critical radius to be $\sim$ 2 $\AA$, in contradiction with the semi-empirical calculation of Ref. [57] which predicts $\sim$ 3.85 $\AA$. However, we stress that as long as the tube and strip energies are comparable, kinetic effects will still dominate the growth process. Thus, total energy comparisons may not be relevant to the question of tube formation.

In conclusion, large π^*-σ^* hybridization can occur in small nanotubes which drastically changes the electronic band structure from that obtained by simply "folding" the graphite sheet band structure. These effects are demonstrated in our study of tubes (6,0) to (9,0), some of which are comparable in size to the smallest tube experimentally observed thus far. Our results show that, for this class of tubes, hybridization changes the energy and character of the lowest lying conduction band states with important consequences to the metallicity and transport properties of the tubes. An implication of this result is that hybridization could also play an important role in doped small nanotubes with metallic dopants either inside or on the tubes.

Chapter 6

Nanotube heterojunctions

In the last two chapters, we have seen that helicity has a profound effect on the electronic structure of carbon nanotubes[13, 14, 15]. All non-chiral, armchair (n, n) tubes are metals. Excepting those of very small-radius[58], all moderate-radius (n, m) tubes with $n - m$ a nonzero multiple of three are small gap semiconductors or semimetals[13]. The remaining tubes are semiconductors with band gaps roughly proportional to the reciprocal of the tube radius[50].

Instead of comparing the electronic structures of tubes with different helicities, we consider changes in helicity *within a single tube.* The chirality of a tube can be changed by introducting topological defects into the hexagonal bond network[59]. The defects must induce zero net curvature to prevent the tube from flaring or closing. Minimal local curvature is desirable to minimize the defect energy. The smallest topological defect with minimal local curvature and zero net curvature is a pentagon-heptagon pair. A pentagon-heptagon defect pair with symmetry axis nonparallel to the tube axis changes the chirality of a nanotube by one unit from (n, m) to $(n \pm 1, m \mp 1)$. Fig. 6.1 shows an $(8, 0)$ tube joined to a $(7, 1)$ tube. The highlighted atoms comprise the defect. We denote this structure by $(8, 0)/(7, 1)$, in analogy with interfaces of bulk materials. Within tight binding, far from the interface the $(7, 1)$ half-tube is a semimetal and the $(8, 0)$ half-tube is a moderate gap semiconductor. The full system forms a quasi-1D semiconductor/metal junction. Unlike most semiconductor/metal junctions[60], the $(8, 0)/(7, 1)$ junction is composed of a single element.

We use a tight-binding model with one π-orbital per atom along with the Surface Green Function Matching method (SGFM)[61] to calculate the local density of states

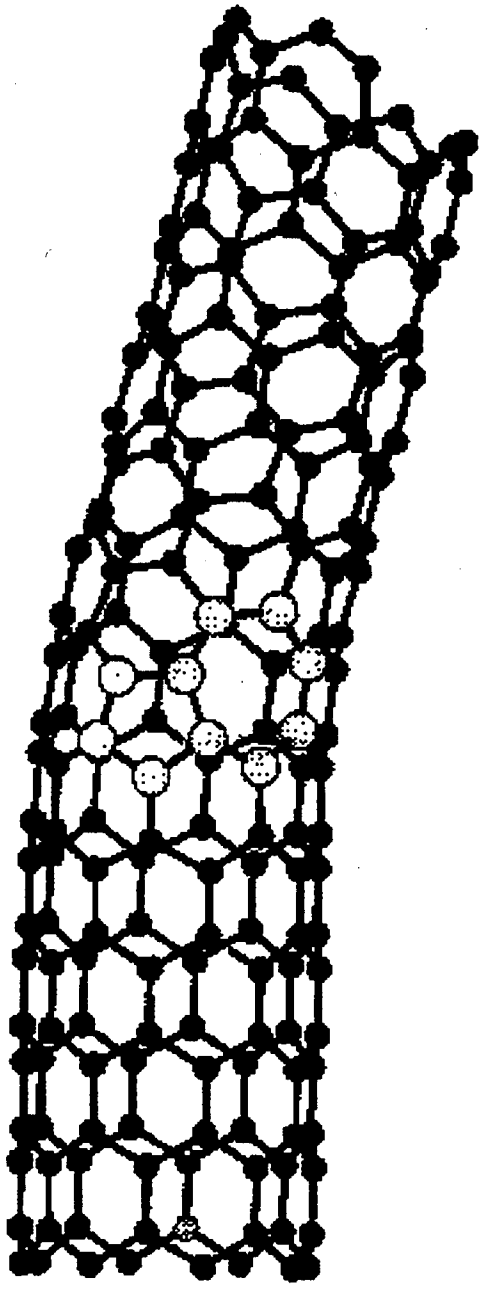

Figure 6.1: Atomic structure of an (8,0)/(7,1) tube. The large light-grey balls denote the atoms forming the heptagon-pentagon pair.

(LDOS) in different regions of two archetypal $(n_1, m_1)/(n_2, m_2)$ systems. In particular, we examine the $(8,0)/(7,1)$ semiconductor/metal junction and the $(8,0)/(5,3)$ semiconductor/semiconductor junction formed with three heptagon-pentagon pairs. In both cases the unit cells of the perfect tubes match at the interface without the addition of extra atoms.

The unit cells of the perfect $(7,1)$ and $(8,0)$ half-tubes may be matched uniquely with a single pentagon-heptagon pair. The interface between the unit cells of the $(8,0)$ and $(5,3)$ half-tubes contains three heptagons, three pentagons, and two hexagons. Two different matching orientations are possible: one with the two hexagons adjacent, the other without. We choose to study the configuration in which the hexagons are separated from each other. The sequence of n-fold rings around the circumference is then 6-7-5-6-7-5-7-5.

In the π-electron approximation of tight binding[62] the $(8,0)$ tube has a 1.2 eV gap[13] and the $(7,1)$ tube is a semimetal. Within tight binding, these tubes form an archetypal semiconductor/metal junction. We note that curvature-induced $\sigma - \pi$ hybridization modifies these band gaps. In particular, within the local density approximation (LDA) the gap of the $(8,0)$ tube is 0.62 eV[58] and the $(7,1)$ tube is a small-gap semiconductor[50]. For the purposes of examining the generic, qualitative features of carbon nanotube heterojunctions, we restrict ourselves to the π-electron tight binding treatment in which $(8,0)/(7,1)$ is a semiconductor/metal junction. Within the same picture, the band gap of the perfect $(5,3)$ tube is 1.4 eV[63], 0.2 eV larger than that of the $(8,0)$ tube. The $(8,0)/(5,3)$ junction therefore provides a prototypical example of a semiconductor heterojunction.

We examine the local density of states in various regions on both sides of the $(8,0)/(7,1)$ and $(8,0)/(5,3)$ junctions. Our π-electron tight-binding Hamiltonian is of

the form

$$H = -V_{pp\pi} \sum_{\langle ij \rangle} a_i{}^{+} a_j + c.c. \tag{6.1}$$

where i and j are restricted to nearest neighbors, and $V_{pp\pi} = 2.66$ eV[64]. The on-site energy is set equal to zero. Within this theory, graphite sheets and defect-free nanotubes have complete electron-hole symmetry with their Fermi levels at zero. All nearest-neighbor hoppings are taken to be equal, independent of the length, location and orientation of the bonds on the matched tubes. Deviations in bond lengths due to reconstruction near the interface are neglected. Hence, we study the changes in local electronic structure solely due to changes in the *connectivity* of the lattice.

To determine the LDOS of two joined semi-infinite tubes, we calculate the Green function using the SGFM method. Details about this formalism can be found elsewhere [61]. The SGFM technique allows us to calculate the Green function of a composite system formed by joining two semi-infinite media from the Green functions of the two infinite constituent systems. Thus, knowing the Green functions of the pure (n_1, m_1) and (n_2, m_2) tubes, we can easily construct the Green function of the system formed by joining two semi-infinite tubes, $(n_1, m_1)/(n_2, m_2)$. Knowledge of the Green function allows us to extract the local density of states at any site on the matched structure.

The results for the $(8,0)/(7,1)$ matched tube are plotted in Figs. 6.2 and 6.3. Fig. 6.2 shows the unit-cell averaged LDOS for three unit cells of the (8,0) half of the matched tube, and for comparison, the DOS of a perfect (8,0) tube. The unit cells are numbered beginning from the junction, so cell 1 of (8,0) is at the interface, in contact with cell 1 of (7,1). We average the LDOS over each cell because quantum interference effects distort the LDOS on individual atomic sites. The unit cell of the (8,0) tube is a circumferential ring of hexagons containing 32 atoms. As the unit cell of the (7,1) tube has 76 atoms, we choose in Fig. 6.3 to plot the LDOS for on the (7,1) side averaged over 32-atom rings. In this way the local densities of states on either side of the system can be directly

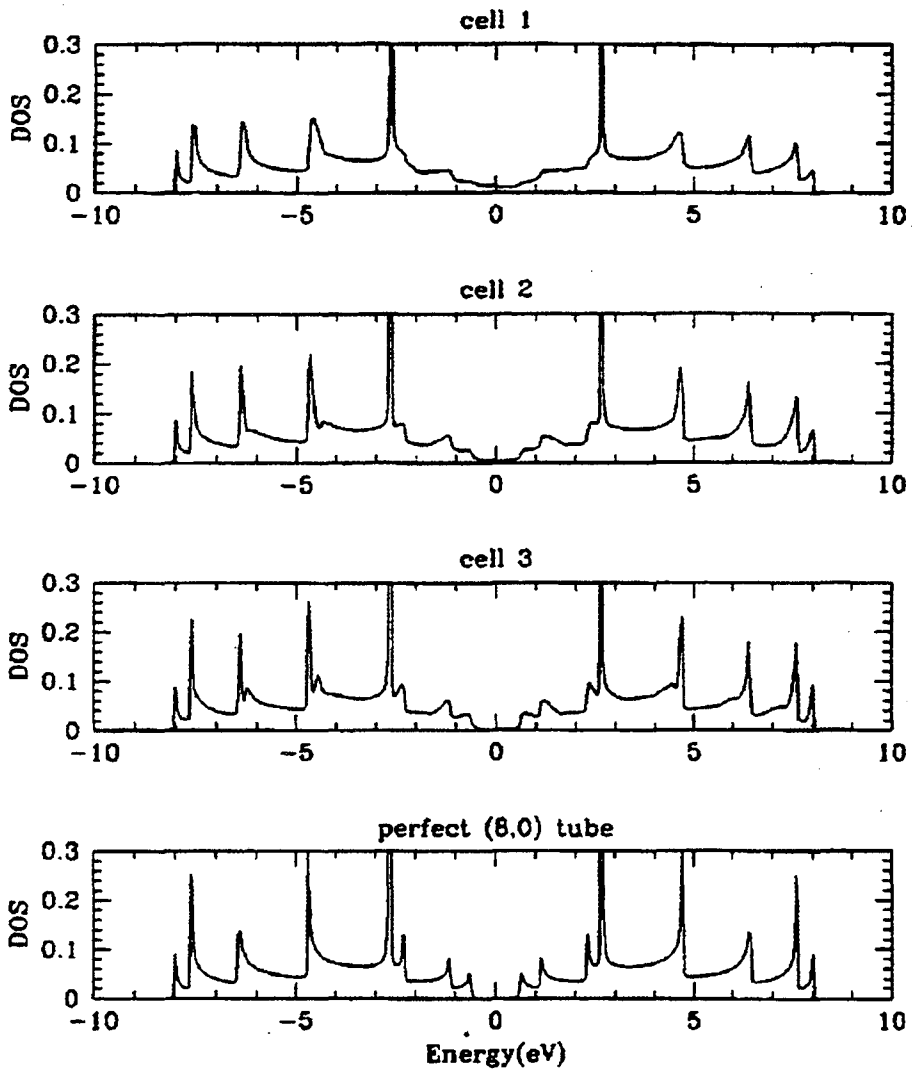

Figure 6.2: Results for the (8,0)/(7,1) metal/semiconductor tube. From top to bottom, LDOS at cells 1, 2 and 3 of the (8,0) side, and DOS for a perfect semiconducting (8,0) tube.

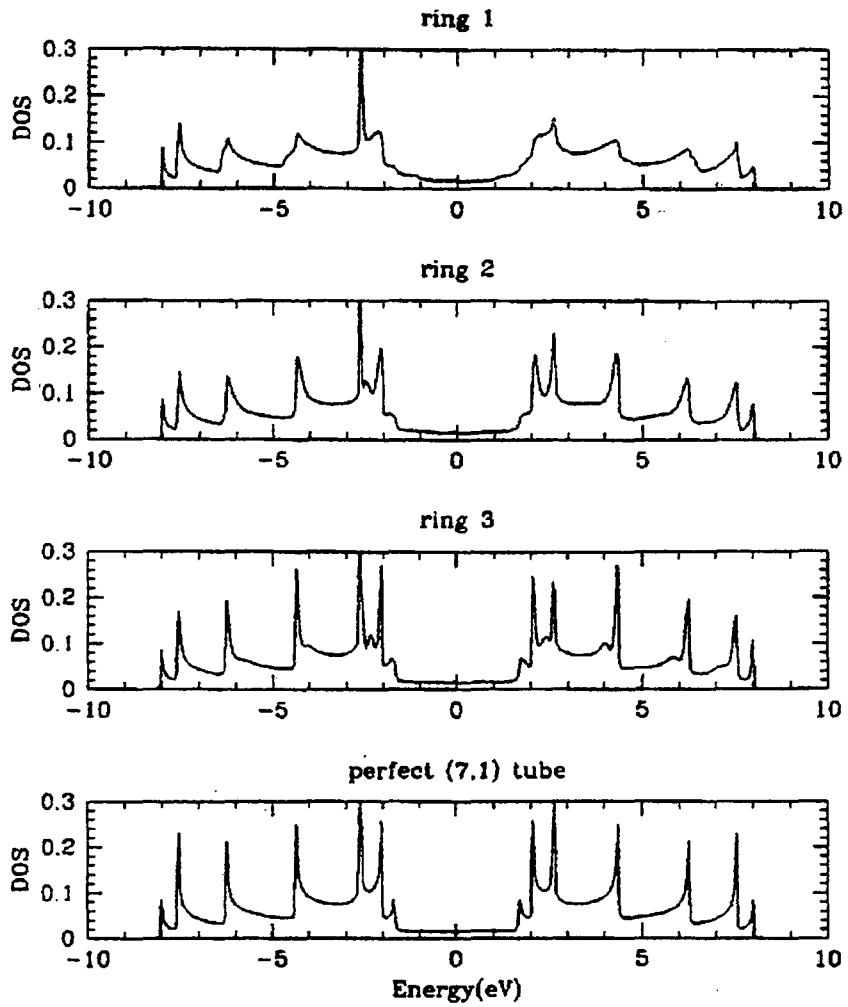

Figure 6.3: Results for the (8,0)/(7,1) metal/semiconductor tube. From top to bottom, LDOS at rings 1, 2 and 3 of the (7,1) side, and DOS for a perfect metallic (7,1) tube.

compared as a function of distance from the interface.

In Fig. 6.2 we see that the LDOS on the (8,0) semiconducting side of the junction is most distorted in cell 1, the region nearest the interface. For all the cells, the difference from the perfect-tube DOS is biggest for energies near the gap. In particular, cell 1 shows allowed states in the energy range of the gap of the infinite (8,0) tube. These metal-induced gap states[65] are characteristic of a metal-semiconductor junction. These states swiftly disappear as we move into the semiconductor, as shown in the plots for cells 2 and 3. Moving away from the interface, the perfect-tube DOS features are recovered: in cell 3, all the van Hove singularities of the infinite tube can be clearly identified.

Unlike the semiconductor side of the system, the LDOS around the Fermi energy (0 eV) in the (7,1) half-tube remains largely unchanged. In ring 1, most of the van Hove singularities present in the perfect (7,1) tube DOS are smeared out, with the exception of those at the highest and lowest energies. As expected, the features of the infinite (7,1) tube are gradually recovered when moving away from the defect region. All the features of the perfect (7,1) system are identifiable in ring 3.

The results for $(8,0)/(5,3)$ semiconductor/semiconductor heterojunction are plotted in Figs. 6.4 and 6.5. As for the previous case, we plot the LDOS at the (5,3) side averaged over 32-atom closed rings, instead of unit cells. Two defect states appear in the gap near the interface. The geometric distortions due to the three pentagon-heptagon pairs in the matching region create states in the gap in a manner similar to that seen in bulk semiconductor interfaces. As we have not changed the bond distances at the matching region, we attribute the appearance of these states to the changes in the lattice connectivity, that is, to the alteration of the network topology. We expect these interface states to pin the Fermi energy of the system[66].

The interface states have maximal local density of states in cell 1 of the (8,0) tube, the narrow-gap semiconductor of the junction. Their amplitudes are appreciable in 5 consecutive 32-atom rings, a 12 Å length along the tube axis. The amplitudes decay

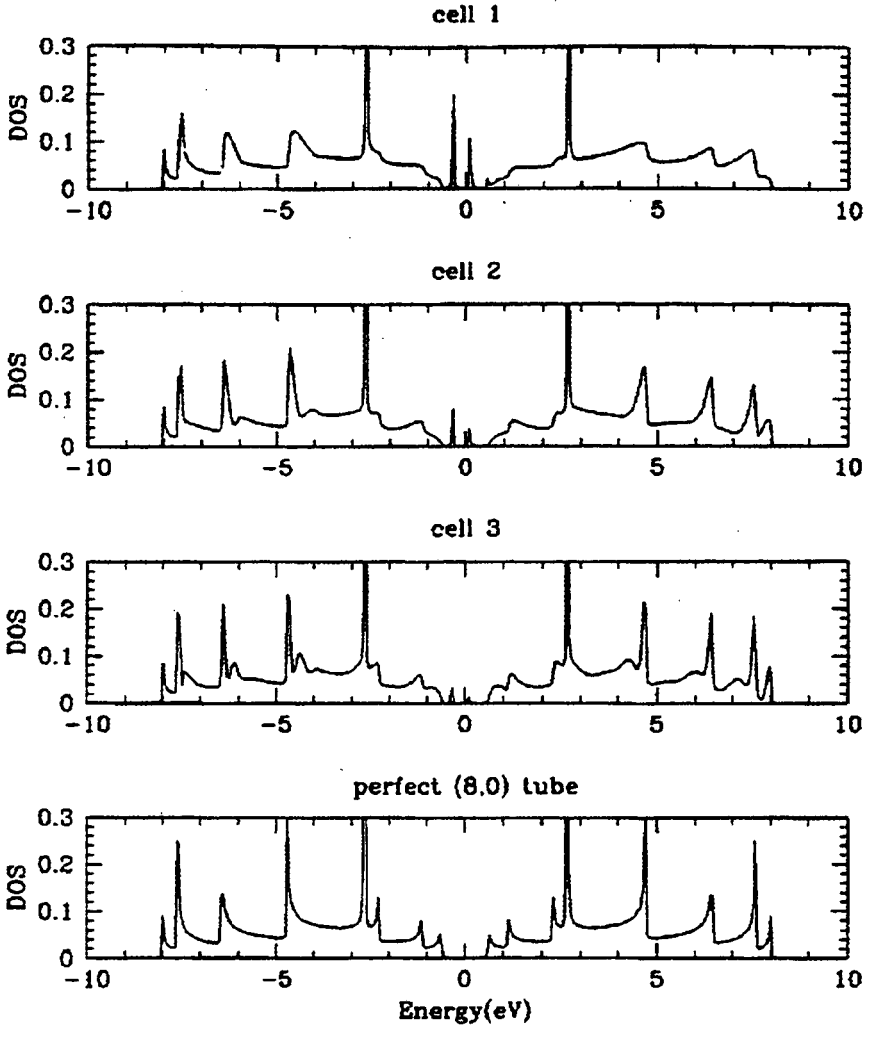

Figure 6.4: Results for the (8,0)/(5,3) semiconductor/semiconductor tube. From top to bottom, LDOS at cells 1, 2 and 3 of the (8,0) side, and DOS for a perfect semiconducting (8,0) tube.

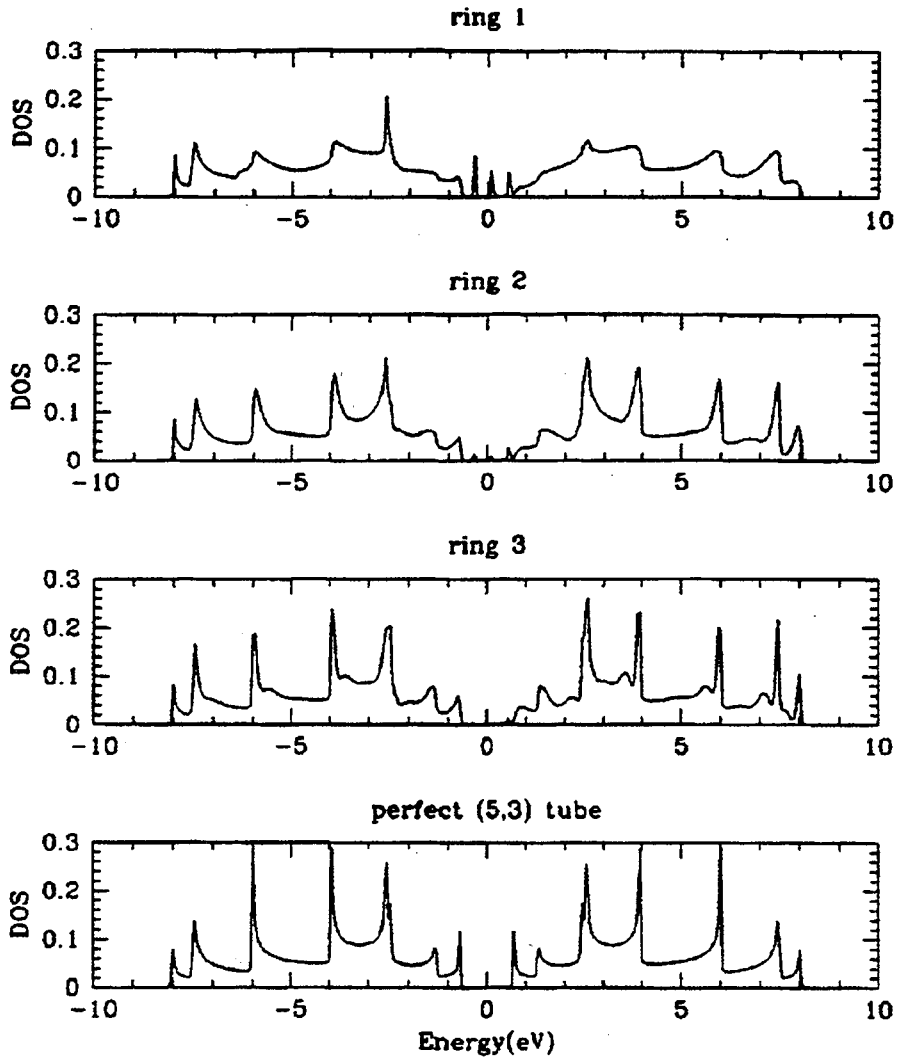

Figure 6.5: Results for the (8,0)/(5,3) semiconductor/semiconductor tube. From top to bottom, LDOS at rings 1, 2 and 3 of the (5,3) side, and DOS for a perfect semiconducting (5,3) tube.

faster in the (5,3) side of the system. This behavior is to be expected, for (5,3) is the wide-gap semiconductor of the junction. As already seen in the previous system, the LDOS in the interface region is the most distorted; the pure (5,3) and (8,0) features appear when moving far from the defect region.

Chirality-changing pentagon-heptagon defects provide a wide range of device possibilities for doped and undoped carbon nanotubes. By arranging these defects along the length of a carbon nanotube one could modulate the electronic structure and generate a variety of carbon-based quasi-1D quantum wells and superlattices with band offsets of $\sim$0.1 eV. Assuming a suitable third terminal could be introduced adjacent to a semiconducting barrier within a metallic nanotube, one can easily envision a gated conductive channel. The Fermi level of a metallic pure carbon nanotube lies within the gap of a similar semiconducting tube. As such, either n-type or p-type doping of the semiconducting side of a metal/semiconductor interface should yield a device similar to a Schottky barrier.

In summary, we have proposed a new type of metal/semiconductor or semiconductor/semiconductor junction, made of a single element, and based solely on the introduction of topological defects in the hexagonal graphite network. We have calculated the LDOS within the tight-binding approximation for two archetypical systems, showing the appearance of metal-induced gap states in a metal/semiconductor tube, and interface states in a semiconductor/semiconductor system. If produced, these could be the building blocks of nanoscale semiconductor devices.

Chapter 7

Heat capacity

It has been shown that tubes with radii $R > 3\mathring{A}$ have excitation spectra which closely resemble those of a graphite sheet with the proper periodic boundary conditions imposed. This has the interesting consequence that nanotube electronic band structures can have band gaps of anywhere between 0 and ~ 1 eV, depending on tube radius and helicity. The phonon bands are also radius and helicity dependent, but the low frequency acoustic modes always have $\omega \longrightarrow 0$ as $k \longrightarrow 0$ (for a tube of infinite length).

The heat capacity, $C_V \equiv \frac{\partial U}{\partial T}|_V$, is a quantity which directly reflects the details of the excitation spectrum. In particular, the low temperature behavior of C_V contains information regarding the type of excitations involved, and the dimensionality of the system. Because nanotubes are *quasi*-one dimensional (1D) systems consisting of rolled-up 2D sheets, they are expected to exhibit both 1D and 2D behavior. This is in contrast to the 2-3D behavior of bulk planar graphite.

In this chapter, we estimate the radius and helicity dependence of the low temperature behavior of C_V for carbon nanotubes, and deduce the range of R and T in which we expect it to be measurably different from that of graphite. We first consider single graphite sheets and single-walled tubes. Then we briefly discuss the more complicated cases of bulk graphite and multi-walled tubes. For small-radius tubes, it is shown that significant deviations from graphitic behavior should appear for presently accessible values of R and T.

For graphite and related systems, the heat capacity can be written as

$$C_V = C_{ph} + C_{el}, \tag{7.1}$$

where C_{ph} is the contribution due to phonons, and C_{el} is the contribution from electrons. If $T << \theta$ (Debye temperature), the phonon contribution for an isotropic D-dimensional system is

$$C_{ph} = \frac{D\pi^{\frac{D}{2}}\Omega\lambda {k_B}^{D+1}T^D}{(2\pi)^D\left(\frac{D}{2}\right)!\,\hbar^D v^D}\int_0^\infty dx \frac{x^{D+1}e^x}{(e^x-1)^2} \tag{7.2}$$

where Ω is the D-dimensional system volume, λ is the number of acoustic phonon polarizations, v is the sound velocity (assumed to be isotropic and equal for all polarizations), and k_B is Boltzmann's constant. For a 2D sheet of graphite with area A, this becomes

$$C_{ph} = \frac{3A{k_B}^3T^2}{2\pi\hbar^2v^2} \times (7.212), \qquad T << \theta \tag{7.3}$$

We will use $v \sim 10^6\ cm/s$ and $\theta \sim 1000\ K$. These values are determined by estimating an average of the sound velocity over the different polarization branches calculated by an *ab initio* frozen phonon technique[67].

The electronic contribution to the heat capacity for a system with density of states $N(E)$ is[68]

$$C_{el} = \Omega\int_0^\infty dE(E-E_F)\frac{df}{dT}N(E) \tag{7.4}$$

where f is the Fermi-Dirac function. Near E_F, the electronic states of an undoped graphite sheet are π-electron states with energies that disperse linearly away from a pointlike Fermi surface[69]. This gives rise to a density of states which goes to zero linearly as E approaches E_F,

$$N(E) = \frac{1}{\pi\hbar^2v_F^2}|E-E_F| \tag{7.5}$$

with the Fermi velocity, $v_F \sim 10^8\ cm/s$[70]. The fact that $N(E_F) = 0$ means that C_{el} will not be proportional to T at low temperature; instead, the relation is

$$C_{el} = \frac{2A{k_B}^3T^2}{\pi\hbar^2v_F^2}\int_0^\infty dx\frac{x^3e^x}{(e^x+1)^2} = \frac{2A{k_B}^3T^2}{\pi\hbar^2v_F^2} \times (5.409), \qquad T << T_F \tag{7.6}$$

Thus, we see that both the phonon and electron contributions to C scale as T^2 at low temperature. Examination of Eqs. 7.3 and 7.6 shows that

$$\frac{C_{ph}}{C_{el}} \sim \left(\frac{v_F}{v}\right)^2 \sim 10^4, \tag{7.7}$$

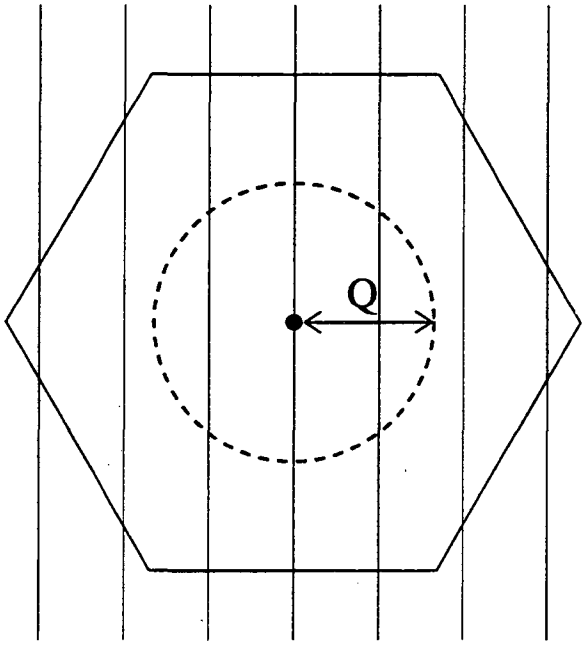

Figure 7.1: Lines of allowed **k**-vectors overlayed on the graphite sheet BZ. The solid dot indicates Γ ($\mathbf{k} = 0$). If $k_B T = \hbar v Q$, most of the phonon modes with **k**-vectors inside the dashed circle will be occupied, while most outside will be unoccupied.

so phonons dominate all the way down to $T = 0$.

Now consider a single-walled carbon nanotube of radius R. As long as R is large enough, it can be thought of as a graphite sheet with periodic boundary conditions imposed in the circumferential direction[13, 14, 15, 58]. This gives rise to a quantization of k_x (component of sheet wavevector in the circumference direction), while k_z (component in axis direction) is left continuous. The situation is depicted in Fig. 7.1, where lines of allowed **k** are overlayed on the graphite sheet first Brillouin Zone (BZ). It is easily shown that the perpendicular distance between adjacent lines is $\frac{1}{R}$.

The acoustic phonon bands of a graphite sheet are approximately isotropic in the plane, with frequencies that go to zero at the BZ center ($\mathbf{k} = 0$). Imagine that the sheet is at a temperature T and we define $Q(T)$ such that $k_B T = \hbar v Q(T)$. Then states with **k**-vectors lying within the circle of radius $Q(T)$ centered at $\mathbf{k} = 0$ will be mostly

occupied, while states with **k** outside will be mostly unoccupied (see Fig. 7.1). Suppose that $Q(T) >> \frac{1}{R}$. A calculation of C_{ph} for the tube requires us to sum over all partially occupied states originating from the allowed lines. Since many lines cross the circle, the result will resemble that of the 2D sheet given in Eq. 7.3. Now suppose that $Q(T) << \frac{1}{R}$. Only one line traverses the circle. This is the line that goes through $\mathbf{k} = 0$, so it contains the phonon bands for which $\omega \longrightarrow 0$. The calculation of C_{ph} is now that of a 1D system. The result is then

$$C_{ph} = \frac{3Lk_B{}^2T}{\pi\hbar v}\int_0^\infty dx \frac{x^2e^x}{(e^x-1)^2} = \frac{3Lk_B{}^2T}{\pi\hbar v} \times (3.292), \qquad T << \frac{\hbar v}{k_B R} \tag{7.8}$$

where L is the tube length.

The situation is represented graphically in Fig. 7.2. If R and T are small enough, $C_{ph} \propto T$. Otherwise, $C_{ph} \propto T^2$ (for $T << \theta$). There will be a crossover between T and T^2 behaviors when $k_BT \sim \frac{\hbar v}{R}$. From our estimated value of v, it follows that this crossover occurs at 300 K for a tube with $R = 2.5$ $\mathring{A}$, and at 7.5 K for a tube with $R = 100$ $\mathring{A}$. Since nanotubes with $R < 100$ $\mathring{A}$ are often seen experimentally and temperatures of several Kelvins are easily obtained, this regime is well within the reach of current experimental investigations. In particular, single-walled nanotubes synthesized using transition metal catalysts are invariably found to have diameters on the order of 10 $\mathring{A}$[11].

The dependence of C_{el} on R is complicated by the fact that the band gap, E_g, of carbon nanotubes depends sensitively on R and the tube helicity[13, 14, 15]. From Eq. 7.4, it can be shown that C_{el} for semiconducting tubes is proportional to $exp[-E_g/k_BT]$ at low temperature. As long as $k_BT << E_g$, C_{el} will be negligibly small. For metallic tubes,

$$C_{el} = \frac{\pi^2 L}{3} N(E_F) k_B{}^2 T, \qquad T << T_F. \tag{7.9}$$

We may use arguments analogous to those presented above for C_{ph} to show that a

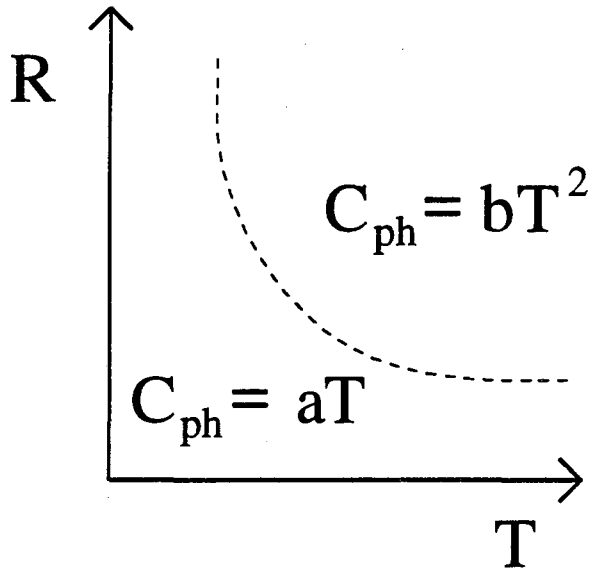

Figure 7.2: Schematic illustration of T-dependence of C_{ph} for carbon nanotubes. For small tube radius, R, and temperature, T, $C_{ph} \propto T$. Otherwise, $C_{ph} \propto T^2$, (for $T << \theta$). Dashed line is the curve $k_B T = \frac{\hbar v}{R}$.

metallic tube with one partially filled band will have

$$C_{el} = \frac{4\pi L {k_B}^2 T}{3\hbar v_F}, \qquad T << \frac{\hbar v_F}{k_B R} \tag{7.10}$$

Comparing this with Eq. 7.8, we see that

$$\frac{C_{ph}}{C_{el}} \sim \frac{v_F}{v} \sim 10^2. \tag{7.11}$$

Even for metallic tubes, phonons dominate all the way down to $T = 0$.

Because $C_{el} << C_{ph}$ for all tubes at sufficiently low temperature, we can approximate C_V by C_{ph} if R and T are in the range for which $C_{ph} \propto T$ (see Fig. 7.2). An isolated graphite sheet has $C_V \propto T^2$ at low temperature. Thus, we see that the temperature dependence of the heat capacity of single-walled tubes differs substantially from that of single graphite sheets as long as R and T are small enough. This 1D behavior is roughly independent of tube helicity since the acoustic phonons dominate C_V.

We now explore the differences between the heat capacities of noninteracting single-

sheets and bulk graphite. For bulk graphite, the weak coupling between sheets gives rise to a small but nonzero sound velocity along the c-axis. The dispersion relation for low-frequency acoustic phonon modes is anisotropic:

$$\omega^2 = v^2 \mathbf{k}_{sheet}{}^2 + v_c{}^2 k_c{}^2, \tag{7.12}$$

where v_c is the c-axis sound velocity. This has been determined by ultrasonic techniques[71]. The resulting ratio of velocities is $(\frac{v_c}{v}) \sim \frac{1}{100} - \frac{1}{10}$. We define a "c-axis Debye temperature" by

$$\theta_c \equiv \left(\frac{v_c}{v}\right)\theta, \tag{7.13}$$

where θ is the single-sheet Debye temperature considered above. A simple analysis involving the above dispersion relation yields

$$C_{ph} = \frac{3\Omega {k_B}^4 T^3}{2\pi^2 \hbar^3 v^2 v_c} \int_0^\infty dx \frac{x^4 e^x}{(e^x-1)^2} = \frac{3\Omega {k_B}^4 T^3}{2\pi^2 \hbar^3 v^2 v_c} \times (25.976), \qquad T << \theta_c \tag{7.14}$$

This is just the anisotropic generalization of Eq. 7.2 for $D = 3$. If, however, $T >> \theta_c$ but is still considerably less than θ, then the c-axis acoustic modes are completely occupied and we get $C_{ph} \propto \left(\frac{T}{v}\right)^2$, as for a 2D sheet[72]. There will be a significant range of temperature for which $C_{ph} \propto T^{2-3}$.

Unlike a single graphite sheet, bulk graphite has a nonzero $N(E_F)$ due to c-axis dispersion of the electronic states. This gives rise to an electronic contribution, $C_{el} \propto N(E_F)T$. Since $N(E_F)$ is very small for undoped graphite, $C_{el} < C_{ph}$ for all but the very lowest accesible temperatures. The result is that $C_V \propto T^{2-3}$ for typical samples in the temperature range $1\ K < T < 80\ K$ [73]. Thus, we see that the low temperature behavior of the heat capacity of single-walled carbon nanotubes ($C_V \propto T$ for sufficiently small R) is expected to be different from that of bulk graphite ($C_V \propto T^{2-3}$).

The heat capacity of multi-walled carbon nanotubes is a much more complicated issue. First, it has been predicted that electronic bands of a multi-walled tube near the Fermi level may be altered from the bands of the individual constituent tubes[74]. In

particular, small gaps can appear which result in $N(E_F) = 0$ even when the constituent tubes are metallic. This may change the small electronic contribution somewhat. More importantly, phonon spectra will now include modes which arise from inter-tube coupling, the analogue of c-axis modes in bulk graphite. A large radius multi-walled tube with N concentric walls can be approximated by an N-sheeted slice of graphite with periodic boundary conditions imposed in the c-direction[75]. From band-folding arguments similar to those given above, we find that $C_{ph} \propto T^2$ if $T << \frac{\pi\hbar v_c}{k_B N d}$, where $d \sim 3.35\mathring{A}$ is the graphite intersheet spacing. Otherwise, $C_{ph} \propto T^{2-3}$ as in bulk graphite. A multi-walled tube with small inner radius R will exhibit anything from 1D - 3D behavior, depending on the detailed values of R and N. However, sufficiently robust 1D behavior ($C_V \propto T$) should be seen if R is small and N is not too large.

In summary, we have considered the low temperature behavior of the heat capacity for four related systems: 1) a single graphite sheet, 2) single-walled carbon nanotubes, 3) bulk graphite, and 4) multi-walled carbon nanotubes. It is shown that a graphite sheet has $C_V \propto T^2$ at low temperature, while all single-walled carbon nanotubes have $C_V \propto T$. The temperature below which this should be observable decreases with increasing nanotube radius, but is accessible to current experimental investigations. Since bulk graphite has $C_V \propto T^{2-3}$, a sample of sufficiently small radius tubes should show a deviation from graphitic behavior. Of course, the deviation will only be appreciable if the mass fraction of small radius tubes is large enough to outway contributions from other graphite-like portions of the sample. Multi-walled tubes are expected to show a range of behavior intermediate between $C_V \propto T$ and $C_V \propto T^{2-3}$, depending in detail on the tube radii and the number of concentric walls.

Chapter 8

Static polarizability

In this chapter we examine the response of single-wall carbon nanotubes to a uniform external electric field $\mathbf{E}$. The main response of the electrons is the formation of an induced dipole moment $\mathbf{p}$. The quantity which relates the two is the polarizability tensor, α, defined by $\mathbf{p} = \alpha\mathbf{E}$. Since the discovery of fullerenes, numerous investigations have been undertaken to determine $\alpha(\omega)$ and $\alpha(\omega = 0)$ for C_{60} both experimentally [76], and theoretically [77, 78, 79]. Recently, calculations of the static polarizability have been done for many of the other stable clusters in the fullerene family as well [80].

For the quasispherical fullerenes, there are two major contributions to $\alpha(\omega)$. There are the noninteracting single particle excitations which give rise to the noninteracting, or unscreened polarizability, α_0. This is defined by

$$\mathbf{p} = \alpha_0 \mathbf{E_{tot}} \tag{8.1}$$

where $\mathbf{E_{tot}}$ is the total electric field felt by the electrons. The polarizability α_0 can be calculated by perturbation theory with a knowledge of the single particle energy levels and wavefunctions. The second contribution arises from the interaction between single particle excitations, making $\mathbf{E_{tot}}$ different from the externally applied field $\mathbf{E}$. It is the interacting, or screened polarizability defined by

$$\mathbf{p} = \alpha\mathbf{E} \tag{8.2}$$

which is the experimentally accessible quantity. For C_{60}, α_0 is roughly four times greater than α. This reflects the fact that $\mathbf{E_{loc}} = \mathbf{E_{tot}} - \mathbf{E}$ is large, due to the build-up of charge on the spherical surface containing the ions [77].

The issue of the response of carbon nanotubes to electric fields is only beginning to be addressed. Random phase approximation (RPA) calculations of $\epsilon(\mathbf{q},\omega)$ have been done for electrons moving freely on a cylindrical surface [81]. Although these studies give qualitative insight into the positions of the zeros in $\epsilon(\mathbf{q},\omega)$, they are unable to take into account the effects arising from the nanotube electronic structure. The most important electronic feature is the existence of an energy gap in most tubes. The size of the gap can drastically affect the magnitude and overall behavior of response functions. This becomes particularly important when coupled with the fact that tubes with roughly the same radius can have very different band gaps. Cylindrical empty lattice calculations are unable to resolve these differences.

We address these issues by performing calculations which include the atomic structure of the carbon nanotubes. For simplicity, we focus on the $\mathbf{q} = 0$, $\omega = 0$ limit in an effort to understand the response to a static, uniform **E**-field. The polarizability per unit length of single nanotubes is calculated, instead of a dielectric constant, in order to draw comparisons with the polarizabilities of fullerene clusters. The most obvious difference between nanotubes and spherical fullerenes is their cylindrical structure. This causes the α_0 and α of Eqs. 8.1 and 8.2 to be highly anisotropic tensors with principle axes $\hat{\mathbf{z}}$ (parallel to the cylindrical axis) and $\hat{\mathbf{x}}$ (perpendicular to the cylindrical axis). Using a tight-binding model, we will show that α_{0zz} is roughly proportional to $\frac{R}{E_g^2}$, where E_g is the minimum direct band gap and R is the tube radius, while α_{0xx} is independent of E_g and is just proportional to R^2. Arguments analogous to those used for C_{60} [77, 82] are then applied which relate α_0 to α. We find that even for insulating tubes, α_{zz} is an order of magnitude larger than α_{xx}. This implies that an external field with equal z and x components will give rise to a dipole moment pointing mainly along the z direction.

The structure of this chapter is as follows: We first describe the details of the models used. The tight-binding theory of α_0 is presented, and then the classical electrostatic model relating α_0 to α. Then we present the results of the calculations for all of the

tubes studied. We explain the findings, and conclude.

8.1 Models

Our tight-binding model for α_0 is based on the Ehrenreich-Cohen formalism for the dielectric function of a crystalline solid [83]. In this approach, $\epsilon(\mathbf{q},\omega)$ is calculated within the RPA using Bloch states as the basis. If we neglect local field effects, the real part of the dielectric function is given by

$$\epsilon_1(\mathbf{q},\omega) = 1 + 2\frac{4\pi e^2}{q^2\Omega}\sum_{\mathbf{k},n_1,n_2}\frac{|\langle \mathbf{k},n_1|e^{-i\mathbf{q}\cdot\mathbf{r}}|\mathbf{k}+\mathbf{q},n_2\rangle|^2}{E_{n_1}(\mathbf{k}) - E_{n_2}(\mathbf{k}+\mathbf{q}) - \hbar\omega}[f^0_{n_2}(\mathbf{k}+\mathbf{q}) - f^0_{n_1}(\mathbf{k})] \quad (8.3)$$

where $\mathbf{q}$ is restricted to the first Brillouin zone (the factor of 2 is for spin). In order to invoke the tight-binding approximations, we express the Bloch states in terms of localized atomic-like orbitals.

$$|\mathbf{k},n_1\rangle = \sum_\mu C_\mu(\mathbf{k},n_1)\left(\frac{1}{\sqrt{N}}\sum_{\mathbf{R}'} e^{i\mathbf{k}\cdot\mathbf{R}'}|\phi_\mu(\mathbf{r}-\tau_\mu-\mathbf{R}')\rangle\right) \quad (8.4)$$

$$|\mathbf{k}+\mathbf{q},n_2\rangle = \sum_\nu C_\nu(\mathbf{k}+\mathbf{q},n_2)\left(\frac{1}{\sqrt{N}}\sum_{\mathbf{R}} e^{i(\mathbf{k}+\mathbf{q})\cdot\mathbf{R}}|\phi_\nu(\mathbf{r}-\tau_\nu-\mathbf{R})\rangle\right) \quad (8.5)$$

Here, $\phi_\mu(\mathbf{r})$ and $\phi_\nu(\mathbf{r})$ are localized orbitals, τ_μ and τ_ν are vectors denoting the positions of the orbitals within a unit cell, and $\mathbf{R}'$ and $\mathbf{R}$ are the lattice translation vectors. C_μ and C_ν are the coefficients in the expansion of the Bloch states in terms of the ϕ_μ and ϕ_ν Bloch sums. We may now form the matrix element which enters the Ehrenreich-Cohen formula. Setting $\mathbf{R}' = 0$ and multiplying by N, we have

$$\langle \mathbf{k},n_1|e^{-i\mathbf{q}\cdot\mathbf{r}}|\mathbf{k}+\mathbf{q},n_2\rangle = \sum_{\mu\nu\mathbf{R}} C^*_\mu(\mathbf{k},n_1)C_\nu(\mathbf{k}+\mathbf{q},n_2)e^{i[(\mathbf{k}+\mathbf{q})\cdot\mathbf{R}-\mathbf{q}\cdot\tau_\mu]}\langle\phi_\mu(\mathbf{r})|e^{-i\mathbf{q}\cdot\mathbf{r}}|\phi_\nu(\mathbf{r}-\mathbf{d})\rangle \quad (8.6)$$

where $\mathbf{d} = \tau_\nu - \tau_\mu + \mathbf{R}$.

Eventually, we will be interested in the $\mathbf{q}\to 0$ limit. Because $\phi_\mu(\mathbf{r})$ and $\phi_\nu(\mathbf{r})$ are localized, we may expand the matrix element in the RHS of Eq. 8.6 to first order in

$\mathbf{q} \cdot \mathbf{r}$, obtaining

$$\lim_{\mathbf{q}\to 0} \langle \phi_\mu(\mathbf{r}) | e^{-i\mathbf{q}\cdot\mathbf{r}} | \phi_\nu(\mathbf{r}-\mathbf{d}) \rangle = \langle \phi_\mu(\mathbf{r}) | \phi_\nu(\mathbf{r}-\mathbf{d}) \rangle - i \langle \phi_\mu(\mathbf{r}) | \mathbf{q}\cdot\mathbf{r} | \phi_\nu(\mathbf{r}-\mathbf{d}) \rangle \qquad (8.7)$$

Here we choose to work within orthogonal tight-binding; two localized orbitals have zero overlap unless they are equivalent, and are on the same site. Eq. 8.7 then becomes

$$\lim_{\mathbf{q}\to 0} \langle \phi_\mu(\mathbf{r}) | e^{-i\mathbf{q}\cdot\mathbf{r}} | \phi_\nu(\mathbf{r}-\mathbf{d}) \rangle = \delta_{\mu\nu}\delta_{\mathbf{R}0} - i\mathbf{q}\cdot\mathbf{R}_{\mu\nu}(\mathbf{d}) \qquad (8.8)$$

$\mathbf{R}_{\mu\nu}(\mathbf{d})$ is defined to be the matrix element of the operator $\mathbf{r}$ between ϕ_μ centered at the origin, and ϕ_ν centered at the position $\mathbf{d}$. We now have

$$\langle \mathbf{k}, n_1 | e^{-i\mathbf{q}\cdot\mathbf{r}} | \mathbf{k}+\mathbf{q}, n_2 \rangle \approx \sum_{\mu\nu\mathbf{R}} C^*_\mu(\mathbf{k}, n_1) C_\nu(\mathbf{k}+\mathbf{q}, n_2) e^{i[(\mathbf{k}+\mathbf{q})\cdot\mathbf{R} - \mathbf{q}\cdot\tau_\mu]} \left(\delta_{\mu\nu}\delta_{\mathbf{R}0} - i\mathbf{q}\cdot\mathbf{R}_{\mu\nu}(\mathbf{d}) \right) \qquad (8.9)$$

for $\frac{1}{|\mathbf{q}|}$ much greater than the characteristic unit cell length. Thus, we see that the matrix element is comprised of two terms. The first arises from the product of delta functions and will be referred to as the "delta term". It is equal to $\sum_\mu C^*_\mu(\mathbf{k}, n_1) C_\mu(\mathbf{k}+\mathbf{q}, n_2) e^{-i\mathbf{q}\cdot\tau_\mu}$. If there is only one atom per unit cell, or if $\mathbf{q}\cdot\tau_\mu = 0$ for all μ, this term is equal to zero. The second term depends on the dipole matrix elements $\mathbf{R}_{\mu\nu}(\mathbf{d})$ and will be called the "dipole term". Note that although the dipole matrix elements are multiplied by $\mathbf{q}$, both terms are the same order in $\mathbf{q}$ because of the $\mathbf{q}\cdot\tau_\mu$ term.

Unlike the quantities appearing in the delta term, the dipole matrix elements cannot be obtained as standard output from Slater-Koster tight-binding calculations. They must be input as external parameters. For the case of solids consisting solely of carbon, there are four localized orbitals in the tight-binding basis set used. They correspond to the carbon $2s$, $2p_x$, $2p_y$, and $2p_z$ states. At first sight, there are seven distinct dipole matrix elements, represented schematically in Fig. 8.1. One is on-site ($\mathbf{d} = 0$), while the others are off-site ($\mathbf{d} \neq 0$), (more precisely, there is a set of off-site dipole matrix elements for each order of nearest neighbors included). These matrix elements are special because

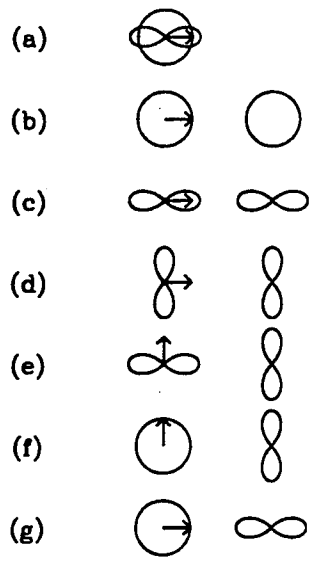

Figure 8.1: Various dipole matrix elements between s and p atomic-like states. The first (a) is on-site, while the rest are off-site. The arrow indicates the direction of the vector $\mathbf{r}$ which gives a nonvanishing contribution to the matrix element.

any $\mathbf{R}_{\mu\nu}(\mathbf{d})$ can be written as a linear combination of them, in a manner analogous to the Slater-Koster two-center integral formulae for Hamiltonian matrix elements [52].

On closer inspection it is seen that the matrix elements denoted by d and e in Fig. 8.1 are actually equal, for $xp_y = yp_x$. Also, the assumption of orthogonal tight-binding forces b,c, and d to be zero. This is because the origin may be translated to the point $\frac{1}{2}\mathbf{d}$, where the integrals are zero by parity. Thus, we are left with three special dipole matrix elements, one on-site (a), and two off-site (f, g). Their magnitudes will be denoted R_{sp}, $R_{sp\pi}$, and $R_{sp\sigma}$ respectively.

The $\mathbf{R}_{\mu\nu}(\mathbf{d})$ must now be related to the special matrix elements. For the $\mathbf{d} = 0$ case, we have simply

$$\mathbf{R}_{sp_x}(0) = \mathbf{R}_{p_x s}(0) = R_{sp}\hat{\mathbf{x}} \tag{8.10}$$

The off-site case is a bit more complicated. The relations can be derived by rotating the p orbital so that the axis of quantization is along $\mathbf{d}$. Let l, m, and n be the direction

cosines of $\mathbf{d}$ with respect to x, y, and z respectively. Then,

$$\mathbf{R}_{sp_x}(\mathbf{d}) = \mathbf{R}_{p_x s}(\mathbf{d}) = [(1-l^2)R_{sp\pi} + l^2 R_{sp\sigma}]\hat{\mathbf{x}} + [lm(R_{sp\sigma} - R_{sp\pi})]\hat{\mathbf{y}} + [ln(R_{sp\sigma} - R_{sp\pi})]\hat{\mathbf{z}} \tag{8.11}$$

$\mathbf{R}_{sp_y}$ and $\mathbf{R}_{sp_z}$ are obtained from Eqs. 8.10, 8.11 by the cyclic permutations $x \rightarrow y \rightarrow z$, $l \rightarrow m \rightarrow n$. All other dipole matrix elements are zero within the framework of orthogonal tight-binding. For simplicity, we limit the off-site matrix elements to include first nearest neighbors only. It is demonstrated below that this is not a serious restriction for the systems studied.

We define the unscreened polarizability per unit cell of a crystal by the relation

$$\lim_{\mathbf{q}\rightarrow 0} \epsilon_1(\mathbf{q},\omega) = 1 + \frac{4\pi}{\Omega}\alpha_0(\omega) \tag{8.12}$$

where $\epsilon_1(\mathbf{q},\omega)$ is given in Eq. 8.3. If there is no interaction between atoms in different unit cells, $\alpha_0(\omega)$ is just equal to the unscreened polarizability of the single molecule contained in each cell. Both ϵ_1 and α_0 are second rank tensors. The individual components may be calculated by first determining the principle axes by symmetry, and then letting $\mathbf{q} \rightarrow 0$ along these directions. This yields the diagonal elements corresponding to each axis.

There are two sets of parameters which must be input into this model: Slater-Koster tight-binding parameters which determine the energy eigenvalues and eigenstates, and dipole matrix elements. All carbon nanotubes are sp^2 bonded systems, so we use the first and second nearest neighbor Slater-Koster parameters of Tomanek and Louie [4]. These were originally designed to reproduce the band structure of graphite, and since have been applied successfully to the study of carbon nanotubes [58]. In order to determine the optimal values for R_{sp}, $R_{sp\sigma}$, and $R_{sp\pi}$, we must choose a reference system for which either ϵ_1 or α_0 is known. Because orthogonal tight-binding is used, it is desirable to choose a system which has a bonding configuration similar to that of the tubes. This will ensure the transferability of the parameters. C_{60} is a predominantly sp^2 bonded

system with an experimentally determined screened polarizability. Unfortunately, our tight-binding model only has access to the unscreened polarizability. This has, however, been determined theoretically by Pederson and Quong [38] using *ab initio* local density functional theory. They obtained a result of $311\mathring{A}^3$ per molecule for $\alpha_0(\omega = 0)$, roughly four times larger than the experimental value for the screened polarizability [76], as expected. We have calculated $\alpha_0(\omega = 0)$ of C_{60} using our model for a wide range of different R_{sp}, $R_{sp\sigma}$, and $R_{sp\pi}$. We find a sensitive dependence of $\alpha_0(\omega = 0)$ on R_{sp}, whereas the dependence on the off-site matrix elements is negligible. Therefore, $R_{sp\sigma}$ and $R_{sp\pi}$ may be set equal to zero. The local density functional result is then obtained if $R_{sp} = 0.5\mathring{A}$. If $R_{sp\sigma}$ and $R_{sp\pi}$ are changed, the value of $\alpha_0(\omega = 0)$ is only slightly altered. For instance, if $R_{sp\sigma}$ and $R_{sp\pi}$ are both set equal to $0.5\mathring{A}$ while keeping $R_{sp} = 0.5\mathring{A}$, $\alpha_0(\omega = 0)$ is changed by less than 5%.

We have therefore constructed a tight-binding model of the $\mathbf{q} = 0$ dielectric response function without local field effects for sp^2 bonded carbon systems, in which the only external parameter is an on-site $s - p$ dipole matrix element. Before the issue of local fields is addressed, two points must be made: 1) The value of $R_{sp} = 0.5\mathring{A}$ is not to be understood as the dipole matrix element between true atomic carbon $2s$ and $2p$ wavefunctions. As stated above, the localized orbitals of this model are orthogonalized orbitals which may be very different from their atomic counterparts. 2) The parameters of the model have been chosen to describe sp^2 bonded systems. If we wish to study systems with other bonding configurations, both the Slater-Koster parameters, and the dipole matrix elements may need to be changed.

The difference between the unscreened polarizability, α_0, defined in Eq. 8.1, and the screened polarizability, α, of Eq. 8.2 is due to the difference between the total and applied electric fields. This arises because the virtual single-particle excitations have electric charge, and produce a local field. Stated another way, α_0 only accounts for the polarization of the individual single particle wavefunctions, while α includes their

mutual interaction as well. For most bulk crystals, local field effects change ϵ by roughly 10% [84]. For surfaces, however, the effect is much greater due to the build-up of bound surface charge. Since fullerenes are closed surfaces, local field effects are large. This is the reason for the factor of four difference between α_0 and α of C_{60}.

Local fields can be taken into account within RPA by considering charge fluctuations inside a unit cell, i.e. $\mathbf{q}$ of Eq. 8.3 outside the first Brillouin zone. From the previous section, we see that our tight-binding model is only valid for $\mathbf{q} \rightarrow 0$. Thus, a straightforward application of RPA is not possible here. Instead we can take advantage of the simple geometries of fullerenes, and construct classical models that relate $\mathbf{E}$ to $\mathbf{E_{tot}}$. This determines the relationship between α_0 and α via Eqs. 8.1 and 8.2. The simplest possible model is one in which the local field, $\mathbf{E_{loc}} = \mathbf{E_{tot}} - \mathbf{E}$, is constant within the fullerene. This is reasonable if the fullerene is ellipsoidal [85].

As an example, consider C_{60} [77, 82]. If a spatially constant external field, $\mathbf{E}$, is applied, bound charge will form at the surface of the sphere. This will create a depolarization field, $\mathbf{E_{loc}}$, pointing opposite to $\mathbf{E}$. If we assume that this field is constant within the sphere, then $\mathbf{E_{tot}}$ will be constant inside as well. We can relate the magnitude of this field to the induced dipole moment, $E_{loc} = \frac{p}{R^3}$. Eqs. 8.1 and 8.2 then give us the relationship between α_0 and α:

$$\alpha(\omega) = \frac{\alpha_0(\omega)}{1 + \frac{\alpha_0(\omega)}{R^3}} \tag{8.13}$$

We see that α is less than α_0, as expected. However, the maximum value of α is $R^3 = 45\mathring{A}^3$. This is inconsistent with the experimental result of $80\mathring{A}^3$ [76, 82]. The discrepancy can be understood by noting that the electrons which participate in the screening are not confined to the sphere containing the ions. This can be taken into account with a single parameter, δR, such that the "effective radius" is $R_{eff} = R + \delta R$ [82],

$$\alpha(\omega) = \frac{\alpha_0(\omega)}{1 + \frac{\alpha_0(\omega)}{R_{eff}^3}} \tag{8.14}$$

If we take the local density functional theory value of $311\mathring{A}^3$ for α_0, the experimental value of α is reproduced when $\delta R = 1.2\mathring{A}$.

The same arguments will now be applied to single-wall carbon nanotubes. Again, the goal will be to relate $\mathbf{E}$ to $\mathbf{E_{tot}}$ in order to determine the relationship between α_0 and α. The crucial difference between nanotubes and C_{60} is their cylindrical structure. If $\mathbf{E}$ is in the $\hat{\mathbf{x}}$ direction, bound charge will build up on the surface and create a local depolarization field. If $\mathbf{E}$ is along $\hat{\mathbf{z}}$, there will be no bound surface charge, so $\mathbf{E_{loc}} = 0$ within this model. This is, of course, only true in the ideal case of an infinitely long tube. For a tube of finite length, an external field in the $\hat{\mathbf{z}}$ direction will induce bound charge at the ends. However, the resulting local field will be negligible as long as the length is much larger than the diameter. Thus, we will assume that $\mathbf{E_{loc}}$ has no z component.

Since the principle axes of α_0 and α are $\hat{\mathbf{z}}$ and $\hat{\mathbf{x}}$ (see below), we need only consider the two cases of $\mathbf{E}$ along these directions. Let $\mathbf{E}$ be along $\hat{\mathbf{x}}$ ($\perp \hat{\mathbf{z}}$). There will then be a local field in the x direction. Assume that it is constant inside the tube. The surface charge density per length which gives rise to a constant field along $\hat{\mathbf{x}}$ is of the form $\sigma(\phi) = \sigma_0 cos\phi$, where ϕ is the azimuthal angle measured with respect to $\hat{\mathbf{x}}$. The resulting dipole moment per length is

$$p_x = R\int d\phi x\sigma(\phi) = 2R\int_0^\pi d\phi R cos\phi\sigma_0 cos\phi = \pi R^2\sigma_0 \tag{8.15}$$

With this and Eq. 8.1, we have

$$\sigma(\phi) = \frac{p_x}{\pi R^2}cos\phi = \frac{\alpha_{0xx}E_{totx}}{\pi R^2}cos\phi \tag{8.16}$$

where σ, p, and α are all defined per unit length. We can now calculate the local electric field due to $\sigma(\phi)$. It can be shown to be constant within the tube and equal to

$$\mathbf{E_{loc}} = -\frac{2\alpha_{0xx}E_{totx}}{R^2}\hat{\mathbf{x}} \tag{8.17}$$

Knowing that $\mathbf{E_{tot}} = \mathbf{E} + \mathbf{E_{loc}}$, we may use Eqs. 8.1, 8.2, and 8.17 to obtain

$$\alpha_{xx} = \frac{\alpha_{0xx}}{1 + 2\frac{\alpha_{0xx}}{R^2}} \tag{8.18}$$

If $\mathbf{E}$ is along $\hat{\mathbf{z}}$, then $\mathbf{E_{loc}} = 0$. This means that $\mathbf{E_{tot}} = \mathbf{E}$ and we get simply

$$\alpha_{zz} = \alpha_{0zz} \tag{8.19}$$

Note that all polarizabilities are defined per unit length.

If we combine Eqs. 8.18 and 8.19 and restore the frequency dependance, we can write $\alpha(\omega)$ as a matrix

$$\alpha(\omega) = \begin{pmatrix} \frac{\alpha_{0xx}(\omega)}{1+2\frac{\alpha_{0xx}(\omega)}{R^2}} & 0 \\ 0 & \alpha_{0zz}(\omega) \end{pmatrix} \tag{8.20}$$

It should be pointed out that α is actually a 3×3 matrix, for $\hat{\mathbf{x}}$ can lie anywhere in the plane perpendicular to $\hat{\mathbf{z}}$. Since all x axes are equivalent, we supress one dimension. As for C_{60}, $\alpha_{xx} < \alpha_{0xx}$; Eq. 8.18 is the two dimensional analogue of Eq. 8.13. Likewise, we anticipate that it will be necessary to replace R by $R_{eff} = R + \delta R$. The question of what is the appropriate δR is not a simple one. However, we expect the magnitude of δR to reflect the intrinsic features of π-electron systems, such as the extent of a p orbital, etc. Thus, we fix $\delta R = 1.2\mathring{A}$ as for C_{60}. We show below that the results are not sensitive to this choice.

The most important feature of Eq. 8.20 is that α_{zz} remains unscreened. This has two interesting consequences: 1) Even if α_{0xx} and α_{0zz} are comparable, α_{zz} will be significantly greater than α_{xx}. This means that an external electric field with equal z and x components will give rise to an electric dipole moment pointing primarily along $\hat{\mathbf{z}}$. 2) The response of the tubes to electric fields will be particularly sensitive to the details of the tube electronic structure. As we stated above, α_0 is determined from the single-particle energies and eigenstates (Eq. 8.3). If the energy gap is small, α_{0zz} may be quite large. Because of Eq. 8.19, α_{zz} will be large as well. This is not true for the caged fullerenes, in which all components of the polarizability tensor are governed by expressions like Eq. 8.14; as long as α_0 is large enough, α is completely determined by

$R_{eff} \sim R$. The absence of a large screening field along the axes of the tubes makes it necessary to consider band structure effects in these systems.

We are now in a position to calculate $\alpha(\omega = 0)$ for a wide range of tubes. Our strategy is simple. First, a tight-binding calculation is performed to determine the $E_n(\mathbf{k})$, and $C_\mu(\mathbf{k}, n)$ appearing in Eqs. 8.3 and 8.9. Then a small $\mathbf{q}$ is chosen along $\hat{\mathbf{z}}$. $\epsilon_1(\mathbf{q}, \omega = 0)$ without local fields is calculated using Eqs. 8.3, 8.9, and 8.10, and $R_{sp} = 0.5\mathring{A}$ ($R_{sp\sigma} = R_{sp\pi} \equiv 0$). Smaller and smaller $\mathbf{q}$ are chosen, and $\lim_{\mathbf{q}\to 0} \epsilon_1(\mathbf{q}, \omega = 0)$ is obtained. We then choose $\mathbf{q}$ along $\hat{\mathbf{x}}$ and repeat the procedure. The $\alpha_0(\omega = 0)$ tensor is calculated using Eq. 8.12. Finally, we use the electrostatic model of Eq. 8.20 with R replaced by $R_{eff} = R + 1.2\mathring{A}$ to determine the $\alpha(\omega = 0)$ tensor. Results of these calculations are presented for tubes having a variety of different radii and band gaps in the next section.

8.2 Results

Before results are presented, it is worth considering the criteria on n_1 and n_2 such that the (n_1, n_2) tube has the symmetry required by Eq. 8.20. We have assumed above that $\hat{\mathbf{x}}$ and $\hat{\mathbf{z}}$ are principle axes of the α_0 and α tensors. It can be shown that any second-rank symmetric tensor in three dimensions is "isotropic" in a plane perpendicular to a three or more-fold axis of rotation [85]; i.e. every direction perpendicular to the rotation axis is a principle axis. Thus, all tubes of the form $(n, 0)$ and (n, n) with $n \geq 3$ have the required symmetry. The same statement is true for screw axes. Therefore all (n_1, n_2) tubes with $n_1 \neq n_2$ are included as well. This set comprises all tubes of interest, for the ones not included are probably too small to ever be found. In what follows, we may refer to the direction $\hat{\mathbf{x}}$ without specifying where it is pointing with respect to the individual atoms [86].

We have calculated the static unscreened and screened polarizabilities of the $(n, 0)$

tubes for $9 \leq n \leq 19$. The metallic (n,n) tubes $(4,4)$, $(5,5)$ and $(6,6)$ have also been studied, as well as the chiral tubes $(4,2)$ and $(5,2)$. Table 8.1 contains a list of the results. Since $\alpha_{0zz} = \alpha_{zz}$, only α_{zz} is shown. In the cases where $n_1 - n_2$ is a multiple of three, the minimum band gap is very small (or zero), and α_{zz} is effectively infinite. Thus, we choose not to list it here. Note that this is not true for α_{0xx}. This will be discussed at length below.

The first issue to be addressed is the overall magnitude of the polarizabilities. If we multiply each value by a length, and divide by the number of carbon atoms per that length, we obtain the polarizabilities per atom ($\mathring{A}^3$). We may compare these to the polarizabilities per atom of fullerene clusters. Because tubes are cylinders and the clusters are quasispherical, their local field contributions are quite different. Therefore, it is only meaningful to compare the unscreened polarizabilities. The quantity which is most analogous to α_0 of C_{60} is α_{0xx}. Its value increases monotonically with R. It is $3.8\mathring{A}^3/atom$ for the $(4,2)$ tube, and $8.5\mathring{A}^3/atom$ for $(19,0)$. This is consistent with the C_{60} value of roughly $5\mathring{A}^3/atom$. The general increase with radius is also consistent with a similar trend in fullerene clusters [80] if we assume that α is a monotonically increasing function of α_0, as in Eq. 8.14. We see that α_{0zz} is considerably larger than α_{0xx}. This is a result of the anisotropy of the single particle wavefunctions (i.e., graphite is more polarizable along the sheet plane direction than in the perpendicular direction). It manifests itself in the matrix elements of Eq. 8.3.

The increase of α_{0xx} with radius can be quantified by plotting α_{0xx} versus R^2, as shown in Fig. 8.2. We see that α_{0xx} is roughly proportional to R^2 with a slope of 2.6, independent of the tube chirality and band gap. Even the zero gap (n,n) tubes have finite α_{0xx}, and obey this simple relation. The fact that α_{0xx} is completely independent of the minimum band gap is particularly striking. It suggests that there are selection rules which force the matrix elements of Eq. 8.3 to be zero in cases where the energy denominator is small. We will explore the origin of these selection rules in the next

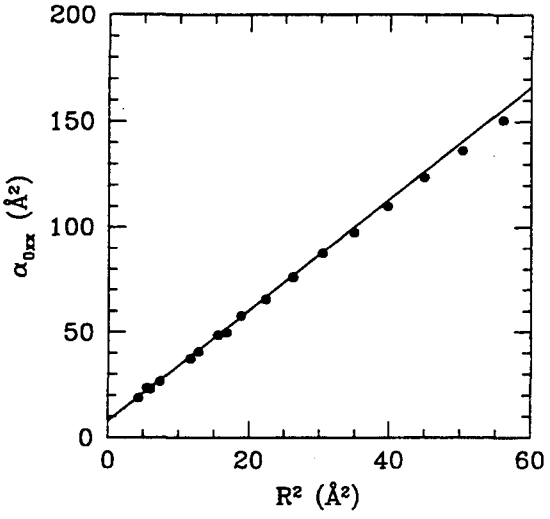

Figure 8.2: Plot of α_{0xx} versus R^2 for the tubes studied. The solid line is a linear least squares fit to the points.

section.

Unlike α_{0xx}, α_{0zz} ($= \alpha_{zz}$ in the present theoretical framework) is highly dependent on the minimum gap. In cases where the gap is zero, α_{0zz} is infinite. This means that the above selection rules for the matrix elements do not apply when $\mathbf{q}$ is in the z direction. There is also a dependence of this quantity on the tube radius. In fact, α_{0zz} is approximately linear in $\frac{R}{E_g^2}$, as shown in Fig. 8.3. An explanation of this behavior is given in the following section.

As can be seen from Table 8.1, $\alpha_{xx} \sim \frac{1}{5}\alpha_{0xx}$ for each tube. This is a consequence of Eq. 8.18, with R replaced by $R+\delta R = R+1.2\mathring{A}$. These results are relatively insensitive to the choice of δR; a factor of two increase or decrease in δR changes α_{xx} by no more than 40%. The ratio $\frac{\alpha_{zz}}{\alpha_{xx}}$ is > 11 for all tubes studied. For very small gap tubes, the ratio is extremely large. This, along with Eq. 8.2, justifies our prediction that an external electric field with equal z and x components will give rise to a dipole moment pointing mainly along $\hat{\mathbf{z}}$. Likewise, the magnitude of this dipole moment will depend mostly on

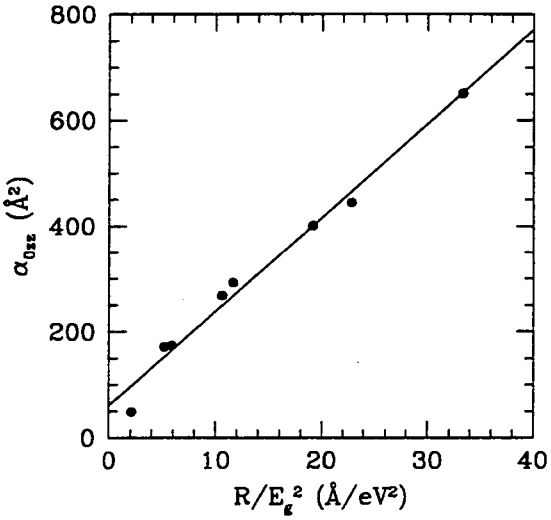

Figure 8.3: Plot of α_{0zz} $(= \alpha_{zz})$ versus $\frac{R}{E_g^2}$ for the (n_1, n_2) tubes studied where $n_1 - n_2$ is *not* equal to an integer multiple of three. A linear least squares fit is also shown.

α_{zz} and will therefore be roughly proportional to $\frac{R}{E_g^2}$. It should be understood that the relationship implied by Eq. 8.18 is approximate. More sophisticated models for local field effects may yield results different from those presented here. However, we expect the general features to be correct.

8.3 Discussion

In this section, we explore the origins of the dependence of α_{0xx} and α_{0zz} on R and E_g. First, we see why α_{0xx} is independent of the minimum gap. Then its proportionality to R^2 is explained using an empty lattice model. Finally, the linear variation of α_{0zz} with $\frac{R}{E_g^2}$ is understood from the point of view of a simple model based on the oscillator strength sum rule.

In order for α_{0xx} to be completely independent of the minimum gap, the matrix elements of Eq. 8.3 must be zero when the energy denominator has its smallest values. We can see that this is true by examining the quantity $\langle \mathbf{k}, n_1 | e^{-i\mathbf{q}\cdot\mathbf{r}} | \mathbf{k}+\mathbf{q}, n_2 \rangle$ when

$\mathbf{q} = q\hat{\mathbf{x}}$. Since we are considering individual tubes, the states $|\mathbf{k}, n_1\rangle$ and $|\mathbf{k}+\mathbf{q}, n_2\rangle$ are localized along the directions perpendicular to $\hat{\mathbf{z}}$. The matrix element may then be expanded to first order in $\mathbf{q}\cdot\mathbf{r}$ $(= qx)$. Also, the absence of dispersion in the x direction allows us to write $|\mathbf{k}+\mathbf{q}, n_2\rangle = |\mathbf{k}, n_2\rangle$. This yields

$$\lim_{\mathbf{q}\to 0}\langle \mathbf{k}, n_1|e^{-i\mathbf{q}\cdot\mathbf{r}}|\mathbf{k}+\mathbf{q}, n_2\rangle = \langle \mathbf{k}, n_1|\mathbf{k}, n_2\rangle - i\langle \mathbf{k}, n_1|\mathbf{q}\cdot\mathbf{r}|\mathbf{k}, n_2\rangle = -iq\langle \mathbf{k}, n_1|\hat{\mathbf{x}}\cdot\mathbf{r}|\mathbf{k}, n_2\rangle \tag{8.21}$$

for $n_1 \neq n_2$. As discussed by previous workers [13, 14], the Bloch states of nanotubes arise from lines of allowed k-vectors of the graphite sheet Brillouin zone which point along $\hat{\mathbf{k}_z}$. In the Appendix at the end of this chapter, we use group theory to show that $\langle \mathbf{k}, n_1|\hat{\mathbf{x}}\cdot\mathbf{r}|\mathbf{k}, n_2\rangle = 0$ if $|n_1\rangle$ and $|n_2\rangle$ arise from the same line, as long as it is *not* the line which is farthest from Γ in $(n, 0)$ and (n, n) tubes with odd n. In the absence of strong $\sigma - \pi$ hybridization [58], the minimum direct gap is always between states coming from the same line. This line intersects Γ for the case of (n, n) tubes, and is not the line farthest from Γ in $(n, 0)$ tubes unless $n < 5$. This means that $\langle \mathbf{k}, n_1|e^{-iq\hat{\mathbf{x}}\cdot\mathbf{r}}|\mathbf{k}+q\hat{\mathbf{x}}, n_2\rangle$ is zero between HOMO and LUMO states of all chiral tubes, (n, n) tubes, and $(n, 0)$ tubes with $R > 2.0\mathring{A}$. Thus, it follows that α_{0xx} is independent of of the HOMO and LUMO states and hence E_g in these cases.

The fact that α_{0xx} is approximately proportional to R^2 can be best understood by appealing to an empty lattice model of electrons moving freely on a cylinder of infinitesimal thickness. Such a model has been used by several authors to study collective modes of nanotubes [81]. In this approach, the π-electron Bloch states of a tube of radius R may be written as $\langle \mathbf{r}|k, n\rangle = \frac{1}{2\pi\sqrt{R}}e^{ikz}e^{in\phi}$ where n is an integer. Their energies are $E_n(k) = \frac{\hbar^2}{2m^*}\left[\left(\frac{n}{R}\right)^2 + k^2\right]$. The band index, n, now refers to the rotational sub-bands of the π-electron complex which arise from the lines of allowed k-vectors mentioned above. Each one of these bands will be folded back in a reduced zone scheme, and will acquire gaps at the Fermi energy with the addition of the crystalline potential. Therefore, every

free-electron band corresponds to many bands of the tight-binding calculation. We choose to use an extended-zone scheme to simplify the argument that follows.

From the considerations outlined above, such as the absence of dispersion in the $\hat{\mathbf{x}}$ direction, we have:

$$\alpha_{0xx} = e^2 \int \frac{dk}{2\pi} \sum_{n_1,n_2} \frac{|\langle k, n_1|\hat{\mathbf{x}} \cdot \mathbf{r}|k, n_2\rangle|^2}{E_{n_1}(k) - E_{n_2}(k)} [f^0_{n_2}(k) - f^0_{n_1}(k)] \tag{8.22}$$

The matrix elements of this expression can be shown to be independent of k and proportional to R. They are only nonzero if n_1 and n_2 differ by one. The energy denominator is equal to $\frac{\hbar^2}{2m^* R^2}({n_1}^2 - {n_2}^2)$ independent of k. Thus,

$$\alpha_{0xx} \propto \int_0^{k_F} dk \sum_{n=0}^{\infty} \frac{R^2 \frac{2m^* R^2}{\hbar^2}}{2n-1} [f^0_{n-1}(k) - f^0_n(k)] \tag{8.23}$$

k_F is the Fermi wavevector, equal to $\frac{\sqrt{2m^* E_F}}{\hbar}$. It is the wavevector where the $n = 0$ band crosses E_F. Let k_n denote the k-point where the nth band crosses E_F. We then have $\cdots < k_2 < k_1 < k_0 = k_F$. Because of the difference of zero temperature Fermi factors, we are forced to set $n = j$ when $k \in [k_j, k_{j-1}]$. The integral can then be evaluated in piecewise fashion over the intervals $[k_n, k_{n-1}]$

$$\alpha_{0xx} \propto \frac{2m^* R^4}{\hbar^2} \sum_{n=0}^{n_F} \frac{k_{n-1} - k_n}{2n-1} \tag{8.24}$$

n_F is the largest n such that $\frac{\hbar^2 n^2}{2m^* R^2} < E_F$. The interval length $k_{n-1} - k_n = \sqrt{\frac{2m^* E_F}{\hbar^2} - \left(\frac{n-1}{R}\right)^2} - \sqrt{\frac{2m^* E_F}{\hbar^2} - \left(\frac{n}{R}\right)^2}$ may be approximated by

$$k_{n-1} - k_n \approx \frac{\hbar}{2\sqrt{2m^* E_F} R^2} (2n-1) \tag{8.25}$$

for $n \ll n_F$. These are the terms which contribute most to the sum. If we neglect the large n terms, Eqs. 8.24, and 8.25 yield the approximate relation

$$\alpha_{0xx} \propto \sqrt{\frac{m^*}{E_F}} R^2 \tag{8.26}$$

Since m^* and E_F are roughly independent of the tube size (for tubes large enough so that the zone-folding picture applies), $\alpha_{0xx} \propto R^2$ as expected. Therefore, we see that

the behavior shown in Fig. 8.2 is due to three properties of the systems: 1) The matrix element of Eq. 8.21 is proportional to R, and is only nonzero when n_1 and n_2 correspond to rotational sub-bands which are adjacent in energy. 2) The energy difference between rotational sub-bands is proportional to $\frac{1}{R^2}$. 3) m^* and E_F are roughly independent of R. Although this discussion has involved a cylindrical shell empty lattice model, the conclusions are valid for nanotubes large enough so that hybridization effects do not play a dominant role.

We now turn to a discussion of α_{0zz}. For this case, we consider Eq. 8.3 with $\mathbf{q} = q\hat{\mathbf{z}}$. The relevant Bloch states are $\mathbf{q}$-dependent, and the matrix elements are of the form $\langle \mathbf{k}, n_1 | f(q,z) | \mathbf{k}+\mathbf{q}, n_2 \rangle$. Therefore, the above selection rules do not apply; the matrix elements between HOMO and LUMO bands are nonzero. Because the minimum gap in most tubes is small, we expect α_{0zz} to be dominated by terms for which the energy denominator is roughly equal to E_g. This makes it reasonable to assume that the linear dielectric response will be adequately described by a model in which all virtual single particle transitions of a given tube have the same energy, $\bar{E}_g$, which is of the order of E_g. A model of this type has been constructed for $\epsilon(\mathbf{q}=0, \omega=0)$ from a generalized Thomas-Rieche-Kuhn sum rule [87],

$$\epsilon = 1 + \left(\frac{\hbar \omega_p}{\bar{E}_g} \right)^2 \tag{8.27}$$

ω_p is the plasma frequency, equal to $\sqrt{\frac{4\pi e^2 N_e}{\Omega m}}$. N_e is the number of electrons per cell which participate in the screening. For this we use $4/atom$, because one carbon $2s$ and three $2p$ electrons were considered in the RPA calculation. $\bar{E}_g$ is the "average gap" of the system. The approximate linearity in the separation of the π-bands near the Fermi level suggests that $\bar{E}_g$ will vary linearly with E_g (since there is much less contribution from states far away from E_F).

If we use Eq. 8.12 to convert Eq. 8.27 into an expression involving α_{0zz}, we get

$$\alpha_{0zz} = \left[\frac{8\pi\hbar^2 e^2}{mA}\right]\left(\frac{R}{\bar{E}_g^{\,2}}\right) \tag{8.28}$$

where A is the area per atom on the graphite sheet (again, α_{0zz} is defined per unit length). This establishes the linear dependence on $\frac{R}{E_g^2}$ since we expect $\bar{E}_g \propto E_g$. We may use the plot of Fig. 8.3 to determine the precise relation between $\bar{E}_g$ and E_g. The least squares linear fit to the points has a slope of 17.8 $eV^2\mathring{A}$. This, along with Eq. 8.28, gives $\bar{E}_g \sim 5.4E_g$; a reasonable result considering that the HOMO and LUMO bands of tubes have large dispersion.

8.4 Conclusions

We have used a tight-binding model and a classical electrostatic argument to calculate the static polarizability of single-wall carbon nanotubes. It was shown that the polarizability tensor is highly anisotropic, a consequence of the inherent anisotropy of the tubes. The polarizability for external fields in the $\hat{\mathbf{z}}$ direction is considerably larger than that for fields along the $\hat{\mathbf{x}}$ direction. From this we conclude that a randomly oriented field will, on average, give rise to a dipole moment pointing mainly along the tube axis. The size of the moment is proportional to the tube radius divided by the square of the band gap. This may have significant consequences, for it suggests that tubes with different atomic arrangements respond very differently to external fields, even if the tube radii are similar. The issue of nonzero frequency, though not considered here, can be addressed easily within this model. One must only use a range of different ω in the denominator of Eq. 8.3. In addition, the calculated matrix elements and their associated selection rules can be used to compute the frequency dependent transverse dielectric function. This could provide a key to understanding the results of subsequent absorption measurements. The exotic geometric and electronic structures of carbon nanotubes could provide some unique dielectric responses.

Appendix

We wish to show that $\langle n_1|\hat{\mathbf{x}}\cdot\mathbf{r}|n_2\rangle = 0$ if $|n_1\rangle$ and $|n_2\rangle$ arise from the same line of allowed k-vectors pointing along $\hat{\mathbf{k}_z}$. To do this, we must consider the symmetry groups of tubes. We first discuss the non-chiral $(n,0)$ and (n,n) tubes. They have symmorphic space groups, with the point subgroups C_{nv} [15]. C_{nv} consists of powers of C_n rotations, and reflections. For n even, C_{nv} has $\frac{n}{2}+3$ irreducible representations labeled $A_1, A_2, B_1, B_2, E_1, E_2, ..., E_{\frac{n}{2}-1}$. A_1 is the totally symmetric representation. It has z as a basis function (the z direction is defined to be the C_n axis). For odd n, C_{nv} has the $\frac{n-1}{2}+2$ irreducible representations $A_1, A_2, E_1, E_2, ..., E_{\frac{n-1}{2}}$. Again, A_1 is the symmetric representation which has the symmetry of z. For both even and odd cases, E_1 has x and y as basis functions. The states $|n_1\rangle$ and $|n_2\rangle$ are eigenstates of the Hamiltonian, so they transform according to irreducible representations of the point group. The operator $\hat{\mathbf{x}}\cdot\mathbf{r}$ can also be classified according to symmetry. $\langle n_1|\hat{\mathbf{x}}\cdot\mathbf{r}|n_2\rangle$ will be zero if the combined symmetry does not contain the totally symmetric representation; i.e.

$$\Gamma(|n_1\rangle)\times\Gamma(\hat{\mathbf{x}}\cdot\mathbf{r})\times\Gamma(|n_2\rangle)\not\ni A_1 \Longrightarrow \langle n_1|\hat{\mathbf{x}}\cdot\mathbf{r}|n_2\rangle = 0 \tag{8.29}$$

Because $\hat{\mathbf{x}}\cdot\mathbf{r} = x$, $\Gamma(\hat{\mathbf{x}}\cdot\mathbf{r}) = E_1$. Thus,

$$\Gamma(|n_1\rangle)\times\Gamma(|n_2\rangle)\not\ni E_1 \Longrightarrow \langle n_1|\hat{\mathbf{x}}\cdot\mathbf{r}|n_2\rangle = 0 \tag{8.30}$$

It can be shown that states which arise from particular lines transform according to specific irreducible representations of the point group. As an example, consider the $(4,4)$ tube. Its corresponding allowed lines are shown in Fig. 8.4 along with the symmetrical Brillouin zone of the graphite sheet. The dashed lines mark the boundary of the Brillouin zone of the $(1,1)$ unit. Each line is associated with one or more irreducible representations of C_{4v}. The center line intersects the Γ-point of the graphite sheet, and is associated with A_1 and A_2. The lines farthest from Γ are associated with B_1 and

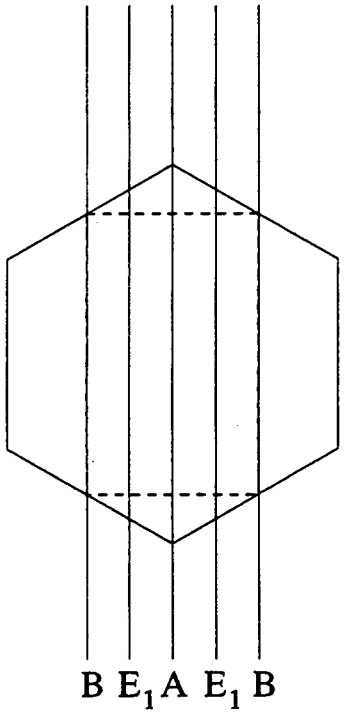

Figure 8.4: Allowed k-vectors of the $(4,4)$ tube mapped onto the graphite sheet Brillouin zone. The dashed lines enclose the Brillouin zone of a single $(1,1)$ unit. Each line is identified with irreducible representations of the point group C_{4v}. A denotes A_1, A_2, and B denotes B_1, B_2.

B_2. The two middle lines on either side of the center belong to E_1. Similar assignments can be made for all even n (n,n) tubes. It is always true that A_1, A_2 correspond to the center line, and B_1, B_2 to the lines farthest out. $E_1, E_2, ..., E_j, ...$ are always between the two, with E_j being associated with the jth lines away from the center on both sides. The picture for odd n (n,n) tubes is the same, except that the lines farthest from Γ belong to $E_{\frac{n-1}{2}}$. For $(n,0)$ tubes, we must only rotate the hexagon by 90 degrees, and change the density of the lines [14]. Everything else remains the same.

Assume that $|n_1\rangle$ and $|n_2\rangle$ arise from the same line. There are three cases: 1) $\Gamma(|n_1\rangle) = \Gamma(|n_2\rangle)$. 2) $\Gamma(|n_1\rangle) = A_1$, $\Gamma(|n_2\rangle) = A_2$ (or vice versa). 3) $\Gamma(|n_1\rangle) = B_1$, $\Gamma(|n_2\rangle) = B_2$ (or vice versa). In all C_{nv} groups, $A_1 \times A_2$ and $B_1 \times B_2$ do not contain E_1 [88]. Thus, $\langle n_1|\hat{\mathbf{x}} \cdot \mathbf{r}|n_2\rangle = 0$ for cases 2 and 3. If n is even, the direct product of an irreducible representation with itself never contains E_1, so the matrix element is zero for case 1 as well. However, if n is odd, $E_{\frac{n-1}{2}} \times E_{\frac{n-1}{2}} \ni E_1$, while all other such products do not contain E_1. This means that $\langle n_1|\hat{\mathbf{x}} \cdot \mathbf{r}|n_2\rangle$ can be nonzero only if $|n_1\rangle$ and $|n_2\rangle$ arise from the line farthest from Γ in odd-n tubes.

We now turn to chiral tubes. The space groups of these tubes are nonsymmorphic. However, factor groups which are analogous to the above point groups can be constructed from powers of screw operations; i.e. rotations about z followed by translations along z. This was done recently by Jishi *et al* [89] for all chiral tubes. They showed that each chiral tube has a factor group consisting of powers of a single screw operation. The factor groups are all isomorphic to the point groups C_n with n even. The irreducible representations are $A, B, E_1, E_2, ..., E_{\frac{n}{2}-1}$. A is the symmetric representation, and x, y transform as E_1. Again, we may use Eq. 8.30 to carry out the analysis.

Just as for non-chiral tubes, states which arise from particular lines transform like particular irreducible representations of the factor group. The line intersecting the Γ-point is associated with A, the farthest lines with B, and the others with $E_1, E_2, ...$ etc. For these groups, the direct product of an irreducible representation with itself never

contains E_1. Thus, $\langle n_1|\hat{\mathbf{x}}\cdot\mathbf{r}|n_2\rangle$ is always zero if $|n_1\rangle$ and $|n_2\rangle$ arise from the same line. This is true for all chiral tubes.

Table 8.1: Static Polarizabilities per unit length (in $\AA^2$) of various carbon nanotubes of radius R ($\AA$). In cases where $n_1 - n_2$ is a multiple of three, α_{zz} is extremely large and is not given.

Tube (n_1, n_2)	R	α_{zz}	α_{0xx}	α_{xx}
(9,0)	3.57	—	40.6	8.9
(10,0)	3.94	174.7	48.5	10.3
(11,0)	4.33	171.6	57.8	12.1
(12,0)	4.73	—	65.7	13.9
(13,0)	5.12	292.4	76.1	15.8
(14,0)	5.52	268.3	87.4	17.9
(15,0)	5.91	—	97.4	20.1
(16,0)	6.30	445.5	109.9	22.4
(17,0)	6.70	401.4	123.6	24.9
(18,0)	7.09	—	136.3	27.4
(19,0)	7.49	651.1	150.6	30.2
(4,4)	2.73	—	26.6	6.0
(5,5)	3.41	—	37.4	8.3
(6,6)	4.10	—	49.8	11.0
(4,2)	2.09	49.1	18.8	4.2
(5,2)	2.46	—	23.1	5.2

Chapter 9

Room temperature static conductivity

Since the discovery of carbon nanotubes, researchers have alluded to the possibility of their use as current carrying devices. We have seen that in the absence of the strong $\sigma - \pi$ hybridization present in the smallest tubes [58], only the zero-helicity "armchair" tubes have zero electronic band gap [14], the others being small gap semiconductors or insulators depending on their radius and helicity. The transport properties of carbon nanotubes are only beginning to be studied. It has recently been predicted that a bundle of single-walled 7 Å diameter armchair nanotubes separated by the graphite interplanar distance will have a conductivity greater than an equivalent volume of copper at room temperature [90].

We extend these ideas to consider single-wall tubes of any size. Using approximations which relate the electron-phonon matrix elements in tubes and planar graphite sheets, we derive an order-of-magnitude estimate of the resistance of a metallic tube of radius r and length ℓ at room temperature, namely $R \sim (1-5) \times \left(\frac{\ell}{r}\right)$Ohms. The resistance of multi-wall nanotubes could be different, approaching that of the in-plane resistivity of turbostratic graphite.

We first relate the conductivity of carbon nanotubes to the conductivity of a single graphite sheet. Consider σ_{sheet}, the conductivity of a two dimensional graphite sheet, and σ_{tube}, the conductivity of a one dimensional nanotube, where conductivity in dimension D has units of $(conductance)(length)^{2-D}$. From the linearized Boltzmann equation for a homogeneous medium[91]

$$\overleftrightarrow{\sigma} = \frac{2e^2}{(2\pi)^D} \sum_n \int dE \int_{S_k(E)} d^{D-1} S_k \left(-\frac{\partial f}{\partial E}\right) \frac{\mathbf{v}_{n,k}\mathbf{v}_{n,k}}{\left|\frac{\partial E}{\partial \mathbf{k}}\right|} \tau_{n,k} \tag{9.1}$$

where $S_k(E)$ is the k-space surface of constant energy E, f is the Fermi factor, $\mathbf{v}_{n,k}$ is the band velocity of a Bloch state $|n,k\rangle$ and $\tau_{n,k}$ is the scattering time of this state. We consider temperatures small enough so that $\left(-\frac{\partial f}{\partial E}\right)$ can be replaced by $\delta(E-E_F)$. The diagonal components of conductivity in one and two dimensions are

$$\sigma^{1D} = \frac{e^2}{\pi\hbar}\sum_n v_n(E_F)\tau_n(E_F) \tag{9.2}$$

and

$$\sigma^{2D}_{xx} = \frac{e^2}{2\pi^2\hbar}\sum_n \int_{S_k(E_F)} \frac{(\mathbf{v}_{n,k}\cdot\hat{\mathbf{x}})^2}{|\mathbf{v}_{n,k}|}\tau_{n,k}d^1S_k. \tag{9.3}$$

Note that Eq. 9.2 contains no integral over k-space, while Eq. 9.3 has an integral over a one-dimensional k-space surface.

We now estimate σ_{sheet} using Eq. 9.3. The electronic band structure of a single graphite sheet near the Fermi level (around the point "K" of the graphite Brillouin zone) is pictured schematically in Fig. 9.1. The lower cone represents the energies of the occupied π states; the upper cone represents the π^* band. In an undoped sheet E_F corresponds to the point of intersection between the π and π^* cones. For the sake of argument, we assume an arbitrarily small amount of n-type doping to produce the Fermi surface delineated by the dashed curve on the π^* cone[92]. For simplicity, we approximate the Fermi surface as a circle of radius Q with uniform band velocity v_F directed radially outward. We then assume that the scattering times of all these states are equal, obtaining

$$\sigma_{sheet} = \frac{e^2 v_F \tau_{sheet}}{4\pi^2\hbar}(2\pi Q). \tag{9.4}$$

At first sight, this would seem to give the dubious result that σ_{sheet} depends sensitively on the doping and is equal to zero for no doping ($Q=0$). However, the scattering rate for a given state is roughly proportional to the number of final states available for scattering. As Q increases, the density of states at the Fermi level increases so that the

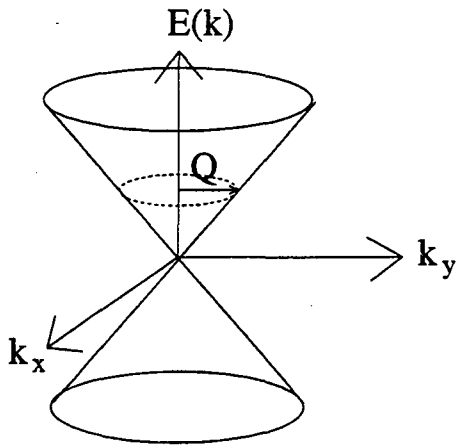

Figure 9.1: (a) Schematic illustration of the graphite sheet bands near the $\pi-\pi^*$ crossing point (the point "K" of the graphite sheet Brillouin zone). The upper and lower cones are the π^* and π bands respectively. For no doping, the Fermi level is at the crossing point. The dotted line marks the Fermi surface for n-type doping.

product $Q\tau_{sheet}$ remains approximately constant. The behavior can best be captured by the relation[93]

$$N_{sheet}(E_F)\tau_{sheet} \approx constant \tag{9.5}$$

where $N_{sheet}(E_F)$ is the number of states per unit energy per unit area at the Fermi level. This is appropriate at high temperatures when the scattering is dominated by phonons. We then rewrite Eq. 9.4 as

$$\sigma_{sheet} = e^2 v_F^2 [N_{sheet}(E_F)\tau_{sheet}], \tag{9.6}$$

an expression obtained by Pietronero et al.[94]. These authors also estimated the scattering time due to electron-phonon scattering at room temperature to obtain $\sigma_{sheet} \sim 4 \times 10^{-2} \frac{1}{\Omega}$. When many sheets are placed in parallel and separated by the Van der Waals distance $d \approx 3.4$Å the resulting 3D in-plane conductivity is $\sim 10^6 \frac{1}{\Omega cm}$ *if hopping between sheets is neglected.* In real undoped graphite, the conductivity is more

than an order of magnitude smaller. The hopping between sheets induces variations in v_F near the K point that result in a smaller v_F for low doping than would be expected from Fig. 9.1 [95]. If bulk graphite is sufficiently doped, the Fermi surface becomes as in Fig. 9.1, and larger conductivities result [96].

The 1D conductivity, σ_{tube}, is now calculated and related to σ_{sheet}. The band structure of single-walled armchair tubes near the Fermi level is shown schematically in Fig. 9.2, the dotted line marking the Fermi level for a small amount of n-type doping[92]. In the absence of the strong hybridization present in extremely small-radius tubes [58], the magnitude of the band velocities for all states is v_F, as for the sheet. Using Eq. 9.2,

$$\sigma_{tube} = \frac{2e^2 v_F \tau_{tube}}{\pi \hbar} \tag{9.7}$$

where the extra factor of 2 comes from the sum over bands crossing E_F. This expression can be rewritten in terms of the density of states of the tube,

$$\sigma_{tube} = 2e^2 v_F^2 [N_{tube}(E_F)\tau_{tube}] \tag{9.8}$$

Unlike the sheet case, $N_{tube}(E_F)$, the number of states per unit energy per unit length, does not depend on the position of the Fermi level in the low-doping limit.

We now relate τ_{tube} to τ_{sheet} by considering the individual scattering processes that determine the scattering times for sheets and tubes. In both cases, scattering is between electronic states at roughly the same energy. The total scattering rate for an initial state $|i\rangle$ is a sum over individual scatterings to each final state. Assuming scattering due to phonons, τ_i of the Boltzmann equation is given by[93],

$$\frac{1}{\tau_i} = \sum_f |\langle f|H_{el-ph}|i\rangle|^2 (1 - cos\theta)\delta(E_f - E_i), \tag{9.9}$$

where θ is the angle between band velocities of states $|i\rangle$ and $|f\rangle$. (We identify $|i\rangle$ and $|f\rangle$ for the tube with the corresponding band-folded states of the sheet[13, 14]). For large enough tubes, it is a good approximation to assume that the electron-phonon matrix

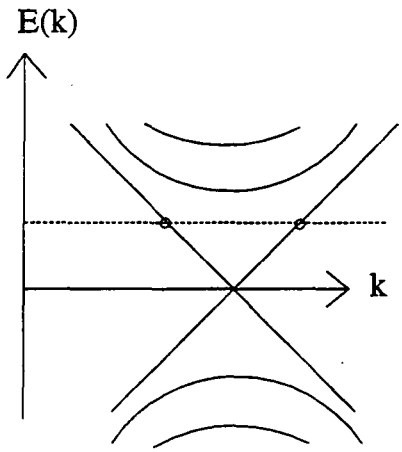

Figure 9.2: Schematic of the band structure of armchair carbon nanotubes near the Fermi level. The bands shown are the band-folded π and π^* bands from Fig. 9.1. The Fermi level for no doping is at the crossing point. The dashed line indicates the Fermi level for n-type doping.

elements are equal for tubes and sheets presuming that the total number of carbon atoms (which enters the matrix element normalization) is the same. This approximation should be accurate for tubes of diameter greater than ~ 10Å as will be discussed in the section on superconductivity. In the general case where the number of atoms is different, we have

$$\frac{\langle f|H_{el-ph}|i\rangle_{tube}}{\langle f|H_{el-ph}|i\rangle_{sheet}} = \frac{\sqrt{n_{sheet}}}{\sqrt{n_{tube}}} \tag{9.10}$$

where n_{sheet} and n_{tube} are the numbers of atoms of the sheet and tube respectively. For the purpose of making order-of-magnitude estimates, we assume that the electron-phonon matrix elements for tubes and sheets have characteristic values M_{tube} and M_{sheet}, such that $M_{tube}\sqrt{n_{tube}} = M_{sheet}\sqrt{n_{sheet}}$, independent of $|i\rangle$ and $|f\rangle$. We obtain

$$\frac{1}{\tau_{tube}} = M_{tube}^2 \sum_f (1 - cos\theta)\delta(E_f - E_i) = M_{tube}^2 \ell N_{tube}(E_F) \tag{9.11}$$

where ℓ is the length of the tube. We also have

$$\frac{1}{\tau_{sheet}} = M_{sheet}^2 \sum_f (1 - cos\theta)\delta(E_f - E_i) = M_{sheet}^2 A N_{sheet}(E_F) \tag{9.12}$$

where A is the area of the sheet. In both cases the angular factors average to 1. Using Eqs. 9.6, 9.8, 9.11, and 9.12 along with the relation

$$\frac{M_{sheet}^2}{M_{tube}^2} = \frac{n_{tube}}{n_{sheet}} = \frac{2\pi r \ell}{A} \tag{9.13}$$

we obtain

$$\sigma_{tube} = 4\pi r \sigma_{sheet} = 2 \cdot (2\pi r \sigma_{sheet}) \tag{9.14}$$

Thus, the above assumptions regarding the electron-phonon matrix elements for sheets and tubes imply that an armchair nanotube has twice the conductance of an infinite graphite sheet per $2\pi r$ of width. The factor of two arises from the Fermi surface average of the x-component of the Fermi velocity. For an armchair tube with a single partially filled band the average of the squared x-component of the Fermi velocity is simply $\langle v_x^2 \rangle = v_F^2$, whereas for a graphite sheet with a circular Fermi surface $\langle v_x^2 \rangle = \frac{1}{2} v_F^2$. For sufficiently large tubes, the Fermi level crosses many bands of differing Fermi velocities (assuming a small amount of doping). The resulting average Fermi velocity approaches that of $\langle v_x^2 \rangle$ for doped graphite. Alternatively, we may consider continuously changing the Fermi level for a tube of fixed radius. As each new band crosses E_F, the density of states will peak, yielding a steplike dependence for σ_{tube} as a function of doping which tends to the graphite sheet value[97]. It must be pointed out that the relation of Eq. 9.14 is only approximate; the true θ-dependence of $\langle f|H_{el-ph}|i\rangle$ may introduce factors of order unity into the expressions for the scattering times.

A system with 1D conductivity σ has a resistance per length of $\frac{1}{\sigma}$. Using Eq. 9.14 and the previously estimated value of σ_{sheet}, we obtain an order-of-magnitude estimate of the resistance of an armchair carbon nanotube of radius r and length ℓ at room

temperature:

$$(1-5)\times\left(\frac{\ell}{r}\right)\Omega \tag{9.15}$$

Typical experimental parameters of $r\sim 10-100\text{Å}$ and $\ell\sim 1-10\mu m$ yield $10^2-10^5\Omega$. In small-gap non-armchair nanotubes, the π and π^* bands have an avoided crossing at the Fermi level for the undoped case[14]. If they are sufficiently doped (or if k_BT is much larger than the gap), their resistance will be the same as above. For a parallel array of noninteracting single-wall nanotubes, the 3D conductivity will be determined by the resistance of the individual tubes, and the packing-fraction of tubes within the array. For tubes packed in a 2D hexagonal arrangement at the graphite interplanar distance, the conductivity along the tube axes will be comparable to, or greater than that of copper if $r\sim 2-10\text{Å}$ [90] *provided that the change in the Fermi surface due to inter-tube hopping is negligible.* As was the case for bulk graphite as compared to noninteracting single sheets, the conductivity of an array of nanotubes at the equilibrium intertube distance may be smaller than that of a theoretical array of noninteracting tubes. The difference should be exacerbated for large single-walled tubes which are expected to deform in a manner which increases the contact area between tubes[98].

The resistance of multi-wall tubes is a complicated issue. The electronic properties of bulk graphite are strongly affected by the inter-sheet electron hopping [95], in particular the introduction of c-axis dispersion and the flattening of the π and π^* bands near the K point. It has been predicted that similar band flattening occurs for multi-wall carbon nanotubes [74]. The static in-plane conductivity at 300 K of undoped ABAB-stacking graphite is $\sim 2.6\times 10^4\frac{1}{\Omega cm}$ [99], more than an order of magnitude lower than the "independent parallel sheet" result. Thus, we expect the conductivity of multi-wall tubes to be considerably below that of the sum of the constituent tubes. For large radius multi-wall tubes, the situation is probably most analogous to turbostratic graphite in which the parallel sheets are orientationally disordered [100].

We have explored the room-temperature static conductivity of carbon nanotubes by relating the properties of tubes to those of a graphite sheet. The character of the electronic states, gross features of the phonon spectra and overall magnitude of electron-phonon coupling are similar in tubes and sheets. This implies that single-wall carbon nanotubes are excellent conductors, with a collection of non-interacting armchair tubes conducting current roughly as well as a graphite sheet of equal length and area. We expect multi-wall tubes to have a reduced conductivity due to changes in the band structure analogous to those which occur in turbostratic graphite.

Chapter 10

Quantum conductance of nanotubes with defects

In chapter 6, we saw that the introduction of topological defects can change the chirality of nanotubes. In fact, it is possible to join two perfect nanotubes (n, m) and $(n \pm d, m \mp d)$ by forming d pentagon-heptagon pairs in the interface between them [59]. The resulting carbon nanotube heterojunction, $(n, m)/(n \pm d, m \mp d)$, can have a different electronic structure on each side of the interface. The heterostructures formed by joining nanotubes of different chirality may show unique quasi-one-dimensional transport properties.

There are theoretical and experimental studies on the quantum transport properties of carbon nanotubes in the literature. On the experimental side, the conductance of nanotube bundles has been measured [101], and a measurement of the conductance of an isolated multiwalled carbon nanotube has been recently reported [102]. From the theoretical viewpoint, there are studies on the effect of magnetic fields and voltage bias in the ballistic conductance of perfect nanotubes[103] using the Landauer approach [104], but there have been no studies of changes in the conductance produced by defects. We address this issue by calculating the conductance of metallic carbon nanotubes with defects using the Landauer formula[104] in a tight-binding scheme. Within the Landauer formalism, the ballistic conductance of perfect systems is proportional to the number of conducting channels at the Fermi energy, that is, the number of bands at this energy [105]. The conductance of an imperfect system is lowered due to reflection of the electron waves off the defects. We first study the simplest possible defect, a single vacancy, and calculate the conductance as a function of tube radius. The increase of conductance with radius illustrates the crossover from one-dimensional to two-dimensional behavior. We

then calculate the conductance through nanotube heterojunctions, $(n_1, m_1)/(n_2, m_2)$, where both (n_1, m_1) and (n_2, m_2) tubes are metallic. We show that certain configurations of pentagon-heptagon pair defects completely stop the flow of electrons, while others permit the transmission of current through the interface. Such systems may be used as nanoscale electrical switches.

10.1 Model and Method

We are interested in studying infinitely long carbon nanotubes with localized defects. First we consider the problem of a vacancy in an otherwise perfect tube. We also study nanotubes with pentagon-heptagon pairs, which can be viewed as the result of matching two perfect semi-infinite tubes with different chiralities. This kind of problem is most conveniently treated with the Green function matching (GFM) method[61]. A nanotube with pentagon-heptagon pairs is depicted schematically in Fig. 10.1. The perfect tubes are media A and B. The last unit cell of medium A, labeled -1, together with the first of medium B, labeled 1, constitute the interface domain. We describe the carbon nanotubes by a tight-binding model with one π-electron per atom. Our tight-binding Hamiltonian is of the form

$$H = -V_{pp\pi} \sum_{\langle ij \rangle} a_i^\dagger a_j + c.c. \tag{10.1}$$

where the sum in i, j is restricted to nearest-neighbor atoms, and $V_{pp\pi} = 2.66$ eV, as in Ref. [106]. On-site energies are set to zero. All the hopping parameters are equal, independent of the bond length, curvature or any rearrangement due to the presence of defects. Therefore, our results show the changes induced solely by the alterations in the topology of the hexagonal rolled lattice. A vacancy is simulated by setting the hoppings to zero around the vacant site and its on-site energy equal to a large value, so the impurity peak does not appear in the energy range for which the density of states (DOS) of the tube is non-zero. We now describe the salient features of the GFM, and

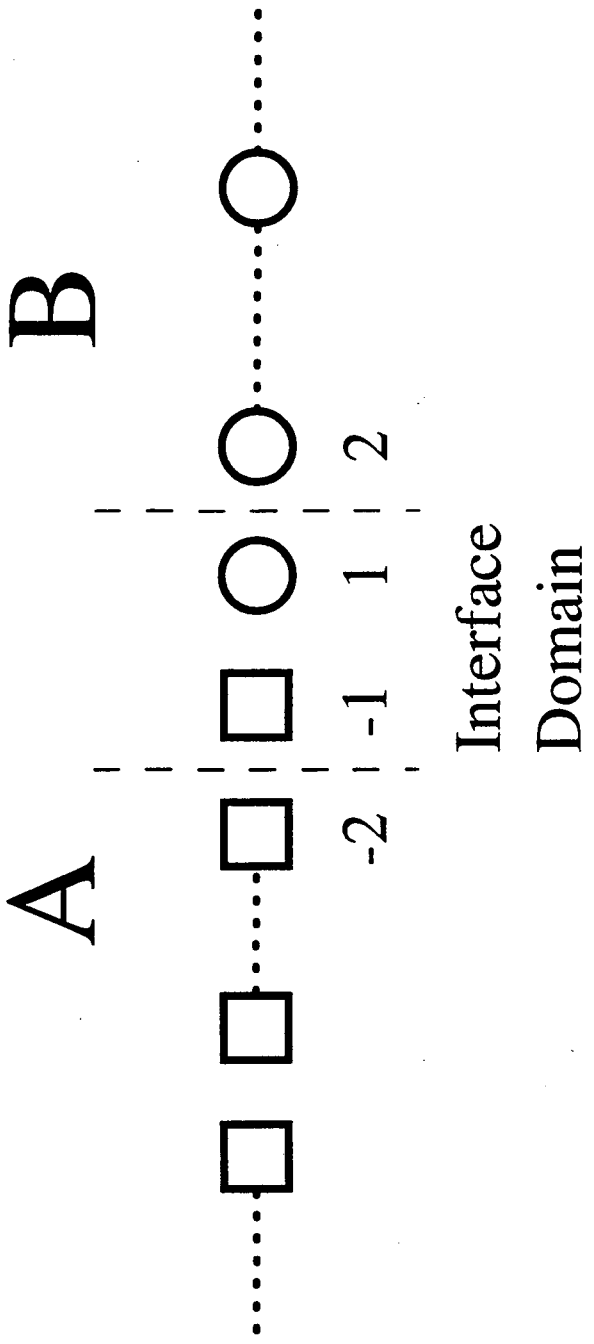

Figure 10.1: Schematic view of a matched $A|B$ system.

show how it is applied to calculate the conductance.

In the GFM method, the single-particle Green function of the tube with pentagon-heptagon pairs, G, is calculated from the bulk Green functions and Hamiltonians of the perfect, defect-free systems, G_A, G_B, H_A, and H_B respectively, and the coupling interaction between media A and B. This method can be used with different one-electron Hamiltonian models [61]. Within the tight-binding model we employ, the Hamiltonians and the Green functions are matrices whose dimensions are $(N_c \cdot N_e) \times (N_c \cdot N_e)$, where N_c is the number of unit cells and N_e is the number of π-electrons/cell. Since we are studying infinite systems, in principle these matrices are infinite. An element of G would be denoted by $\langle i, \alpha | G | j, \alpha' \rangle$, where i, j are cell indices and α, α' denote orbitals. In what follows, we let $H_{M\,i,j}$ denote the *block* of the Hamiltonian matrix of the perfect system M ($M = A, B$) which contains matrix elements of H_M between localized π-electron orbitals in cell i and orbitals in cell j. Thus, $H_{M\,i,j}$ is itself a matrix of dimension $N_{M\,e} \times N_{M\,e}$ (similarly for $G_{M\,i,j}$). Using the GFM we will only have to deal with block matrices whose dimensions are at most $(N_{A\,e} + N_{B\,e}) \times (N_{A\,e} + N_{B\,e})$, $N_{A\,e}$ and $N_{B\,e}$ being the number of orbitals per cell in materials A and B respectively.

The coupling between media A and B is given by the block matrices $H_{I\,-1,1}$ and $H_{I\,1,-1}$. $H_{I\,-1,1}$ contains matrix elements between orbitals in cells -1 and 1. Obviously $H_{I\,1,-1} = H^{\dagger}_{I\,-1,1}$. The dimension of $H_{I\,-1,1}$ is $N_{A\,e} \times N_{B\,e}$, so in general it is a rectangular matrix.

From G we can evaluate the local density of states $N_n(E)$ at any energy E and nth cell of the system,

$$N_n(E) = -\frac{1}{\pi} \mathrm{Im\ tr}\ G_{n,n}(E), \tag{10.2}$$

where the trace is over the N_e orbitals in cell n.

The total Green function, G, is calculated in the following way: Suppose that in our matched system, $A|B$, we have an incident amplitude from side A, and we want to know

the amplitude produced by the scattering at the interface. That is, given an excitation in cell n of medium A propagating toward the interface, we are interested in knowing the amplitude produced in cell n' of medium B (transmission) or medium A (reflection).

In the first case, i.e., for transmission amplitudes, we have that

$$G_{n,n'} = G_{B\,n,1}\,\mathcal{G}_B^{-1}\mathcal{G}\mathcal{G}_A^{-1}\,G_{A\,-1,n'}, \tag{10.3}$$

where calligraphic letters indicate interface objects, e.g., $\mathcal{G}$ is the Green function of the system projected onto the interface domain. For reflected amplitudes we have

$$G_{n,n'} = G_{M\,n,n'} + G_{M\,n,-1}\,\mathcal{G}_M^{-1}(\mathcal{G}-\mathcal{G}_M)\mathcal{G}_M^{-1}\,G_{M\,-1,n'}, \tag{10.4}$$

where we have written the Green function separating the incident and reflected part; the second term in Eq. (10.4) accounts for reflection at the interface. This will be useful for deriving an expression for the scattering matrix within the Green function scheme.

For computational purposes it is convenient to introduce the transfer matrices of medium M, T_M, S_M, $\overline{T}_M$, $\overline{S}_M$ [61], as

$$G_{M\,n+1,m} = T_M G_{M\,n,m}, \quad (n \geq m) \tag{10.5}$$

$$G_{M\,n-1,m} = \overline{T}_M G_{M\,n,m}, \quad (n \leq m) \tag{10.6}$$

$$G_{M\,n,m+1} = G_{M\,n,m} S_M, \quad (m \geq n) \tag{10.7}$$

$$G_{M\,n,m-1} = G_{M\,n,m}\overline{S}_M, \quad (m \leq n)\,. \tag{10.8}$$

We compute the transfer matrices using the algorithm of López-Sancho *et al.* [107]. From Eqns. (10.5-10.8) it is easily seen that

$$\overline{S}_M = \mathcal{G}_M^{-1} T_M \mathcal{G}_M \tag{10.9}$$

$$S_M = \mathcal{G}_M^{-1}\overline{T}_M\mathcal{G}_M, \tag{10.10}$$

so we only need to calculate two of the four transfer matrices defined above. Nevertheless, we maintain all four to yield more compact expressions. Using the former definitions, it can be shown that [61]

$$\mathcal{G} \equiv \begin{pmatrix} \mathcal{G}_{BB} & \mathcal{G}_{BA} \\ \mathcal{G}_{AB} & \mathcal{G}_{AA} \end{pmatrix} = \begin{pmatrix} E - H_{B\,1,1} - H_{B\,1,2}T_B & H_{I\,1,-1} \\ H_{I\,-1,1} & E - H_{A\,-1,-1} - H_{A\,-1,-2}T_A \end{pmatrix}^{-1}. \tag{10.11}$$

The full Green function matrix, G, can then be constructed from Eqs. 10.3 and 10.4.

In the Landauer formalism, the conductance of a system is related to its scattering properties[104], which are described using the Green function scheme presented in the previous subsection. The multi-channel generalization of the Landauer conductance formula is [105]:

$$\Gamma = \frac{2e^2}{h}\mathrm{Tr}(t^\dagger t) = \frac{2e^2}{h}\sum_{\beta\alpha}|t_{\beta\alpha}|^2, \tag{10.12}$$

where t is the transmission matrix from either the left or the right as defined by Fisher and Lee. Let us choose transmission from left to right, i.e., from medium A to B. Suppose that at the energy E there are M_A channels in medium A and M_B channels in medium B. Then t is a rectangular $M_B \times M_A$ matrix. The squared modulus of a component of t, $|t_{\beta\alpha}|^2$, is the transmission coefficient from channel α in medium A to channel β in medium B. If we have an incident eigenstate from medium A, φ_α, the corresponding transmitted amplitude in side B, $\psi_{\alpha\,sc}$, can be written as a linear combination of the eigenstates of medium B, φ_β, provided that we are far from the interface. So $|t_{\beta\alpha}|^2 = \frac{v_\beta}{v_\alpha}|\langle\varphi_\beta|\psi_{\alpha\,sc}\rangle|^2$, where v_β, v_α are the group velocities of the corresponding eigenstates.

The scattered wave, $\psi_{\alpha\,sc}$, is calculated from the scattering matrix, $S(E)$, which is defined by

$$\begin{pmatrix} \Psi_{B,out} \\ \Psi_{A,out} \end{pmatrix} = S(E) \begin{pmatrix} \Psi_{B,in} \\ \Psi_{A,in} \end{pmatrix}, \tag{10.13}$$

where Ψ_{in}, Ψ_{out} denote the ingoing and outgoing wavefunction amplitudes respectively. The transmitted amplitude is obtained by setting Ψ_{in} equal to an incident eigenstate. Using the relation between the wavefunction amplitudes and the Green function [61],

we can write the scattering matrix in terms of $\mathcal{G}$: For example, the reflected amplitude in medium B is

$$\Psi_n = \varphi_{B\,n} + G_{B\,n,1}\mathcal{G}_B^{-1}(\mathcal{G}_{BB} - \mathcal{G}_B)\mathcal{G}_B^{-1}G_{B\,1,n'}G^{-1}_{B\,n',n'}\varphi_{B\,n'}, \tag{10.14}$$

where φ_B is an incident eigenstate in medium B. Similarly, for the amplitude transmitted from side A to B,

$$\Psi_n = G_{B\,n,1}\mathcal{G}_B^{-1}\mathcal{G}_{BA}\mathcal{G}_A^{-1}G_{A\,-1,n'}G^{-1}_{A\,n',n'}\varphi_{A\,n'}, \tag{10.15}$$

and so on. Using (5-8) we can write the scattering matrix $S(E)$ as

$$\begin{aligned} S(E) \equiv & \begin{pmatrix} S_{BB} & S_{BA} \\ S_{AB} & S_{AA} \end{pmatrix} = \\ & \begin{pmatrix} T_B^{n'} & 0 \\ 0 & \overline{T}_A^{n} \end{pmatrix} \begin{pmatrix} \mathcal{G}_{BB} - \mathcal{G}_B & \mathcal{G}_{BA} \\ \mathcal{G}_{AB} & \mathcal{G}_{AA} - \mathcal{G}_A \end{pmatrix} \begin{pmatrix} S_B^{n'} & 0 \\ 0 & \overline{S}_A^{n} \end{pmatrix} \times \\ & \begin{pmatrix} G^{-1}_{B\,n',n'} & 0 \\ 0 & G^{-1}_{A\,n,n} \end{pmatrix}. \end{aligned} \tag{10.16}$$

If we take n, n' far from the interface, we can choose the incident amplitudes as eigenstates of the unperturbed Hamiltonian H_A, and decompose the scattered wavefunctions in terms of the eigenstates of the unperturbed Hamiltonian H_B. Thus, in terms of the scattering matrix, equation (10.12) reads

$$\Gamma(E) = \frac{2e^2}{h}\sum_{\alpha\beta}\left(\frac{v_\alpha}{v_\beta}\right)|\langle\varphi_\beta|S_{BA}(E)|\varphi_\alpha\rangle|^2 \tag{10.17}$$

where the indices α, β run over all eigenstates with energy E of media A and B respectively.

10.2 Carbon nanotubes with vacancies

In this section we study the conductance of several (n, n) carbon nanotubes in which an atom has been removed to produce a vacancy. In Fig. 10.2 we plot the conductance

of the $(4,4)$ nanotube with one vacancy (full line) and the perfect $(4,4)$ tube (dashed line) as a function of the energy. For most energies, and particularly at the Fermi energy of the undoped system ($E = 0$), the value of the conductance is reduced by almost one unit, $\frac{2e^2}{h}$, when the impurity is present. This amounts to the removal of one conducting channel, and for the undoped case, a reduction of 50 % with respect to the conductance of the perfect $(4,4)$ nanotube. This is to be expected, for the presence of a vacancy in a monatomic chain completely suppresses the conductance by removing the only existing channel. Since a nanotube is a *quasi*-one-dimensional system, the conductance is not totally suppressed; the extent to which it is depleted reflects the dimensionality of the system.

Fig.10.3 shows the difference between the conductance (for $E_F = 0$) of a perfect (n,n) tube and that of the same tube with a vacancy as a function of n. The circumference of an (n,n) tube is given by $C = 3nl$, where l is the carbon-carbon nearest-neighbor distance, so this is equivalent to plotting the change in conductance versus nanotube radius. All perfect (n,n) tubes have two bands at E_F, giving rise to a conductance of $4\frac{e^2}{h}$. When the impurity is introduced, the conductance decreases, this decrease being greater for the smaller tubes. Note that for the (4,4) tube the conductance is reduced by one channel, and this difference diminishes smoothly when the radius increases. An increase in radius corresponds to a change from quasi-one-dimensional to two-dimensional behavior. In a perfect two-dimensional graphite sheet the change in conductance due to the presence of a single vacancy is negligible.

10.3 Pentagon-heptagon matched tubes: Nanotube heterojunctions

We now come to the main focus of this chapter, the conductance of matched metallic carbon tubes with pentagon-heptagon pair defects. First we study the (12,0)/(6,6) tube. There is a unique way to match these two tubes by joining their perfect unit cells, which

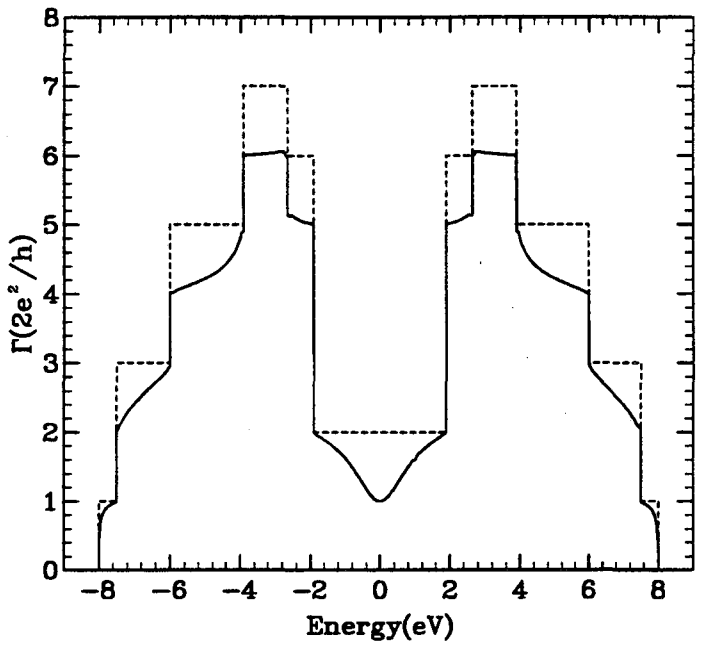

Figure 10.2: Conductance of a (4,4) nanotube with a vacancy (full line) and a perfect (4,4) nanotube (dashed line) as a function of the Fermi energy.

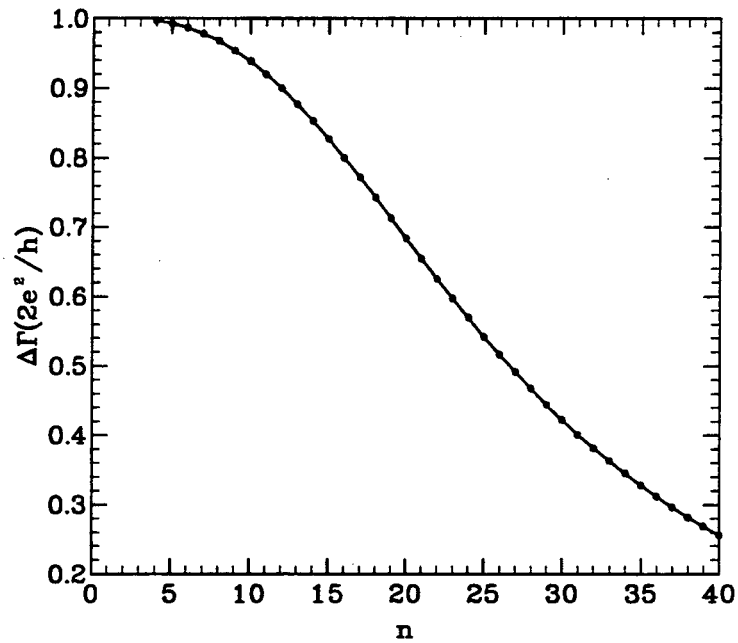

Figure 10.3: Difference in the conductance of an (n, n) nanotube with and without a vacancy as a function of n.

produces a ring of six pentagon-heptagon pairs around the circumference. In Fig. 10.4 (top) we show the conductance of the matched tube together with the conductances of the (12,0) and (6,6) perfect tubes as a function of energy. We see that, whereas the perfect tubes are metallic and have non-zero conductance at the Fermi energy of the undoped tube ($E_F = 0$), there is a gap in the conductance for the matched system. The conductance of the matched tube is always smaller than the conductance of the perfect tubes that form it, as expected: any defect degrades the conductance, and in a matched system $A|B$ medium B can be considered as a perturbation to medium A and viceversa. This effect is similar to what Todorov *et al.* [108] noted studying the conductance of wires with width fluctuations. In Figs. 10.4 (center) and 10.4 (bottom) we present the local density of states (LDOS) of the unit cells which contain the pentagon-heptagon pairs (full lines)[109]. In our notation these are cells with $n = -1$ (for the (12,0) tube, Fig. 10.4, center) and $n = 1$ (for the (6,6) tube, Fig. 10.4, bottom). For comparison we also plot the LDOS of the perfect tubes (dotted line in Fig. 10.4 (center) and dashed line in Fig. 10.4 (bottom) respectively). The LDOS is non-zero in the defect region for the energy interval in which the conductance is zero, as it is for the perfect tubes. Therefore the conductance is not suppressed due to the appearance of a gap in the LDOS in the defect region. This points to a symmetry origin of the suppression of the conductance in this system. We discuss this at length in the following section. One may wonder whether the presence of a full ring of pentagon-heptagon pairs around the circumference of the tube could be related to this effect.

To clarify this point we have studied a tube for which the matching is achieved by a mixture of hexagons and pentagon-heptagon pairs, the (9,0)/(6,3) tube. In this case three pentagon-heptagon pairs are needed, so the matching region contains three hexagons as well. There are several inequivalent ways of joining the perfect unit cells: all the hexagons adjacent to each other, only two of the hexagons adjacent, and all the hexagons separated. Here we study two of these possible matching orientations: 1)

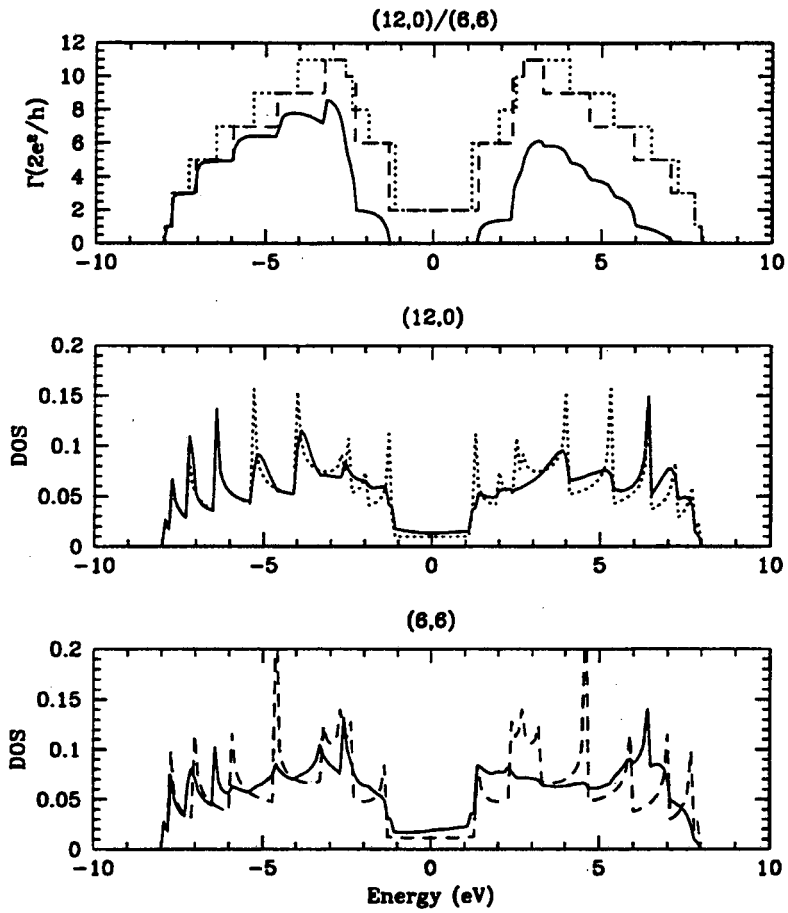

Figure 10.4: Results for the (12,0)/(6,6) matched tube. Top: conductances of the matched system (solid line), perfect (12,0) tube (dashed line), and perfect (6,6) tube (dotted line). Center: atom-averaged LDOS of the interface unit cell of the (12,0) tube (full line) and the perfect (12,0) tube (dotted line), plotted for comparison. Bottom: atom-averaged LDOS of the interface unit cell of the (6,6) tube (full line) and the perfect (6,6) tube (dashed line), plotted for comparison.

symmetric: all the hexagons separated by defects, and 2) asymmetric: two hexagons adjacent to each other. The first is so-named because the sequence of n-fold atom rings around the circumference (6-7-5-6-7-5-6-7-5) has three-fold rotational symmetry about the cylindrical axis of the tube. The asymmetric case has no rotational symmetry (sequence of n-fold rings is 6-7-5-6-6-7-5-7-5).

In Fig. 10.5 we present the results for the $(9,0)/(6,3)$ symmetric tube. Fig. 10.5 (top) shows the conductance along with the conductance of its perfect components, i.e. the $(9,0)$ (dashed line) and the $(6,3)$ (dotted line). Again we find that there is a gap in the conductance around the Fermi energy of the undoped system, so the appearance of a conductance gap is not exclusive to tubes with a full circumference of pentagon-heptagon pairs. As before, the conductance of the matched tube is lower at every energy than that of its perfect constituents. In Figs. 10.5 (center) and 10.5 (bottom) we show the LDOS of the matched unit cells which form the interface (full lines) along with the LDOS of the corresponding perfect $(9,0)$ and $(6,3)$ tubes (dashed and dotted lines, respectively). Again the LDOS is non-zero in the energy interval in which the conductance is zero.

The results for the asymmetric $(9,0)/(6,3)$ tube are shown in Fig. 10.6. For this tube we find that there is not a total suppression of the conductance at any energy at which the LDOS is non-zero (Fig. 10.6, top, full line): the matched system behaves as a metal. Nevertheless, since the interface between the tubes acts as a defect, the conductance is reduced by approximately one channel relative to that of the perfect tubes. As in the previous cases, we plot the conductances of the (9,0) and (6,3) perfect tubes for comparison. The LDOS at the interface (Figs. 10.6, center and bottom, full lines) is practically equal to the one found for the symmetric case (see Fig. 10.5). The rest of the features are very similar to the symmetric case. The metallic nature of the asymmetric $(9,0)/(6,3)$ tube provides further evidence that the presence of a conductance gap is related to the symmetry of the defects at the interface. In what follows, we explain this effect and derive general rules that predict the occurence of conductance gaps in

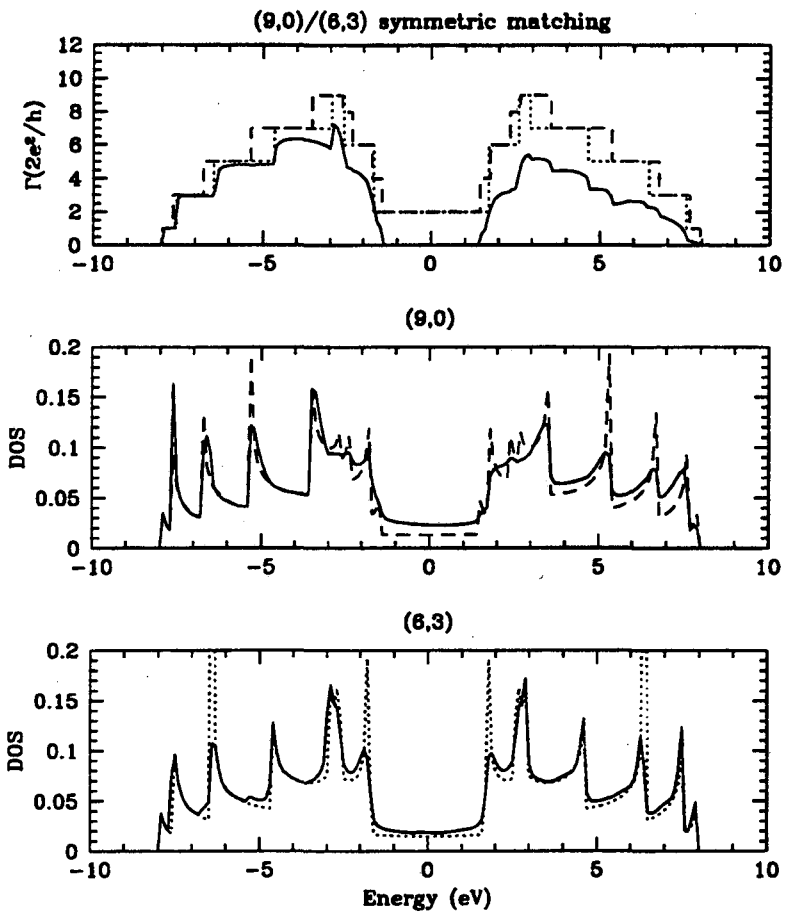

Figure 10.5: Results for the (9,0)/(6,3) symmetric matched tube. Top: conductances of the matched system (solid line), perfect (6,3) tube (dotted line), and perfect (9,0) tube (dashed line). Center: atom-averaged LDOS of the interface unit cell of the (9,0) tube (full line) and the perfect (9,0) tube (dashed line), plotted for comparison. Bottom: atom-averaged LDOS of the interface unit cell of the (6,3) tube (full line) and the perfect (6,3) tube (dotted line), plotted for comparison.

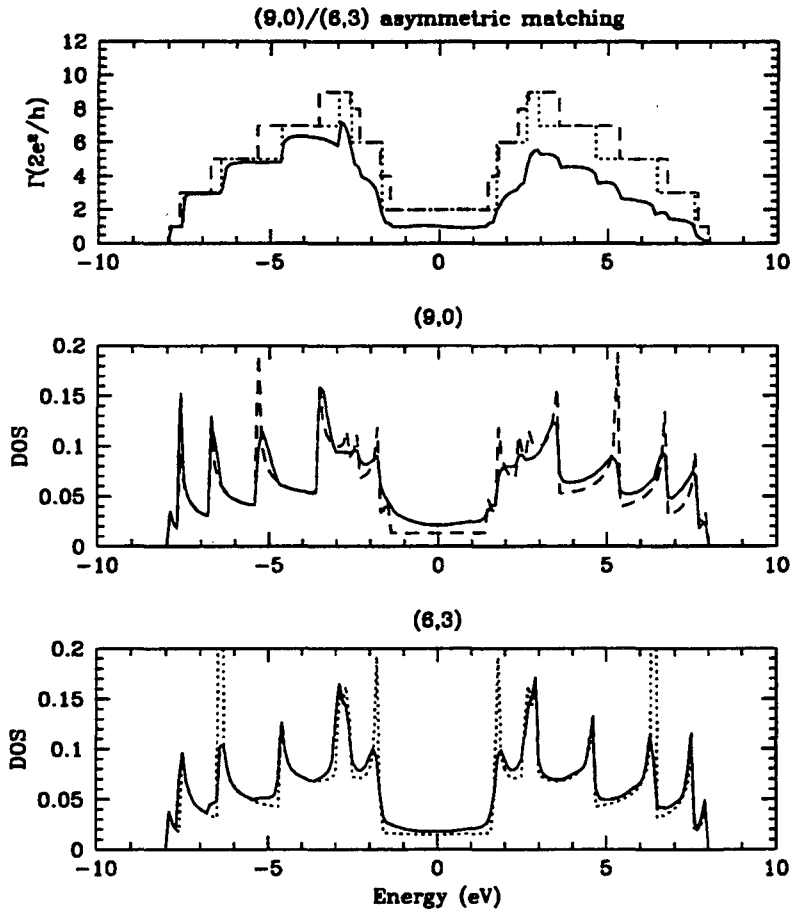

Figure 10.6: Results for the (9,0)/(6,3) asymmetric matched tube. Top: conductances of the matched system (solid line), perfect (6,3) tube (dotted line), and perfect (9,0) tube (dashed line). Center: atom-averaged LDOS of the interface unit cell of the (9,0) tube (full line) and the perfect (9,0) tube (dashed line), plotted for comparison. Bottom: atom-averaged LDOS of the interface unit cell of the (6,3) tube (full line) and the perfect (6,3) tube (dotted line), plotted for comparison.

$(n_1, m_1)/(n_2, m_2)$ systems.

10.4 Discussion

We first explain the conductance gap in the $(12,0)/(6,6)$ tube. A discussion of the $(9,0)/(6,3)$ system and the general rules for all $(n_1, m_1)/(n_2, m_2)$ tubes follow. If curvature-induced hybridization is neglected[58], carbon nanotubes can be thought of as graphite sheets with periodic boundary conditions applied in the circumferential direction. This results in a quantization of allowed **k**-vectors of the graphite sheet which forms the tube. Fig. 10.7 shows the lines of allowed **k**-vectors overlayed on the graphite sheet first Brillouin zone (BZ) for the perfect $(6,6)$ and $(12,0)$ tubes. Both tubes have six-fold rotational symmetry about their cylindrical axes. Thus, electronic states of the tubes may be classified according to discrete angular momenta L[110]. States that arise from different lines of allowed **k**-vectors have different rotational symmetries. The lines which intersect $\mathbf{k} = 0$ give rise to rotationally invariant (L=0) tube states. Other lines give rise to states of higher L.

The states with energies near E_F (for the undoped case) are those with **k**-vectors close to the vertices of the hexagonal BZ. This is because the Fermi surface of the undoped graphite sheet is located at these points. Thus, the states at E_F for the $(6,6)$ tube originate from the center line, and are $L = 0$ states, invariant under rotations by $\frac{2\pi}{6}$ about the tube axis. The Fermi level states of the $(12,0)$ tube come from the fourth lines away from the center, and are $L = 2$ states (defined with respect to six-fold rotational symmetry). So we see that the Fermi level states of the two perfect tubes have *different rotational symmetries*.

When the two tubes are matched to form the junction, $(12,0)/(6,6)$, six pentagon-heptagon pairs are introduced at the interface. The interface itself has six-fold rotational symmetry. Therefore, the matched tube is invariant under rotations by $\frac{2\pi}{6}$. Now consider

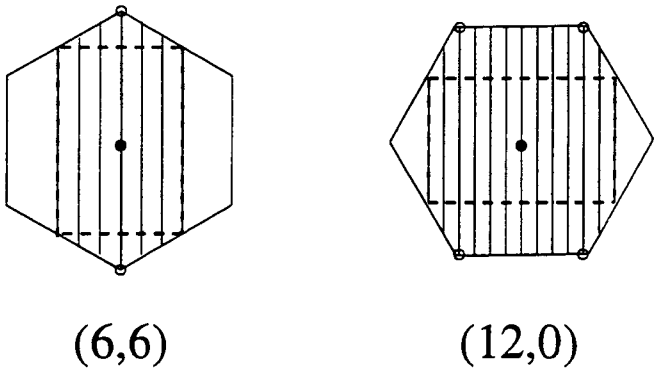

Figure 10.7: Lines of allowed **k**-vectors of the (6,6) and (12,0) carbon nanotubes overlayed on the graphite sheet Brillouin zone. Dashed lines enclose Brillouin zones of the $(1,1)$ and $(1,0)$ units. Solid dots indicate $\mathbf{k} = 0$, and open dots mark points where the lines touch the graphite sheet Fermi surface.

the conduction process. Scattering due to rigid defects is elastic as long as the defects have no internal excitations. Thus, an electron which begins in the $(12,0)$ tube must scatter to a state with the same energy in the $(6,6)$ tube. But since the states at E_F of the two half-tubes have different L, the electron wave is *totally reflected*, and the conductance equals zero. Stated another way, the perfectly symmetric interface cannot impart any extra angular momentum to the electron, so the conditions of energy and angular momentum conservation cannot be satisfied simultaneously[111]. If the system is doped with either electrons or holes, such that E_F is pushed away from 0 to energies at which states of equal L coexist on both halves of the junction, the conductance is nonzero. The conductance gap marks the energy window in which states of the two sides have no L-values in common.

It should be pointed out that the $L = 0$ states of the $(6,6)$ side of the junction do extend into the $(12,0)$ side, but they decay away from the interface, as is typical of interface states. Likewise, the $L = 2$ states of the $(12,0)$ side extend into the $(6,0)$ side,

but are damped. Since evanescent waves carry no current, the resulting conductance is zero. This is similar to total reflection in wave optics: even when the reflectance equals unity, some nonzero amplitude penetrates. However, far from the reflecting surface (on the opposite side from the source), no light flux is measured.

The above arguments may also be applied to the $(9,0)/(6,3)$ system. Consider the symmetric matching case. The interface (6-7-5-6-7-5-6-7-5) has three-fold rotational symmetry about the tube axis, as do the individual $(9,0)$ and $(6,3)$ tubes. From the graphite sheet band-folding analysis, it can be shown that the states at E_F for the $(6,3)$ tube have $L = 1$ (defined with respect to three-fold rotational symmetry). The Fermi level states of the $(9,0)$ tube have $L = 0$. Again, states on opposite sides of the interface have different rotational symmetries. The symmetric interface does not impart extra angular momentum to the conducting electrons, so there is a conductance gap near $E_F = 0$.

Now consider the asymmetric matching case. The interface (6-7-5-6-6-7-5-7-5) has *no* rotational symmetry whatsoever, and in particular, it lacks three-fold symmetry. Therefore, transitions between the $L = 1$ states of the $(6,3)$ side, and the $L = 0$ states of the $(9,0)$ side are permitted; the interface can impart angular momentum to the electron. This results in a conductance which is nonzero over the whole energy range where the DOS is nonzero.

A general rule can now be abstracted: Carbon nanotube heterojunctions may have conductance gaps if the defects that form the interface are arranged symmetrically. They will not have conductance gaps if the interface does not preserve the rotational symmetry of the two constituent tubes. Of course, it is possible to match two tubes with different rotational symmetries[112]. In this case, no symmetric matching is possible, and conductance gaps will never appear. It is also possible for symmetrically matched tubes to avoid having a conductance gap. This will happen when the states of the two sides have some L-values in common at every energy.

We can easily derive the necessary condition on n_1, m_1, n_2, and m_2 such that the $(n_1, m_1)/(n_2, m_2)$ matched tube is a candidate for a conductance gap: An (n, m) tube has J-fold rotational symmetry if n and m are both divisible by J. Thus, if n_1, m_1, n_2, and m_2 all have a common divisor, it will be possible to form the $(n_1, m_1)/(n_2, m_2)$ junction with a rotationally symmetric interface. A conductance gap may result. Otherwise the conductance will, in general, be nonzero in the energy range for which the DOS is nonzero. Note that even if the two constituent tubes share a common rotational symmetry, it is usually possible to choose an asymmetric matching (see the asymmetric $(9, 0)/(6, 3)$ above). A conductance gap can then be avoided (it cannot be avoided in the $(12, 0)/(6, 6)$ system with ideal unit cell matching). It should be mentioned that the above argument holds for all types of defects at the interface. Only the symmetry of the interface is relevant.

One point of interest is the variation in geometrical structure of carbon nanotube heterojunctions with different matching configurations. Nanotubes with pentagon-heptagon pair defects may exibit localized kinks and bends. Bend angles of up to 15 degrees have been predicted[59, 106], and tubes with these signatures have been seen experimentally[59]. A nanotube heterojunction with a bend is the result of an asymmetric matching at the interface; rotational invariance is destroyed. If two tubes are matched symmetrically, the junction will have no bend, for the axis of rotational symmetry is preserved. Thus, there is a relationship between the geometry of nanotube heterojunctions and the appearance of conductance gaps. Bent junctions will, in general, have nonzero conductance if the constituent tubes are metallic. Straight junctions may have conductance gaps. So we have the somewhat counterintuitive result that bent junctions conduct better than straight junctions on average.

The presence of conductance gaps in some carbon nanotube heterojunctions opens up new possibilities for their potential applications. Since conductance gaps arise from rotational symmetry, any perturbation which destroys this symmetry will allow the

tube to conduct. Three sources of symmetry-breaking are thermally excited phonons, externally applied electromagnetic (EM) radiation, and mechanical deformation. If a nanotube heterojunction with a conductance gap is at very low temperature, only acoustic phonon modes with $\mathbf{q} \sim 0$ will be excited. From the above band-folding analysis, these modes will be symmetric ($L = 0$), and will not change the rotational symmetry of the interface. If the junction is at slightly higher temperature, asymmetric phonon modes ($L > 0$) will be excited which break the rotational symmetry, and destroy the conductance gap. The conductance should then show a sharp increase as temperature is increased. Therefore, heterojunctions with conductance gaps may be used as nanoscale thermistors which operate in the 10-100 K range. Heterojunctions kept at low temperature may loose their conductance gaps when bathed with appropriately polarized EM radiation. Circularly polarized photons with **E**-fields rotating about the tube axis can impart angular momentum to the conduction electrons. This allows the electrons to cross the interface and conduct current. Thus, these systems could also be used as nanoscale photoconductive switches which operate over a wide range of frequencies (unlike typical photoconductive materials, it is the exchange of angular momentum rather than energy that excites the electrons into conducting states). Finally, mechanical stress can be used to destroy the rotational symmetry of a junction. If a nanotube heterojunction is anchored at both ends, a nanoscale piezoelectric particle positioned along side the interface may deform the tube wall enough to allow the flow of current. In this way, heterojunctions could be used as nanoscale voltage-activated electrical switches.

10.5 Conclusion

We have studied the conductance of metallic carbon nanotubes with defects using the Landauer approach and a tight-binding Green function technique. We find that a single vacancy produces a dramatic decrease in the conductance of small-radius tubes,

while tubes with large radii are less affected. This is indicative of the crossover from one-dimensional to two-dimensional behavior. We have shown that carbon nanotube heterojunctions formed from two metallic tubes conduct if the defects at the interface are arranged asymmetrically. If the defects preserve the rotational symmetries of the two tubes, conductance gaps appear. Consequently, bent junctions conduct better than straight junctions on average. Owing to their novel properties, carbon nanotube heterojunctions with conductance gaps may be used as nanoscale thermistors, as well as optically-activated and voltage-activated electrical switches.

Chapter 11

Collapsed carbon nanotubes

11.1 Introduction

The strength of the carbon-carbon bond implies that perfect carbon nanotubes should have extremely high tensile strength[113, 10, 12]. However, large resistance to an increase in axial length does not guarantee resistance to radial deformation. The component graphitic sheets of a nanotube, though difficult to stretch, are easy to bend. For example, arrays of parallel single-walled nanotubes flatten at the lines of contact between tubes so as to maximize the intertube attractive interaction[114], a distortion consistent with energetic models of such structures[114, 98].

More dramatic deformations can be stabilized by the intersheet attraction[115] between opposing walls of the *same* tube[116]. A tube may collapse into a flat strip of thickness $(2N-1)d$ where N is the number of graphitic walls and d is the graphitic interwall spacing of ~ 3.35Å. The collapsed tube differs in total energy from the corresponding circular tube for two reasons. First, any departure from the circular cross-section increases the curvature contribution to the energy. High curvature admixes sp^3-bonding into the sp^2 network, imposing an energetic cost. Second, circular tubes with diameters much larger than d have an insignificant attrative interaction between atoms on opposite sides of the circular perimeter. If the tube flattens so that the opposite sides are flat sheets a distance $\sim d$ apart, the intersheet attraction lowers the energy.

We illustrate the essential physics with a simple model based on the schematic cross-section of Fig. 11.1. The collapsed tube is a two-sheeted strip of thickness d with bulbs on the edges of radii r and arclength a. Denoting the radius of the corresponding circular

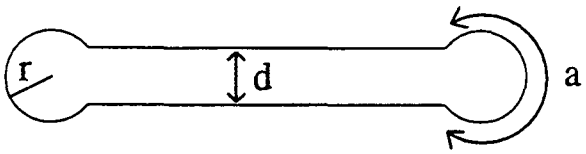

Figure 11.1: Simplified schematic cross-section of a flattened nanotube. The bulbs are approximated as circular arcs.

tube by R, the width of the flat strip is $\pi R - a + 2r \sim \pi R$ for $a, r << R$. The difference in curvature energy between collapsed and circular tubes per axial length is

$$\Delta E_{\text{curv}} = k\left(\frac{a}{r^2} - \frac{\pi}{R}\right) \tag{11.1}$$

where k is the mean curvature modulus of a graphite sheet. The additional intersheet attraction per unit axial length in the collapsed tube is

$$\Delta E_{\text{attr}} = -\epsilon_{\text{attr}}(\pi R - a) \tag{11.2}$$

where ϵ_{attr} is absolute value of the interaction energy per unit area between two graphite sheets separated by d. Since the competition between curvature and intersheet attraction is played out locally at the bulbs, we take a and r to be functions of d, k and ϵ_{attr}, independent of R for $R >> a, r$. As the radius R of the circular tube increases, the energetic cost of collapse ΔE_{curv} approaches a constant while the energetic gain ΔE_{attr} increases linearly. Above a critical radius, R_{crit}, flat tubes are favored. The value of R_{crit} depends on the ratio $(\frac{\epsilon_{\text{attr}}}{k})$ and the intersheet spacing d.

We use a variational model to estimate R_{crit} as a function of the number of walls for a flattened multiwalled tube with realistic cross-section. The inputs are k, ϵ_{attr}, and d, which we obtain from a combination of experiments and *ab initio* calculations. We then compare the theoretical results for bulb cross-sections to TEM images of collapsed nanotubes, and extract an estimate of the graphite intersheet attractive energy.

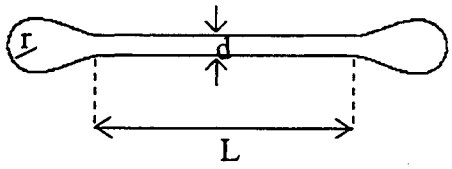

Figure 11.2: Cross-section of a flattened nanotube. The cross-section is described by the width L of the central flat portion, the interwall spacing d, the radius r of the semicircle, and the radius R of the corresponding circular tube.

11.2 Elastic Model

A two-parameter family of trial shapes is used to model the geometry of an N-walled collapsed nanotube. After describing the trial shapes, we outline the variational calculation for first single-walled and then multi-walled tubes. We show that the bulb size decreases as $(\frac{\epsilon_{\text{attr}}}{k})$ increases. The critical radius for stability of an N-walled collapsed tube, $R_{\text{crit}}(N)$, is determined.

Opposing walls of a flattened single-walled nanotube collapse to a distance d apart. Assuming that the graphite sheet does not tear, the two flat sections must join at the edges. If $\epsilon_{\text{attr}} d^2 \sim k$, the edges bulge smoothly to decrease the local curvature energy, yielding the cross-section shown in Fig. 11.2. We model the edges as semicircles joined to the flat region by the curve $\alpha \sin(\beta x + \gamma) + \delta$. The constants α, β, γ and δ are chosen by imposing continuity in value and slope at the boundaries of the sin curves.

Four parameters determine the shape of the collapsed tube: the distance d between the flattened walls, the radius r of the semicircle in the bulb, the length L of the flat region and the perimeter $2\pi R$ of the collapsed tube, written as the circumference of the corresponding circular tube. The length of the sin-portion is determined by these four parameters. As long as R is much larger than a typical graphite intersheet spacing, the distance d between flat walls is always nearly ~ 3.35 Å. Thus, we fix $d = 3.35$ Å for all

tubes.

The variational calculation minimizes the sum of the curvature and intersheet attraction energies as a function of (r, L) for each circular tube radius R. All energies are defined per unit axial length (out of the page in Fig. 2), with the zero of energy taken as the energy per unit length of a $2\pi R$-wide strip on an isolated flat graphite sheet. A circular tube with radius $R >> d$ will have a negligible contribution from intersheet attraction, but will have the curvature energy

$$E_{\text{circular}} = \frac{k}{2}\frac{(2\pi R)}{R^2} = \frac{\pi k}{R}, \tag{11.3}$$

with k the mean curvature modulus of a graphite sheet[117]. This expression accurately fits *ab initio* calculations of the total energies of circular carbon tubes[118] when $k = 1.4$ eV. As long as R is large, k is independent of the helicity of the tube because the in-plane elastic properties of a graphite sheet are isotropic.

A surface with one-dimensional translational symmetry and a cross-section defined by $y = f(x)$ has a curvature energy

$$\frac{k}{2}\int \frac{dl}{[R(x)]^2} = \frac{k}{2}\int dx \frac{[f''(x)]^2}{\{1 + [f'(x)]^2\}^{\frac{5}{2}}}, \tag{11.4}$$

We use this expression to calculate the curvature energy of the sin-portions of the collapsed tube. Adding the contribution from the semi-circular regions, we obtain the curvature energy of a collapsed tube, $E_{\text{collapsed}}$, as a function of the perimeter $2\pi R$, and the structural parameters (r, L).

The energy of intersheet attraction in a single-walled collapsed tube is calculated by partitioning the cylindrical surface into axial strips and summing the Lennard-Jones interaction over pairs of strips. Each strip has an infinitesimal width w perpendicular to the axis. The Lennard-Jones interaction between two parallel, infinitely long strips is of the form

$$V_{LJ}(D) = -\frac{s}{D^5} + \frac{t}{D^{11}}, \tag{11.5}$$

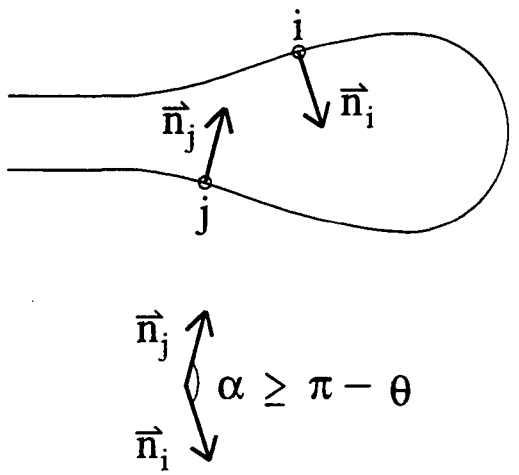

Figure 11.3: V_{LJ} is only calculated between points i and j if the angle, α, between inward normals is $\geq \pi - \theta$.

where D is the distance between strips and $s, t > 0$. The coefficients s and t are determined by two constraints: the interaction energy between infinite sheets is a minimum at $D = d$ and the interaction energy per area at this distance is $-\epsilon_{\text{attr}}$. We obtain

$$s = 1.2505 w^2 \epsilon_{\text{attr}} d^4 \tag{11.6}$$

$$t = 0.8204 w^2 \epsilon_{\text{attr}} d^{10}. \tag{11.7}$$

Eqn. 11.5 contains an inconvenient divergence from neighboring points in the same layer. The divergence is inconsequential since it can be eliminated by referencing all energies to the (equally divergent) single graphite sheet Lennard-Jones energy per $2\pi R$ of width. We avoid divergent terms by excluding contributions between portions of the surface whose normals point in nearly the same direction. Consider two strips at points i and j on the surface (see Fig. 11.3) with $\hat{\mathbf{n}}_i$ and $\hat{\mathbf{n}}_j$ the inward unit normals. We include $V_{LJ}(i,j)$ in the intersheet energy only if $\hat{\mathbf{n}}_i \cdot \hat{\mathbf{n}}_j \leq -\cos\theta$, with θ between 0 and π. If $\theta = 0$, then V_{LJ} only includes interaction between the two straight portions of the tube.

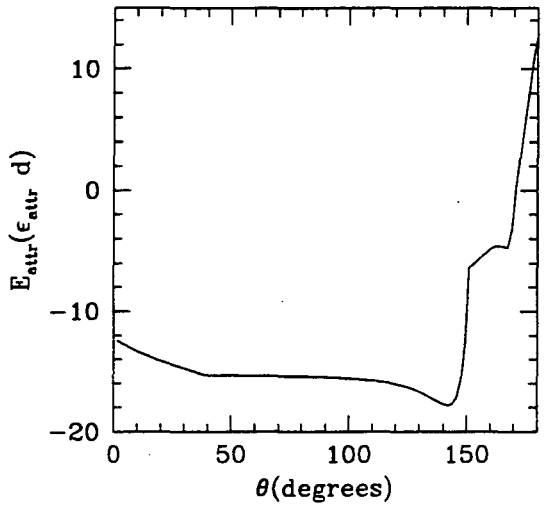

Figure 11.4: Energy of interlayer attraction (per length) vs. θ for a collapsed tube with $2\pi R = 167.5$ Å, $L = 40.9$ Å, $r = 4.7$ Å. Between $\theta = 40°$ and $\theta = 90°$, E_{attr} is roughly independent of θ. E is given in units of $\epsilon_{attr}d$.

If θ is greater than 0, contributions from the curved portions are considered as well. As long as θ is significantly less than π, the divergent contributions from neighboring points are excluded.

This method of excluding divergent terms is justified if the calculated energy is independent of θ for a wide range of intermediate angles. Fig. 11.4 shows the intersheet attractive energy as a function of θ for the single-walled tube whose cross-section is depicted in Fig. 11.2 (structural parameters $2\pi R = 167.5$Å, $L = 40.9$ Å, and $r = 4.7$ Å). The energy asymptotes between $\theta = 40°$ and $\theta = 90°$ before diverging near $\theta = 145°$ due to the inclusion of nearby pairs. For θ between 40° and 90° contributions from the curved regions are included, but divergent terms in the Lennard-Jones self-energy are excluded. We find that $\theta = 50°$ is suitable for all tubes studied.

The prescription for calculating the equilibrium cross-section of a single-walled collapsed tube with circumference $2\pi R$ is simple: values for L and r are chosen. The

curvature energy, E_{curv}, is calculated using Eqn. 11.4. Then the interlayer energy, E_{attr}, is calculated by summing the Lennard-Jones interaction of Eqns. 11.5-11.7 between pairs of strips, subject to the normal vector condition with $\theta = 50°$. This yields $E_{\text{collapsed}}(2\pi R; L, r) = E_{\text{curv}} + E_{\text{attr}}$, the energy per length of the collapsed tube relative to a flat graphite sheet per $2\pi R$ of width. The energy is minimized with respect to L and r to obtain $E_{\text{collapsed}}(2\pi R)$.

Additional complications arise in calculating the equilibrium cross-sections of N-walled collapsed tubes. Consider a two-walled circular tube with inner radius R. If $R >> d$, the distance between the walls of the two concentric tubes is nearly d. We take the radius of the outer tube to be exactly $R + d$. The circumference of the outer wall is then $2\pi(R + d) = 2\pi R + 2\pi d$. The increase in circumference between inner and outer walls is $2\pi d$, independent of R.

Now imagine the collapsed version of the same tube. We assume that the walls have cross-sections described by trial shapes with parameters $\{r(1), L(1)\}$ and $\{r(2), L(2)\}$. It is reasonable to assume that the perpendicular distance between flat portions of inner and outer walls remains d. The curved portions, however, present a problem. In order for the circumference of the outer wall to be exactly $2\pi d$ greater than the circumference of the inner wall, the distance between inner and outer walls in the curved region must be less than d somewhere[119]. This reduction in interlayer spacing is energetically disfavored since $V_{LJ}(D)$ increases rapidly as D falls below d. The best cross-section can be determined by minimizing the total energy (which includes the interlayer attraction between inner and outer walls) with respect to the parameters $r(1)$, $L(1)$, $r(2)$, and $L(2)$. This is rather tedious, especially for large numbers of walls.

Instead, we make an ansatz which reduces the number of parameters to two: let $r(2) = r(1) + d$ and $L(2) = L(1)$. This supposition is illustrated in Fig. 11.5. The lengths of the straight and sin-portions are now the same for inner and outer walls, while the excess length of the outer semicircular regions is $2\pi(r + d) - 2\pi r = 2\pi d$. The

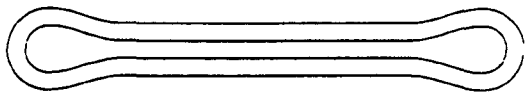

Figure 11.5: Cross-section of a 2-walled collapsed tube. We take $r(2) = r(1) + d$, and $L(1) = L(2)$.

ansatz forces the circumference of the outer wall to be precisely $2\pi(R+d)$, as required. Furthermore, the only place where the closest distance between walls is less than d is in the sin-portions. The deviation from d will be small as long as $r(1)$ is not too much larger than $\frac{d}{2}$, an assumption that will be justified by the results for the dimensions of the bulbs.

The ansatz is easily generalized to any number of walls: Let

$$\begin{aligned} r(j) &= r(j-1) + d \qquad & 1 < j \leq N \\ L(j) &= L(1) & 1 < j \leq N. \end{aligned} \tag{11.8}$$

With these assumptions, the jth wall has a circumference of $2\pi R + 2\pi(j-1)d$ and the small decrease in distance between adjacent walls in the sin-portions incurs only a minor energetic cost. Furthermore, there are just two variational parameters, $\{r(1), L(1)\}$, as for the single-walled case. The general prescription for calculating the equilibrium cross-section of an N-walled collapsed tube is the same as outlined above, with E_{curv} calculated for all walls and E_{attr} including interactions between walls. The zero of energy is now taken to be the energy per length of an N-sheeted slab of graphite per $\pi(2R + (N-1)d)$ of width (the average circumference of the N walls). It should be noted that the parameters $\{r(1), L(1)\}$ which minimize the total energy for an N-walled collapsed tube may depend on N, i.e. the shape of the curved regions may change as the number of walls increases.

Before presenting results for $R_{\text{crit}}(N)$, we discuss the value of ϵ_{attr} to be used. Although the mean curvature modulus $k = 1.4$ eV and the graphitic interwall spacing

$d = 3.35$ Å are well known, the intersheet attraction is a subject of controversy. Attempts to determine ϵ_{attr} have yielded disparate values.

Local density approximation calculations can have difficulty with the correlation-born Van der Waals energy. Bearing in mind this weakness, two different local density approximation calculations yield $\epsilon_{attr} \approx 0.02$ eV/atom[120] and $\epsilon_{attr} \approx 0.03$ eV/atom[121] for the intersheet attraction between graphitic layers. One calculation yields $\epsilon_{attr} \approx 0.02$ eV/atom[122] for the intersheet attraction between layers of a small two-walled nanotube.

The most direct experimental measurement is heat of wetting, which yields $\epsilon_{attr} \approx 0.04$ eV/atom[123]. Although this value is in reasonable agreement with the difference between an sp^2 bond-energy sum and the graphite heat of vaporization[124], the bond energy sum minus the heat of vaporization is the difference of large, imprecisely known numbers. Comparable values also obtain from theoretical calculations of interatomic (e.g. Lennard-Jones) force laws[123, 125].

Several alternative approaches yield widely dispersed values. Fits of empirical interatomic interactions to a large database of sp^3 hydrocarbon binding energies yield a carbon-carbon van der Waals interaction which implies $\epsilon_{attr} \approx 0.002$ eV/atom[126]. This value is corroborated by fits of a two-parameter interatomic potential to the c-axis compressibility and interlayer spacing of sp^2 graphite[127]. Applying fits of intermolecular N_2 interactions to carbon atoms yields a similar value, $\epsilon_{attr} \approx 0.003$ eV/atom[128]. Alternative theoretical calculations and semiempirical estimates yield a clutch of larger values, $\epsilon_{attr} \approx 0.1$ eV/atom[129], $\epsilon_{attr} \approx 0.17$ eV/atom[130], $\epsilon_{attr} \approx 0.2$ eV/atom[131]. In our opinion, the groupings of values around 0.002 and 0.2 are suspect since they are sensitive to the choice of empirical force law and/or do not address the idiosyncratic qualities of graphite.

The wide dispersion in estimates for ϵ_{attr} may seem discouraging, but our TEM images will in fact allow us to directly measure the bulb radius. Combining these direct

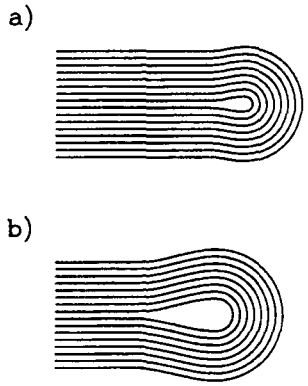

Figure 11.6: Calculated equilibrium cross-section of an 8-walled bulb using a) $\epsilon_{\text{attr}} = 0.05$ eV/atom, and b) $\epsilon_{\text{attr}} = 0.005$ eV/atom.

measurements with our elastic theory then yields the first direct microscopic measure of the interlayer attraction in graphite. Anticipating these results, we will focus on intermediate values of ϵ_{attr} near 0.05 eV/atom.

Fig. 11.6 shows calculated bulb cross-sections of an eight-walled collapsed tube for two choices of the intersheet attraction, $\epsilon_{\text{attr}} = 0.05$ eV/atom and $\epsilon_{\text{attr}} = 0.005$ eV/atom, taking $k = 1.4$ eV in both cases. The bulb size increases as $(\frac{\epsilon_{\text{attr}}}{k})$ decreases. The radius of the innermost wall of the bulb is 3.6 Å for $\epsilon_{\text{attr}} = 0.05$ eV/atom, and 8.0 Å for $\epsilon_{\text{attr}} = 0.005$ eV/atom. Bulbs are larger for weaker intersheet attraction since the loss of attraction between opposite sides of the inner wall is proportional to $\epsilon_{\text{attr}} r$ while the curvature energy goes like $\frac{k}{r}$. Thus, $r \sim (\frac{\epsilon_{\text{attr}}}{k})^{-\frac{1}{2}}$.

Our models for the curvature and inter-sheet attractive energies determine the energy (per length) of an N-walled circular tube of inner radius R. This energy can then be compared to the energy of the corresponding collapsed tube with inner circumference $2\pi R$. The collapsed tube is favored for large R. Define R_{crit} so that a collapsed tube

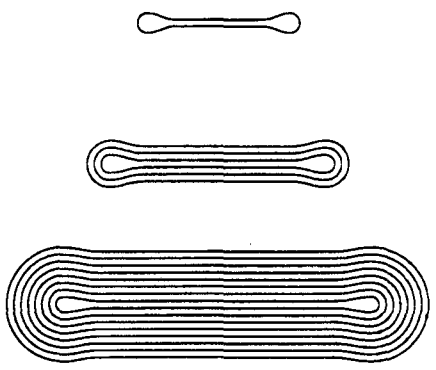

Figure 11.7: Calculated equilibrium cross-sections for 1-walled, 3-walled, and 8-walled collapsed tubes with inner-wall circumferences $2\pi R_{\text{crit}}(1)$, $2\pi R_{\text{crit}}(3)$, and $2\pi R_{\text{crit}}(8)$ respectively. Their widths (distances between outer-wall bulb tips) are 77 Å, 121 Å, and 201 Å.

with inner circumference $2\pi R_{\text{crit}}(N)$ has the same energy as the circular tube with inner radius $R_{\text{crit}}(N)$. Because the attractive energy lowering in collapse is roughly independent of N, and the curvature energy gain increases with N, $R_{\text{crit}}(N)$ is an increasing function of N.

Fig. 11.7 shows the calculated equilibrium cross-sections of one, three, and eight-walled collapsed tubes with inner circumferences of $2\pi R_{\text{crit}}(1)$, $2\pi R_{\text{crit}}(3)$, and $2\pi R_{\text{crit}}(8)$ respectively. The inner circumference of the collapsed tubes increases with the number of walls. Fig. 11.8 shows a plot of R_{crit} as a function of N for $1 \leq N \leq 8$. The inner wall bulb radius $r(1)$ decreases from 4.7 Å to 3.6 Å as the number of walls increases from 1 to 8[132].

The plot of Fig. 11.8 can be thought of as a phase diagram. Each tube with dimensions R, N can be represented by a point in the (R, N)-plane. In equilibrium,

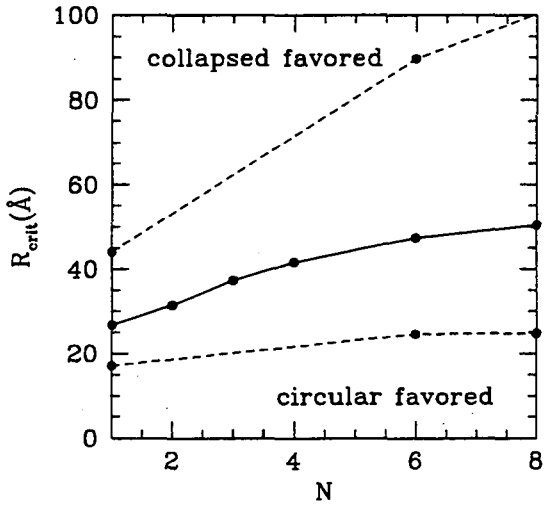

Figure 11.8: Critical radius for tube stability R_{crit}, as a function of the number of walls N, calculated with $\epsilon_{\text{attr}} = 0.05$ eV/atom (solid line). For large N and small R, circular tubes are favored, while for small N and large R, collapsed tubes are favored. The upper and lower dashed curves correspond to $\epsilon_{\text{attr}} = 0.025$ eV/atom and $\epsilon_{\text{attr}} = 0.1$ eV/atom respectively. This shows the sensitivity to the choice of ϵ_{attr}.

tubes represented by points lying above the R_{crit} vs. N line are collapsed, while tubes below are have circular cross-sections. Of course, the equilibrium situation is probably not realized, for the energy barrier towards collapse is much larger than k_BT. Tube geometries are most likely dominated by kinetics. We then ask the question: How large must R be for the collapsed configuration to be *metastable*? The critical radius for metastability, $R_{\text{meta}}(N)$, is defined so that an N-walled tube with inner circumference $2\pi R_{\text{meta}}(N)$ has *no* energy barrier between collapsed and circular states. Although we do not calculate this precisely, it can be approximated by considering a collapsed tube with its straight portion removed. A collapsed tube with a straight section will have an attractive interaction between opposing walls which maintains its structure. Without it, the tube will return to a circular cross-section to release the curvature energy. This suggests the following relationship:

$$R_{\text{meta}}(N) \approx R_{\text{crit}}(N) - \frac{1}{\pi} L_{\text{crit}}(1), \tag{11.9}$$

where $L_{\text{crit}}(1)$ is the length of the straight portion of the inner wall for a collapsed tube with $R = R_{\text{crit}}$. Again, $R_{\text{meta}}(N)$ increases as N increases. In particular, $R_{\text{meta}}(1) \approx$ 13.6 Å and $R_{\text{meta}}(8) \approx 14.6$ Å, a relatively weak dependence on N.

11.3 Analysis of TEM images

Although we expect our model to predict reasonable cross-sections for collapsed tubes, it neglects one important aspect of their morphology. Experimentally observed collapsed tubes are often twisted along their length (like party streamers). Figure 11.9 displays a TEM image of a twisted, collapsed carbon nanotube. The place where the apparent width is smallest indicates the point at which the plane of the flattened tube is parallel to the viewing direction. Examination of the fringes far from this point shows that this tube has eight concentric walls. However, a count performed in the small-width area yields more than 2×8 fringes. These extra fringes come from portions of the walls

which are in the bulb regions.

Bulb-derived fringes can also be seen elsewhere in the image. When the flat tube is tilted toward the viewer, different portions of the bulb walls are parallel to the electron beam. These regions provide heightened contrast which appear on the left side of the twist, both above and below the small-width area. It is possible to obtain an estimate of the bulb size by measuring the distance between these bulb-derived fringes and "normal" wall fringes [133], a fact we shall exploit below. Note that these bulb-derived fringes appear on only one side of the image.

The appearance of the bulbs on just the left side suggests that they do not bulge symmetrically on either side of the flat region, but instead bulge to just one side, as shown in Fig. 11.10. This unusual structure can be understood as a symmetry-breaking cupping deformation of a twisted ribbon. To wit, it is impossible to twist a strip of paper while maintaining a straight cross-section without introducing either cupping or kinks. We now explain this using elasticity theory.

For simplicity we consider the elastic deformations of a twisted sheet as opposed to a twisted flattened tube. The simplest model of a twisted sheet would have a straight cross-section. However, a twisted sheet with a straight cross-section has Gaussian curvature. Therefore, a material with large Gaussian curvature modulus is unstable towards cupping. In the cupped state the sheet cross-section, although curved, yields a surface of zero Gaussian curvature.

A twisted ribbon with a straight cross-section has a Gaussian curvature given by

$$\frac{-\left(\frac{\lambda}{2\pi}\right)^2}{\left(\left(\frac{\lambda}{2\pi}\right)^2+x^2\right)^2}, \tag{11.10}$$

where λ is the length of the twist along the screw axis, and x is the cartesian coordinate pointing parallel to the straight line in Fig. 11.10. The screw axis goes through $x = 0$. If the cross-section of the twisted ribbon is described by $f(x)$, then the condition of zero

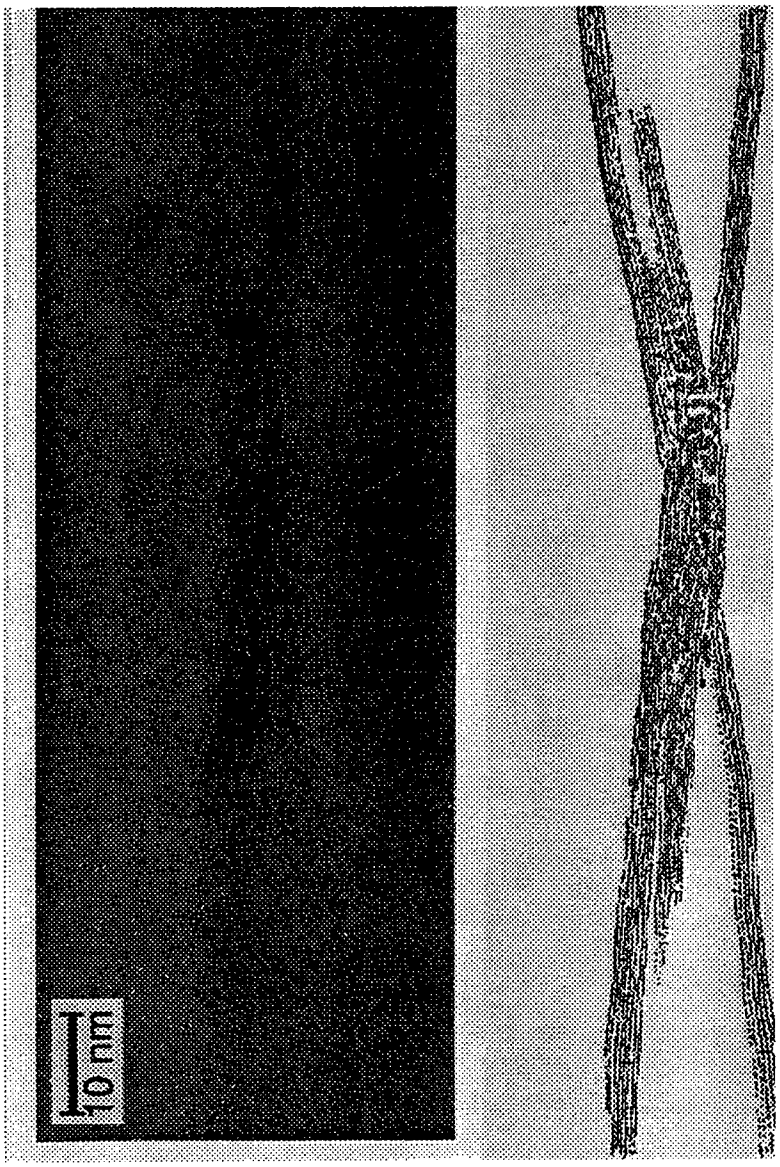

Figure 11.9: TEM image of a twisted, collapsed carbon nanotube taken by N.G. Chopra. Beside it is an interperative line drawing.

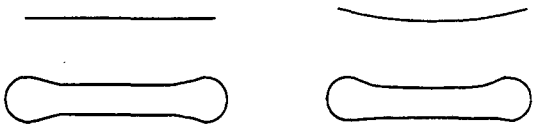

Figure 11.10: Schematic cross-section showing the cupping of a twisted nanotube, in analogy to the cupping of a twisted single-layered ribbon. For clarity only a single layer of the tube is shown. The curved line is a numerical solution of Eqn. 11.11.

Gaussian curvature yields a nonlinear differential equation for f,

$$f''\left(xf'-f\right)=\left(1+(f')^2\right)^2. \tag{11.11}$$

Since the right-hand side is always positive, the curvature f'' has constant sign, consistent with a cupped geometry. The additional constraint that $f''(xf'-f)$ is positive guarantees that the solution does not curve away from the origin when $f'=0$. A sample numerical solution yields the cross-section shown on the righthand side of Fig. 11.10. For the actual multilayered flattened tube we suspect that the cupping concentrates in the already-bent bulbs, flattening one side and accentuating the other with a lesser curvature introduced into the previously flat region between the bulbs.

This symmetry-breaking cupping instability explains the visibility of bulbs on just one side of the image. The large angle at which the bulbs are seen is also attributed to the cupping instability, which concentrates the bulb on one side of the tube.

The minimum spacing between the bulb-derived walls and the primary walls is not the graphitic interwall spacing but instead the diameter of the bulb. The TEM image of Fig. 11.9 shows this gap for the bulb-derived walls below the crossover. The minimum spacing, 7 ± 1 Å, is a good approximation to the diameter of the inner bulb. The bulb diameter is a function of the ratio of the graphite intersheet attraction to the mean curvature modulus; since the curvature modulus is well known, the elastic modelling allows an estimate of the intersheet interaction in graphite, a difficult quantity to access

Table 11.1: Experimentally observed collapsed tube parameters, along with the ϵ_{attr} that would yield these results in our model. N is the number of walls, and R is the inner radius of the corresponding circular tube (in nm). The inner-wall bulb diameter is in Å, and ϵ_{attr} is in eV/atom.

N	R	Bulb diameter	ϵ_{attr}
8	5.2	7 ± 1	0.05 ± 0.02
6	7.4	8 ± 2	$0.04 + 0.04 - 0.02$
8	5.2	9 ± 1.5	$0.02 + 0.02 - 0.01$
Average	—	—	$0.035^{+0.015}_{-0.01}$

either experimentally or theoretically. Using our elastic model, a bulb diameter of 7 ± 1 Å for an eight walled tube implies $\epsilon_{attr} = 0.05 \pm 0.02$ eV/atom. Similar analyses of other twists yield the values quoted in Table 11.1.

Returning to the controversy surrounding the strength of ϵ_{attr}, our direct measurements of bulb size rule out both the lower and upper sets of estimates for the intersheet attraction ($\epsilon_{attr} = 0.002$—0.003 and 0.1—0.2). Instead, they support the heat of wetting experiments and/or the LDA results.

11.4 Conclusion

Continuum elasticity theory with a Lennard-Jones description of intersheet attraction yields the equilibrium cross-sections of collapsed carbon nanotubes. Tubes with few walls and large radii favor collapse over the more familiar circular cross-section. The size of the bulbs on the edges of collapsed tubes depends sensitively on the ratio of the intersheet attraction to the mean curvature modulus. Analysis of TEM images of twisted collapsed tubes allows us to extract information about their geometry. Comparison of theory and experiment affords an estimate of the graphite intersheet attractive energy,

$0.035^{+0.015}_{-0.01}$ eV/atom.

Chapter 12

Planar carbon pentaheptite

The discovery of fullerenes[6] and nanotubes[10] has induced a rennaisance in the study of novel carbon-based materials. Fullerenes, nanotubes, graphite, and diamond provide quasi-zero, one, two, and three dimensional insulators, semiconductors and/or semimetals. The utility of pure-carbon materials would be enhanced if a higher density of states metallic allotrope could be found. We propose an ordered planar arrangement of pentagons and heptagons as a good metal. A single sheet of planar carbon pentaheptite is a mechanically strong covalently-bonded conductor.

An isolated graphite sheet is a semimetal with π and π^* bands touching at a pointlike Fermi surface. A reduction in symmetry below hexagonal can remove this degeneracy and eliminate semimetallic behavior. In this situation the strong carbon potential might be expected to open significant gaps near the Fermi level. However, a structure with a large number of atoms in a low-symmetry unit cell would favor a band-overlap metal. We provide an example of a pure-carbon planar metal composed of a periodic array of pentagons and heptagons.

Any structure with an equal number of pentagons and heptagons and threefold vertices has zero net curvature. If the pentagons and heptagons are nearly uniformly distributed, one might expect local flatness as well. Although there are an infinite number of ways of tiling a plane with equal numbers of heptagons and pentagons, a large subset of physically reasonable tilings can be generated by taking a graphite sheet, dividing it into diamonds of four adjacent hexagons, and rotating certain bonds by $\frac{\pi}{2}$ as shown in Fig. 12.1[134]. Each bond rotation of the interior bond on the diamond generates two pentagons and two heptagons. Additional tilings outside the bond rotation algorithm

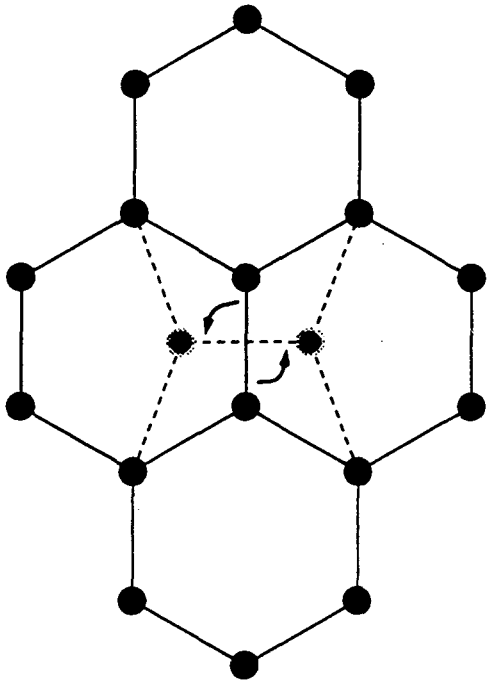

Figure 12.1: The bond rotation algorithm which converts graphite to a sheet of interlinked pentagons and heptagons.

can be generated by clustering pentagons or heptagons. However, bond rotation can produce patterns with minimal local curvature, or equivalently, minimal variation in bond length in a planar structure.

We choose to examine the simplest possible way of tiling a plane with pentagons and heptagons, namely a periodic network with one bond rotation per primitive cell. Although there are two distinct ways of decorating a graphite sheet with diamond-shaped primitive cells of four hexagons and then rotating the interior bonds of each diamond, both methods yield topologically equivalent structures with eight atoms per unit cell. As shown in Fig. 12.2, each pentagon is adjacent to one pentagon and four heptagons. Each heptagon is adjacent to four pentagons and three heptagons. Two carbon atoms are shared by two pentagons and a heptagon, the other six carbon atoms being shared by one pentagon and two heptagons.

Nearest-neighbor curvature effects of pentagonal and heptagonal rings limit the num-

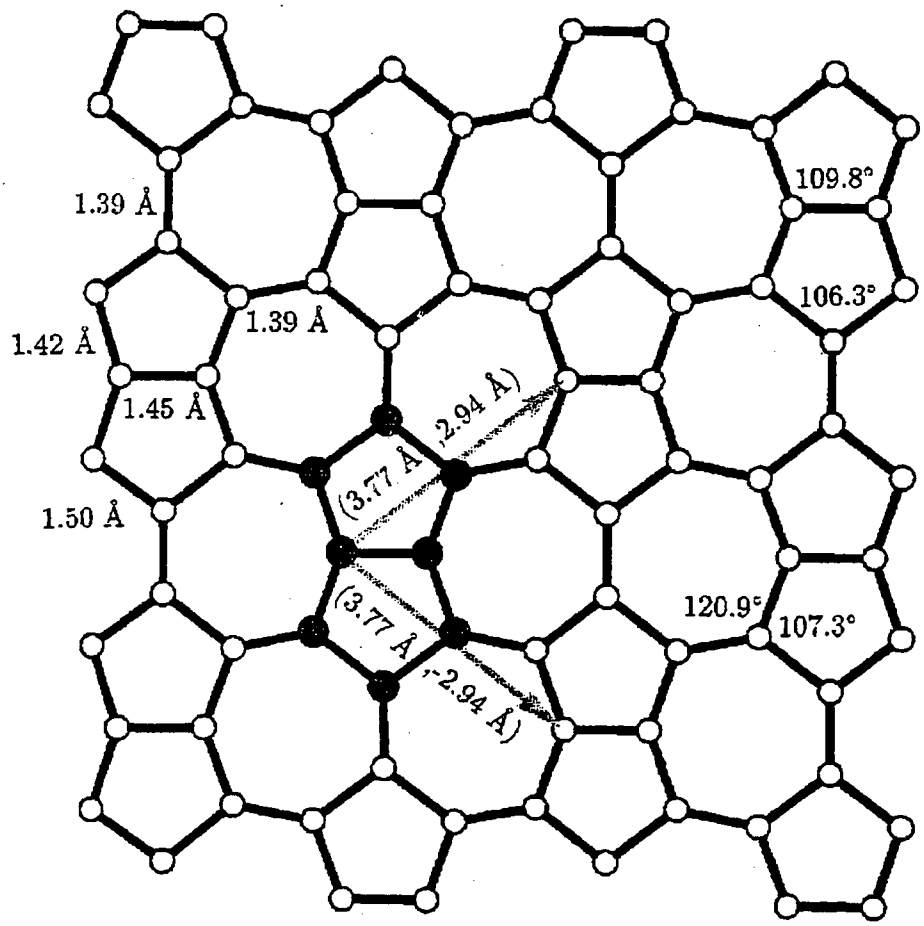

Figure 12.2: The annealed equilibrium structure of single-sheet planar carbon pentaheptite, with unit cell, lattice vectors, and bond parameters marked.

ber of plausible two-dimensional carbon networks. If a pentagon has only heptagonal neighbors, the incipient local negative curvature imposes a large energetic cost. If a pentagon has two or more pentagonal neighbors, the incipient local positive curvature imposes a similar large energetic cost. Bond length and bond angle variation in the planar structure is minimized when each pentagon has one pentagonal neighbor. The requirement of a small unit cell then leads uniquely to the structure chosen for study.

Initial atomic coordinates were obtained from a crude bond rotation construction and subsequently annealed within tight-binding total energy molecular dynamics[55]. The anneal was performed on a finite 141 atom sheet. After initial local relaxation, the atomic positions were perturbed randomly by ~0.1 Å from equilibrium and the structure was annealed from 2500 K for 2.7 picoseconds. Upon cooling the atoms returned to the essentially planar equilibrium positions. Unit cell coordinates were extracted from the atoms in the center of the sheet. Comparison across the interior atoms indicated that finite size effects perturbed atomic positions by less than 0.01 Å. Bond lengths and angles are shown in Fig. 12.2.

It is instructive to compare bond lengths in planar carbon pentaheptite with those in pentalene, the molecule formed by terminating with hydrogens the dangling bonds of the pentaheptite unit cell highlighted in Fig. 12.1. The major difference is a lengthening of bonds to the apical carbons, from ~1.4 Å in D_{2h} pentalene[135] to 1.50 Å in pentaheptite. The carbon atoms making up these bonds in pentaheptite share 1.39 Å carbon-carbon bonds with atoms in the neighboring unit cells, in contrast with the weaker, but analogous, C—H bonds in pentalene. In pentaheptite, the increase in effective bond number for the intercell bonds is accompanied by a decrease in the effective bond number and consequent dilation of the intracell bonds to the apical carbons. We note that the dilation of the pentaheptite C—C bonds from graphitic bond lengths and the more open nature of the planar carbon pentaheptite structure yield an areal atomic density of one carbon atom per 2.77 $Å^2$, 5% less than the graphitic density.

Electronic structure and total energy calculations were performed on the single-sheet periodic structure extracted from the finite sheet simulation. Within the tight-binding total energy scheme, the energy of a single infinite sheet of carbon pentaheptite is ~0.32 eV per atom above that of single-sheet graphite. By comparison, within the same scheme C_{60} is ~0.4 eV per atom above single-sheet graphite. A local density approximation *ab initio* pseudopotential calculation using the same atomic coordinates yields a 0.33 eV per atom energy difference between isolated sheets of pentaheptite and graphite. The bond rotation which generated the topology of pentaheptite also provides a kinetic pathway to graphite. Fixing the absolute angle of a single rotated bond in the center of the 141 atom sheet and annealing and relaxing atomic coordinates up to third nearest neighbors (including the bond length of the rotated bond) yields an energy barrier within tight-binding total energy of ~7 eV for the $\sim\frac{\pi}{2}$ rotation of a single non-symmetry axis interheptagonal bond and local conversion of pentaheptite into graphite[136]. The breaking of two C—C bonds along this pathway explains the large energy barrier. Global conversion of single-sheet pentaheptite to graphite by simultaneous rotation of all relevant bonds is expected to have a comparable energetic barrier. More complex kinetic paths can be envisioned, but all require the breaking and reformation of two C—C bonds per bond rotation so that a large energetic barrier is likely for the isolated sheet. The rigidity of the nearly sp^2 carbon framework argues against the possibility of soft modes, a supposition supported by the stability of the pentaheptite framework under a 2500 K anneal. All evidence available suggests that an isolated sheet of carbon pentaheptite is metastable towards conversion to lower energy carbon allotropes.

The tight-binding band structure[137] and density of states of a single sheet of carbon pentaheptite are shown in Fig. 12.3. The deviation from perfect sp^2 bond angles raises the σ bands. The lack of hexagonal symmetry then fills in the π-π^* pseudogap present at the Fermi level of single-sheet graphite, yielding a density of states at the Fermi level of ~0.1 states per eV per atom. In comparison, the density of states for the smallest

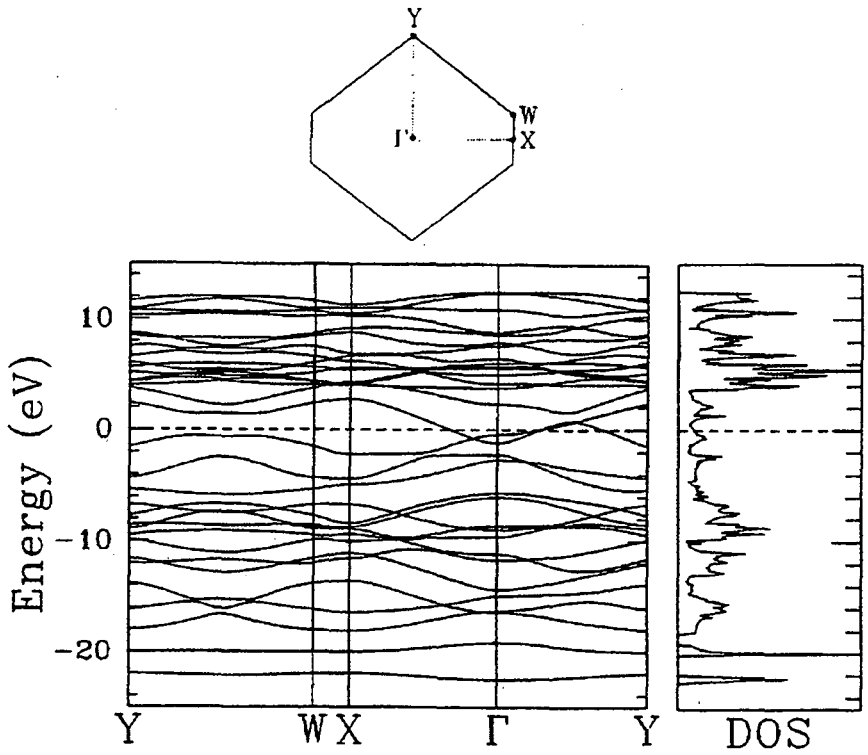

Figure 12.3: Band structure and density of states for an infinite single sheet of planar carbon pentaheptite. The dashed line marks the Fermi energy, E_F. Bands are plotted along high symmetry lines of the Brillouin zone, shown above. The reflection symmetry of the bands along the YW-line is due to time-reversal invariance, $E(\vec{k}) = E(-\vec{k})$. The states nearest E_F have π-character, and those farthest away are σ states.

plausible metallic nanotube, the 5.3 Å diameter (4,4) tube, is 0.07 states per eV per atom. For larger (n,n) metallic nanotubes the densities of states per atom drop inversely proportional to the tube radius, indicating that planar carbon pentaheptite is the largest density of states pure-carbon crystalline allotrope.

The planar pentaheptite stucture can be rolled into tubes indexed in a manner similar to graphite, wherein tubes are labelled (n,m) with n and m defining the circumferenital periodicity in lattice coordinates. In contrast to graphite, the rhomboid structure of pentaheptite implies that we must consider tubes with $0 \leq |m| \leq n$ instead of simply $0 \leq m \leq n$. Unlike the graphite sheet, carbon pentaheptite has a large Fermi surface which surrounds the Γ-point ($\mathbf{k} = 0$). Band-folding arguments[14] then predict all tubes to be metallic, independent of radius and helicity.

The nonzero Fermi level density of states of planar carbon pentaheptite motivates a brief discussion of superconductivity. Unlike curved C_{60} and the nanotubes[138], we expect no enhancement in the electron-phonon coupling due to curvature-induced $\sigma - \pi$ mixing. However, the deviation from perfect sp^2 bond angles in-plane may increase the electron-phonon matrix elements above the values in graphite. T_c of undoped pentaheptite is likely to be small or moderate. Alkali doping to a stochiometry of $\sim AC_4$, corresponding to one alkali atom per heptagon, should increase the density of states at the Fermi level and increase the superconducting T_c substantially.

Synthesis of planar carbon pentaheptite may be challenging. Formation of C_{60}, a carbon allotrope of comparable binding energy, is driven by the dangling bond energy of small carbon polymers in a carbon/helium plasma. Synthesis of planar pentaheptite requires a more subtle strategy since heptagons are strongly disfavored in a regime kinetically dominated by dangling bond energy. We entertain three possible synthetic strategies. First, it may be possible to form planar pentaheptite directly from graphite. Although the areal density of planar pentaheptite is 5% below that of graphite, the metallic nature of single-sheet pentaheptite suggests that the interplanar distance in the

bulk material will be smaller than the interplanar distance in bulk graphite. Should the equilibrium atomic density of bulk pentahaptite exceed that of graphite, external pressure may favor planar carbon pentaheptite. A photochemical strategy using high-pressure graphite may induce the transformation to pentaheptite. Suitable use of intercalated catalysts may also increase the stability of pentaheptite relative to graphite. Polymer chemistry may provide another avenue for synthesis. Several different cyclic hydrocarbons containing a multiple of eight carbon atoms provide candidates for the monomer. Halogenated pentalene and the pentalene dianion are an obvious precursors on geometrical grounds, as are various cyclic structures with side branches. The base unit of the bond rotation algorithm of figure 1 provides a 16-atom precursor that may be arranged in two inequivalent orientations to produce the planar pentaheptite structure studied in this work. Azulene itself cannot tile a plane without introducing vacancies or hexagons. Chemically selective intermolecular bonding should be aided by local curvature since heptagons will tend to form preferentially near pentagons and vice versa (of course hexagon formation must be avoided for the structure studied here). Epitaxial growth on a suitable substrate provides a third strategy. Although carbon-substrate interactions may be weak in the completed structure, the interaction between dangling bonds and the substrate in the growing material may modify the kinetic pathways enough to encourage epitaxial growth of the first layer. As regards synthesis, we note that $\sim \frac{\pi}{2}$ grain boundaries in pentaheptite involve little lattice distortion and should impose at most a minor energetic cost.

The incorporation of equal numbers of pentagons and heptagons into previously hexagonal planar carbon materials opens a new class of metallic carbon allotropes. The simplest form of planar carbon pentaheptite is a relatively good all-carbon covalently bonded planar metal. More complex structures with larger planar unit cells or tubular geometries can easily be envisioned.

References

Bibliography

[1] L.H. Aller, *The Abundance of the Elements* (Interscience Publishers, New York, 1961).

[2] The energy to remove a carbon $1s$ electron is ~ 20 Rydbergs, while the energy to remove a $2s$ or $2p$ electron is ~ 1 Rydberg.

[3] S. Fahy, X. W. Wang, and S. G. Louie, Phys. Rev. B **42**, 3503 (1990); **43**, 9299 (1990).

[4] D. Tomanek and S.G. Louie, Phys. Rev. B **37**, 8327 (1988).

[5] Dresselhaus, M. S. *et al.*, *Graphite fibers and filaments*, (Springer-Verlag, New York, 1988).

[6] H. W. Kroto, J. R. Heath, S. C. O'Brien, R. F. Curl, and R. E. Smalley, Nature **318**, 162 (1985).

[7] F. Diederich *et al.*, Science **252**, 548 (1991).

[8] W. Kratschmer, L.D. Lamb, K. Fostiropoulous, and D.R. Huffman, Nature **347**, 354 (1990).

[9] A.F. Hebard *et al.*, Nature **350**, 600 (1991).

[10] S. Iijima, Nature **354**, 56 (1991).

[11] S. Iijima and T. Ichihashi, Nature **363**, 603 (1993); D.S. Bethune et al., Nature **363**, 605 (1993).

[12] Treacy, M.M.J., Ebbesen, T.W., and Gibson, J.M., Nature **381**, 678 (1996).

[13] R. Saito, M. Fujita, G. Dresselhaus, and M.S. Dresselhaus, Appl. Phys. Lett. **60**, 2204 (1992).

[14] N. Hamada, S. Sawada, and A. Oshiyama, Phys. Rev. Lett. **68**, 1579 (1992).

[15] J. W. Mintmire, B. I. Dunlap and C. T. White, Phys. Rev. Lett. **68**, 631 (1992).

[16] S. Saito, Fall 1990 Materials Research Society Proceedings, Clusters and Cluster Assembled Materials, Boston, MA, ed. R.S. Averback, D.L. Nelson, abd J. Bernholc.

[17] K. Shirai, J. Phys. Soc. Jap. **61**, 2735 (1992).

[18] P.J. Benning *et al.*, Science **252**, 1417 (1991).

[19] Takahashi *et al.*, Phys. Rev. Lett. **68**, 1232 (1992).

[20] R. W. Lof et al., Phys. Rev. Lett. 68, 3924 (1992).

[21] N. Troullier and J. L. Martins, Phys. Rev. B 46, 1754 (1992).

[22] J. Yu, L. Bi, R. K. Kalia, and P. Vashishta, Phys. Rev. B **49**, 5008 (1994).

[23] N. Troullier and J. L. Martins, Phys. Rev. B 46, 1766 (1992).

[24] E. L. Shirley and S. G. Louie, Phys. Rev. Lett. 71, 133 (1993); S. G. Louie and E. L. Shirley, J.

Phys. Chem. Solids 54, 1767 (1993).

[25] T. Rabenau *et al.*, Z. Phys. B **90**, 69 (1993).

[26] C. Reber *et al.*, J. Phys. Chem. **95**, 2127 (1991).

[27] C. Hartmann et al., Phys. Rev. B 52, R5550 (1995).

[28] G. Gensterblum, Phys. Rev. Lett. 67, 2171 (1991).

[29] J. H. Weaver, J. Phys. Chem. Solids 53, 1433 (1992).

[30] L. J. Sham and T. M. Rice, Phys. Rev. 144, 708 (1966);

[31] W. Hanke and L. J. Sham, Phys. Rev. Lett. 43, 387 (1979); Phys. Rev. B 21, 4656 (1980).

[32] W. Ekardt and J. M. Pacheco, Phys. Rev. B 52, 16864 (1995); G. Onida et al., Phys. Rev. Lett. 75, 818 (1995).

[33] R. G. Parr, The Quantum Theory of Molecular Electronic Structure, (Benjamin, New York, 1963). The parameters are taken from the last two columns on p. 67. However, with little approximation, we only account for parameters of type (00|NN), and extrapolate the trends followed by these parameters to longer distances than are found in the benzene molecule. (The parameters approach the form $e^2/[4\pi\epsilon_0 R]$, where R is the separation between two carbons.)

[34] R. E. Haufler et al., Chem. Phys. Lett. 179, 449 (1991).

[35] J. de Vries et al. Chem. Phys. Lett. 188, 159 (1992); J. A. Zimmerman, J. R. Eyler, S. B. H. Bach, and S. W. McElvany, J. Chem. Phys. 94, 3556 (1991); D. L. Lichtenberger et al., Chem. Phys. Lett. 176, 203 (1991).

[36] L.-S. Wang, J. Conceiao, C. Lin, and R. E. Smalley, Chem. Phys. Lett. 182, 5 (1991).

[37] An analogous treatment of screening effects is used in Ref. 38

[38] M. R. Pederson and A. A. Quong, Phys. Rev. B 46, 13584 (1992).

[39] For theoretical studies of the C_{60} level scheme in the vapor phase, see F. Negri, G. Orlandi, and F. Zerbetto, Chem. Phys. Lett. 144, 31 (1988); and I. Laszlo and L. Udvardi, J. Mol. Struct. (THEOCHEM), 183, 271 (1989).

[40] P. Hohenberg and W. Kohn, Phys. Rev. 136, 864 (1964); W. Kohn and L. J. Sham, Phys. Rev. 140, 1133 (1965).

[41] For instance, see H. Chacham, X. Zhu, and S. G. Louie, Phys. Rev. B 46, 6688 (1992), and references therein.

[42] J. L. Martins and N. Troullier, Phys. Rev. 46, 1766 (1992); we infer the effects of compression on band widths from the results presented in this work.

[43] A. Lundin and B. Sundqvist, Europhys. Lett. 27, 463 (1994).

[44] For instance, one might compare the similarity of spectral features found in Ref. [5], in S. Leach et al., Chem. Phys. 160, 451 (1992), and in Y. Wang et al., Phys. Rev. B 51, 4547 (1995).

[45] R. S. Knox, Solid State Physics, Advances in Research and Applications, Suppl. Vol 3, (Academic, New York, 1963).

[46] F. Gugenberger *et al.*, Phys. Rev. Lett. **69**, 3774 (1992).

[47] H. Y. Fan, Phys. Rev. **78**, 808 (1950); H. Brooks and S. C. Yu (unpublished); see also S. C. Yu, PhD. thesis, Harvard University, 1964.

[48] A. Thess *et al.*, Science **273**, 483 (1992).

[49] We calculated the band-gap with the TB model of Ref. 3

[50] J.W. Mintmire, D.H. Robertson, B. I. Dunlap, R.C. Mowrey, D.W. Brenner, and C.T. White, Mater. Res. Soc. Sym. Proc. **247**, 339 (1992).

[51] J. Yu, R.K. Kalia, and P. Vashishta, Europhys. Lett. **32**, 43 (1995).

[52] J. C. Slater and G. F. Koster, Phys. Rev. **94**, 1498 (1954).

[53] N. Troullier and J. L. Martins, Solid State Commun. **74**, 613 (1990).

[54] L. Kleinman and D. M. Bylander, Phys. Rev. Lett. **48**, 1425 (1982).

[55] C. H. Xu, C. Z. Wang, C. T. Chan, and K. M. Ho, J. Phys: Condens. Matter **4**, 6047 (1992).

[56] A. A. Lucas, P. H. Lambin, and R. E. Smalley, J. Phys. Chem. Solids **54**, 587 (1993).

[57] S. Sawada and N. Hamada, Solid State Commun. **83**, 917 (1992).

[58] X. Blase, L.X. Benedict, E.L. Shirley, and S.G. Louie, Phys. Rev. Lett. **72**, 1878 (1994).

[59] T.W. Ebbesen, and T. Takada, Carbon **33**, 973 (1995).

[60] A metal-semiconductor junctions composed of two different structures of SiC has been described by F. Bechstedt and P. Kackell, Phys. Rev. Lett. **75**, 2180 (1995).

[61] F. Garcia-Moliner and V. R. Velasco, *Theory of Single and Multiple Interfaces*, World Scientific, Singapore, 1992.

[62] The four orbital per atom Slater-Koster parameterized tight-binding theories of [14, 58] also give gaps for the $(8,0)$ tube comparable to those derived within the one-orbital per atom π-electron approximation. See [58] for details.

[63] For $(5,3)$, the four orbital per atom tight-binding of [58] predicts a

gap roughly equal to that of the one orbital π-electron tight-binding.

[64] We use the $\pi - \pi$ nearest neighbor hopping parameter of Ref. [58].

[65] V. Heine, Phys. Rev. **138**, 1689 (1965).

[66] Relaxation of atomic coordinates near the interface is expected to slightly shift these interface states.

[67] Y. Miyamoto, M. L. Cohen, and S. G. Louie, Phys. Rev. B **52**, 14971 (1995).

[68] C. Kittel, *Introduction to Solid State Physics* (John Wiley and Sons, New York, 1996).

[69] P. R. Wallace, Phys. Rev. **71**, 622 (1947).

[70] J. -C. Charlier, J. -P. Michenaud, and X. Gonze, Phys. Rev. B **46**, 4531 (1992). We refer to the band structure of simple hexagonal (AA stacking) graphite calculated by these authors. Although the results will be somewhat different for a single graphite sheet, the differences are unimportant for the order-of-magnitude estimates we make here.

[71] D. M. Hwang, Sol. Stat. Com. **46**, 177 (1983).

[72] J. Krumhansl, and H. Brooks, J. Chem. Phys. **21**, 1663 (1953).

[73] W. DeSorba, and W. W. Tyler, Phys. Rev. **83**, 878 (1951); J. Chem. Phys. **21**, 1660 (1953).

[74] Ph. Lambin, L. Philippe, J. -C. Charlier, and J. -P. Michenaud, Comput. Mater. Sci. **2**, 350 (1994).

[75] In reality, the details of the states of a small slab are not well-described by those of a piece of the crystal with periodic boundary conditions. We use it here to take into account the discretization of the c-axis wavevector, k_c, in order to make the following order-of-magnitude estimate.

[76] S.L. Ren, *et al*, Appl. Phys. Lett. **59**,2678 (1991).

[77] G.F. Bertsch, A. Bulgac, D. Tomanek, and Y. Wang, Phys. Rev. Lett. **67**, 2690 (1991).

[78] O. Gunnarson, D. Rainer, and G. Zwicknagl, Int. J. Modern Phys. B **6**, 3993 (1992).

[79] E. Westin and A. Rosen, Int. J. Modern Phys. B **6**, 3893 (1992).

[80] B. Shanker and J. Applequist, J. Phys. Chem. **98**, 6486 (1994).

[81] M.F. Lin and K. W.-K. Shung, Phys. Rev. B **47**, 6617 (1993); P. Longe and S.M. Bose, Phys. Rev. B **48**, 18239 (1993).

[82] B. Koopmans, PhD Thesis, University of Groningen, 1993.

[83] H. Ehrenreich and M.H. Cohen, Phys. Rev. **115**, 786 (1959).

[84] M.S. Hybertson and S.G. Louie, Phys. Rev. B **35**,

5585 (1987); Phys. Rev. B **35**, 5602 (1987).

[85] L.D. Landau and E.M. Lifshitz, *Electrodynamics of Continuous Media* (Pergamon Press, Oxford, 1960).

[86] In order to check the internal consistency of the calculation, we calculated α_{0xx} of some of the smaller tubes with $\hat{\mathbf{x}}$ in different directions. The answer was always independent of the chosen direction.

[87] J.M. Ziman, *Principles of the Theory of Solids* (Cambridge University Press, Cambridge, 1972).

[88] D.C. Harris and M.D. Bertolucci, *Symmetry and Spectroscopy* (Dover, New York, 1989).

[89] R.A. Jishi, M.S. Dresselhaus, and G. Dresselhaus, Phys. Rev. B **47**, 16671 (1993).

[90] R.A. Jishi, M.S. Dresselhaus, and G. Dresselhaus, Phys. Rev. B **48**, 11385 (1993).

[91] J.M. Ziman, *Electrons and Phonons* (Cambridge University Press, Cambridge, 1960).

[92] There are actually two places in the Brillouin zone where bands cross the Fermi level, giving rise to two disconnected regions of Fermi surface. We consider only one in this discussion. The inclusion of "intervalley" scattering processes is straightforward, and does not affect our conclusions.

[93] We have implicitly assumed that the scattering mechanism is elastic.

[94] L. Pietronero, R. Strassler, H.R. Zeller, and M.J. Rice, Phys. Rev. B **22**, 904 (1980).

[95] M.S. Dresselhaus, G. Dresselhaus, and J.E. Fischer, Phys. Rev. B **15**, 3180 (1977).

[96] J.E. Fischer, and T.E. Thompson, Phys. Today, July, 36 (1978), and references therein.

[97] The sensitivity of density of states to radius and/or Fermi level arises because the graphite sheet Fermi surface is much smaller than its Brillouin zone. See the discussion in chapter 1.

[98] J. Tersoff and R.S. Ruoff, Phys. Rev. Lett., **73**, 676 (1994).

[99] W. Primak, and L.H. Fuchs, Phys. Rev., **103**, 541 (1956).

[100] V. Bayot et al., Phys. Rev. B **41**, 11770 (1990). These authors measure the conductivity of turbostratic graphite to be below that of ABAB-stacking graphite. They argue that disorder-induced weak localization is partly responsible for the decreased conductivity.

[101] S. N. Song, X. K. Wang, R. P. H. Chang, and J. B. Ketterson, Phys. Rev. Lett. **72**, 697 (1994); L. Langer, L. Stockman, J. P. Heremans, V. Bayot, C. H.

Olk, C. Van Haesendonck, Y. Bruynseraede, and J.-P. Issi, J. Mater. Res. **9**, 927 (1994).

[102] L. Langer, V. Bayot, E. Grivei, J.-P. Issi, J. P. Heremans, C. H. Olk, L. Stockman, C. Van Haesendonck, and Y. Bruynseraede, Phys. Rev. Lett. **76**, 479 (1996).

[103] W. Tian and S. Datta, Phys. Rev. B **49**, 5907 (1993); M.F. Lin and K.W.-K. Shung, Phys. Rev B **51**, 7592 (1995).

[104] R. Landauer, Phil. Mag. **21**, 863 (1970).

[105] D. S. Fisher and P. A. Lee, Phys. Rev. B **23** 6851 (1981).

[106] L. Chico, V. H. Crespi, L. X. Benedict, S. G. Louie, and M. L. Cohen, Phys. Rev. Lett. **76**, 971 (1996).

[107] M. P. López Sancho, J. M. López Sancho, and J. Rubio, J. Phys. F: Metal Phys. **14**, 1205 (1984); M. P. López Sancho, J. M. López Sancho, and J. Rubio, J. Phys. F: Metal Phys. **15**, 851 (1985).

[108] T. N. Todorov and G. A. D. Briggs, J. Phys.: Cond. Matt. **6**, 2559 (1994).

[109] For each LDOS presented, we add the LDOS of all atomic sites in the cell, and divide by the number of atoms.

[110] We use the term "discrete angular momentum" somewhat loosely here. The more precise statement is that electronic states of n-fold rotationally symmetric tubes act as basis functions for irreducible representations of the point group C_n.

[111] An approximate classical analogue of this phenomenon can be found on pp. 85-86 of V. I. Arnold, *Mathematical Methods of Classical Mechanics*, Springer-Verlag, New York, 1989.

[112] See for example the $(8,0)/(7,1)$ junction studied in chapter 6. In this case, however, the $(8,0)$ tube is a semiconductor, so the presence of a conductance gap is expected on more basic grounds.

[113] P.E. Ross, Scient. Am. **265** (December), 24 (1991).

[114] R.S. Ruoff et al (add authors)., Nature, **364**, 514 (1993).

[115] We refrain from calling this term the Van der Waals energy because other correlation-born contributions and kinetic contributions to the interlayer binding energy may also be important.

[116] N. G. Chopra, L. X. Benedict, V. H. Crespi, M. L. Cohen, S. G. Louie, and A. Zettl, Nature **377**, 135 (1995).

[117] S.A. Safran, *Statistical Thermodynamics of Surfaces and Interfaces* (Addison Wesley, Reading, MA, 1994).

[118] X. Blase, A. Rubio, S.G. Louie, and M.L. Cohen, Europhys Lett. **28**, 335 (1994).

[119] Unless the curved regions consist entirely of two semicircles.

[120] J.-C. Charlier, X. Gonze, and J.-P. Michenaud, Europhys. Lett. **28**, 403 (1994).

[121] M. Côté, private communication.

[122] J.-C. Charlier and J.-P. Michenaud, Phys. Rev. Lett. **70**, 1858 (1993).

[123] L. A. Girifalco and R. A Lad, Jour. Chem. Phys. **25**, 693 (1956) and references therein.

[124] H. J. Bernstein, Trans. Faraday Soc. **58**, 2285 (1962).

[125] A. D. Crowell, J. Chem. Phys. **22**, 1397 (1954).

[126] N. L. Allinger, J. Am. Chem. Soc. **99**, 8127 (1977).

[127] J. T. Sprague and N. L. Allinger, Jour. of Computational. Chem. **1**, 257 (1980).

[128] A. A. Ahmadieh and H. A. Rafizadeh, Phys. Rev. B **7**, 4527 (1973).

[129] E. Santos and A. Villagrá, Phys. Rev. B **6**, 3134 (1972).

[130] R. O. Brennan, J. Chem. Phys. **20**, 40 (1952).

[131] R. Setton, Carbon **33**, 1135 (1995).

[132] In reference [116], we estimated R_{crit} for a few different N, and obtained values that are larger than those reported here. We have since refined the model, and take the present predictions to be the most accurate.

[133] L.X. Benedict, V.H. Crespi, N.G. Chopra, S.G. Louie, M.L. Cohen, A. Zettl, and V. Radmilovic, to be published.

[134] A similar rotation known as the Stone-Wales transformation is used in the study of C_{60} fullerene isomers. A. J. Stone and D. J. Wales, Chem. Phys. Lett. **128**, 501 (1986).

[135] A. Toyota, M. Kataoka, and S. Koseki, Chem. Lett. (volume numbers not used) May 1992, p. 791.

[136] The final relaxed structure after the single bond rotation is 0.17 eV in energy below that of planar pentaheptite. A single sheet of planar carbon pentaheptite is metastable against bond rotation and local formation of a hexagonal network.

[137] We use the graphite sp^3 Slater-Koster tight-binding parameters of Tomanek and Louie. The distance dependence is taken to be a linear interpolation between graphite first and second neighbor parameters. D. Tomanek and S. G. Louie, Phys. Rev. B **37**, 8327 (1988).

[138] L. X. Benedict, V. H. Crespi, S. G. Louie, and M.

L. Cohen, Phys. Rev. B **52**,
14935 (1995).

Ernest Orlando Lawrence Berkeley National Laboratory
One Cyclotron Road | Berkeley, California 94720

Prepared for the U.S. Department of Energy under Contract No. DE-AC03-76SF00098